State-dependent RF-Dressed Ring traps for Sagnac Interferometry

Submitted January 2024, in partial fulfillment of
the conditions for the award of the degree **PhD Physics.**

Vilius Atkocius
14255892

Supervised by Thomas Fernholz

School of Physics and Astronomy
University of Nottingham

Date: 01 / 01 / 2024

Abstract

This thesis describes the experimental realisation of state-dependent traps employing RF-dressed adiabatic potentials. ^{87}Rb atoms have been successfully confined to chip-based atom traps that can independently address atomic ground states defined by the total angular momentum, F. The ring-shaped trap can be used as a Sagnac interferometer to measure rotation with respect to the inertial frame of reference. The results of spatially dependent radio frequency field polarisation control in this trap resulted in counterpropagating motion of the atoms in the $F = 1$ and $F = 2$ states.

Acknowledgements

I would like to thank the entire cold atoms group at the University of Nottingham for continued support, kindness, productive discussions and unproductive conversations. First, I would like to thank my supervisor Thomas Fernholz for his help and guidance during my PhD. Your LabView skills are unmatched. I would also like to thank J. Johnson, R. Morrison, C. Mishra, F. Gentille, K. Poulios for working with me on this project. Some of you I only saw briefly and I spent several years with the others and it has been a pleasure to work with all of you. Thank you T. Pyragius for introducing me to the world of experimental physics.

I would also like to extend my appreciation to university's technical support team which always exceeded my expectations for the quality of the end product, D. Sims for keeping us on track for success, and C. Mellor, my second supervisor, who shared his vast knowledge about chip fabrication.

During these years I have met many kind and interesting people who kept me company. Whether it's a quick chat in the hallway or heated discussions during lunch breaks, I appreciate it all.

"Ad virtutis ad meliores exitus" is a loose translation to Latin of a phrase used many times in the lab, meaning *"more power, more beter"*. Numerous times this proved to be correct; whether it was lasers, more current in coils, higher RF power or something else. Contributing to these lunchtime discussions and talks were wonderful people pushing me to do more, to do better and not settle for a quick fix when things went wrong. I would like to thank: B. Foxon, H. Abbat, J. New, R. Giji, F. Owen, L. Knöbelreiter, L. Rushton, L. Elson, D. Johnson, E. da Ros, B. Hopton, M. Overton, N. Cooper, S. Madkhali, V. Naniyil, C. Colquhoun, L. Hackermüller, A. Davis, K. Jensen, A. Meraki, A. Akbar and others.

My gratitude goes toward my examiners, Dr. Elliot Bentine and Prof. Juan P. Garrahan for taking their time to provide constructive feedback.

Finally, I would like to thank my family: my mother, Lina, and brothers, Justinas and Karolis.

Contents

List of Tables

List of Figures

Chapter 1

Introduction

This thesis describes work on building an atom interferometer capable of measuring rotation through the use of state-dependent radio frequency (RF)-dressed adiabatic potentials. Successful progress toward the Sagnac interferometer has been made by demostrating a state-dependent transport of ^{87}Rb atoms in a ring-shaped trap. I will present to you a journey from putting the atom chip inside the vacuum chamber to state-dependently guiding the atoms on a chip.

1.1 Description of Work

The structure of this PhD thesis is outlined below, including a short description of the contents and key ideas/results.

Chapter 1: A brief overview of the history of rotation detection and the motivation behind the experiment is presented. Historical links between first devices to sensors underpinning modern technology are covered. Following the chronicle of discoveries leading to matterwave interferometry is the motivation for our particular implementation of the Sagnac interferometer. State-of-the-art experiments within the field are reviewed and potential advantages of our setup over the competing strategies is explained. Lastly, we touch on the milestones that are key to the success of the experiment with a brief look at the importance of each one to the success of the overall project.

Chapter 2: The theory behind the state-dependent transport scheme is investigated and key results are presented. Numerical simulations as well as analytical results will provide insight into the interaction between atomic spins, static magnetic fields, and RF radiation. A general model of an atom interacting with magnetic fields will be presented before we show how the potentials can be dynamically shaped to drive atoms around an enclosed loop to perform Sagnac interferometry.

Chapter 3: The experimental setup will be described in this chapter. This includes the vacuum setup, RF & microwave (MW) electronics, control & timing infrastructure, laser optics, current carrying wire configuration and AC field source description. Some of the in-house-built component designs developed for this project are also included here.

Chapter 4: This chapter will present experimental techniques and results leading towards a rotation sensing device. The covered subjects range from initial laser cooling of the atoms to preparing quantum superpositions of states that can be guided independently of each other. A full loop around the ring in one of the quantum states has been completed to show the multi-loop capability for a measurement with increased sensitivity.

Chapter 5: The summary of this thesis will look at the overall progress towards the fully functional rotation sensor and review the remaining hurdles to overcome. A method to reduce transition linewidth dependence on the applied magnetic field will be presented as well as design improvements are presented. Additionally, a time-averaging scheme will be presented to make the device more robust against mechanical motion.

1.2 Overview

A Sagnac interferometer, first introduced by Georges Sagnac [3], is a device used to measure one's rotation with respect to inertial frame of reference at a rate, Ω_{rot}, using the phase shift that arises in an area-enclosing interferometer.

The early concepts of measuring rotation rate date back as far as the 2nd century BC with the Chinese invention of a mechanical device known as the "South Pointing Chariot" [4], which employed a rotating wheel to maintain its direction of travel. In 1851 the Earth's rotation rate was measured with the help of a large pendulum by the French physicist Jean Bernard Leon Foucault [5]. The pendulum's precession displayed a gyroscopic effect, setting the foundation for further gyroscope development. The first practical gyroscopes used mechanical motion to provide stabilising force, keeping the device still with respect to the inertial frame of reference. Initially used for naval navigation applications, these devices were developed in the early nineteenth century, notably the gyrocompass built by the German inventor Hermann Anschütz-Kaempfe in 1908 and the Sperry Gyroscope, invented by Elmer Ambrose Sperry in 1933. As time passed, gyroscopes became essential pieces of equipment in aerospace and space applications. In the late 20th century, compact devices based on micro-electromechanical systems (MEMS) technology [6] made rotation sensors widely available with sensitivity high enough to measure the Earth's rotation rate with a cheap sensor in a smartphone [7]. Ring laser gyroscopes (RLGs) and fibre optic gyroscopes (FOGs) that use interferometry of light travelling in a ring cavity (RLGs) and a coiled optical fibre (FOGs) offer a higher level of measurement precision than MEMS devices and are frequently the preferred option in the inertial sensing field. The first ring laser gyroscope was built in 1963 [8] and since then further research has shown the feasibility of interfering with matter waves rather than electromagnetic waves, which brings its own set of benefits and challenges [9]. Namely, an increase in rotation sensitivity of an order of 10^{10} has been estimated to be achieved by replacing conventional electromagnetic waves with matter waves [10]. The reason for this dramatic gain in sensitivity comes from the much larger accumulated phase of a matter interferometer compared to its light counterpart for the same rotation $\phi_{matter}/\phi_{light} = mc^2/\hbar\omega$, where

$m \approx 10^{-25} kg$ is the mass of the Rb-87 atom, c is the speed of light, $\hbar$ the reduced Planck constant, and $\omega \approx 2\pi \times 10^{15} Hz$ is the angular frequency of light.

The Sagnac interferometer works by splitting coherent wavepackets into a superposition of waves travelling on a closed-loop path in counter-propagating manner. When the waves recombine again after completing a full loop, a measurement is made to determine the differential phase imprinted onto the wavepackets due to the setup rotating with respect to an inertial frame of reference, also called the Sagnac phase ϕ_{Sagnac}.

Although we use Sagnac's invention to measure the rotation rate with high precision to this day, he made the wrong assumption about what gives rise to this phase shift between different paths that the waves take. The interferometer was first built to prove the existence of luminiferous aether. The argument proposed was that an observer travelling through the aether would experience a frictional drag force. The higher the relative velocity of the observer to the aether would lead to the greater the drag force. Under rotation with respect to stationary frame of reference this would mean that wavepackets are moving with the flow of aether while the waves in the other arm of the interferometer would propagate against the flow as shown in figure 1.1, hence the differential phase would manifest from discrepancy in the drag force.

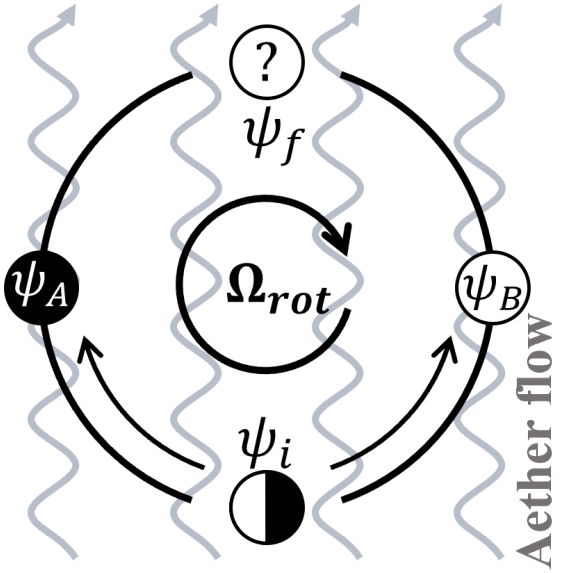

Figure 1.1: According to Sagnac, waves propagating in opposite arms of the interferometer should experience different amounts of drag force resulting in a phase shift ϕ_{Sagnac} when the experiment is rotating with respect to an inertial frame of reference at a rate Ω_{Rot}.

Further work by Max von Laue [11] and Paul Langevin [12, 13] has shown that one can derive the differential phase from relativistic effects, making the experimental rotation rate measurement possible even in the absence of luminiferous aether. In fact, the effect can be expressed in terms of the proper time difference for particles travelling in opposite directions. One of the more impressive examples of related measurement was carried out by Joseph C. Hafele and Richard E. Keating [14], where they placed two identical atomic clocks on aeroplanes travelling around the Earth in opposite directions and managed to predict and measure the relative time difference between the two devices caused by relativistic effects.

This PhD project expands on the idea of a matter-wave Sagnac interferometer by introducing a novel way of guiding the interfering particles around an enclosed path rather than using ballistic transport. The scheme for this experiment was introduced in 2007 [15], and only realised in practise 16 years later. Details of previous theoretical and experimental work can be found in theses by T. Bishop [16], F. Gentile [17], and J. Johnson [18].

1.3 Motivation

Sagnac interferometers have a wide variety of uses, including current sensing [19], temperature measurement [20], gravitational wave detection [21, 22], and rotation sensing [23, 24]. Today, Sagnac interferometers are considered to be some of the most accurate devices for precise rotation measurements. The technology has improved significantly with the rise of fibre optic gyroscopes guiding aircraft and space missions [25], however, matter wave interferometers are getting closer to becoming a better alternative due to their long-term stability. Even the best FOGs are limited by the bias instability, meaning that eventually the accuracy of the measurement cannot improve any further by averaging the measurement over longer times. The averaging time limit of the FOGs is around $10000s$ [26], after which systematic effects, such as the Earth's tidal forces and temperature swings start increasing the uncertainty in the measurement. A recent paper by a research group in Paris [27] observed no such levelling off in precision on the same time

scale with their cold-atom system. Given that a sufficiently small size, weight and power package is achieved, a matter-wave interferometer can be used to supplement conventional ring laser gyroscopes to limit systematic drift in inertial navigation framework [28].

The early matter wave interferometer designs rely on atoms freely falling in space [29, 30, 31], therefore, increasing the sensitivity by increasing the enclosed area of the device becomes challenging. Making an interferometer with a larger area with this design requires increasingly taller vacuum setups to accommodate the atoms accelerating downward with gravity. Later generations of interferometers take advantage of multi-loop schemes [32] and some setups also rely on moving the atoms along the guide, thus reducing the volume of the device. The majority of these schemes, however, still rely on ballistic transport of atoms along the guide [23, 33, 34].

The free propagation of atoms in a guide means that one needs to impart some momentum to atoms travelling around the loop in order to complete a full loop. This is not an issue when the atoms are moving horizontally; nevertheless, the single-loop area becomes limited under tilt due to gravitational potential gradient. Large momentum kicks may cause parametric heating and may still be insufficient to reach the top of the guide. Another prevalent issue stems from the spread of atomic wavepackets along the waveguide over time, leading to a reduced measurement contrast. Instead, we opt for a fully trapped setup that uses RF-dressed adiabatic potentials [35] that trap atoms in all three dimensions during measurement [15, 36].

With the advent of atom chip technology [37], cold-atom experiments can be made compact and more power efficient. Atoms chips use microfabrication techniques to deposit small wire structures on substrates, usually made of silicon. Evaporated metal conductors have few imperfections and can be placed a few μm from the atoms which leads to high trapping field gradients. Small size and low power requirements play in our favour; therefore, an atom chip setup has been chosen as the initial platform to test the feasibility of such device. Due to atoms being in close proximity to the conductors, one can achieve extremely high field gradients for atom trapping, and the RF field magnitude required for guiding the atomic ensemble can be achieved with off-the-shelf commercially available

components.

1.4 Aims and Objectives

The key requirements for achieving a functional rotation sensing device are listed below. The motivation behind our design choices and the significance of each of the milestones will be presented.

Loading Atoms Into a Ring Trap

The experimental setup consists of many current-carrying components, as well as RF and MW sources, which work together to produce a dense atomic ensemble prepared in a quantum state needed to measure the Sagnac phase. External coils and ultra-high vacuum compatible part of the setup work hand in hand during the transport stage from a typical six beam magneto-optical trap to a trap produced by the atom chip. Along the way, the atoms are pumped into a magnetically sensitive state, transferred into a purely magnetic DC trap, cooled down and loaded into a complex potential.

RF Field Control

Multiple sources of RF fields are used to produce state-dependent potentials that can be individually moved around by achieving a high level of control over the RF field frequency and spatially dependent polarisation. We will outline the field-producing elements in the setup, their role, and verification procedures in place used to ensure the correct operation of the device.

State-Dependent Transport

Through the use of constructive and destructive interference of the fields, the RF dressed adiabatic potentials are shaped to serve as a matterwave guide that is capable of state-dependent atom transport. The experimental realisation of such a transport method has not been shown before and is therefore interesting from the perspective of practical applications as well as fundamental science. We demonstrate the capability of completing a full loop around the atom chip guide with atoms moving in counter-propagating directions.

The Ramsey Sequence

A series of carefully timed MW pulses is required for the operation of our device. We use a spin-echo-type sequence to eliminate any phase that rises from the guide having small asymmetric manufacturing imperfections or from the tilted operation of the device with respect to gravity. The description of the sequence and key parameters will be provided in the chapters 2 and 4 of this thesis.

Gyroscope Realisation

Although we already have a grasp on how to perform state-dependent transport and MW pulse sequences to obtain an interferometric phase, the combination of the two to obtain a rotationally sensitive measurement has yet to be achieved. The nature of the biggest hurdles to overcome will be identified with a path to address the most recent challenges.

Design Improvements

Most of the tasks to be completed during this project have been successfully realised; however, there are many ways to improve the setup in the future. On the basis of the experimental observations, many areas for design improvement were identified. The main challenges will be covered, as well as the description of specific setup alterations to address them. Unfortunately, due to time constraints, these changes in the experiment are yet to be implemented; however, significant progress has been made towards the inclusion of additional infrastructure.

These upgrades may include but are not limited to:

- MW dressing scheme that shows promising results towards achieving a narrow spectral width of a clock transition required for high precision measurements,
- adding more strategically placed wire structures,
- implementation of time-averaged potentials to improve the spatial overlap of the state-dependent traps.

Chapter 2

The Atomic Sagnac interferometer

This chapter examines the development of RF-dressed adiabatic potentials for atom trapping and transport. We will begin by exploring the general operating principles of a Sagnac interferometer. We will then analyse the energy-level structure of a single Rb-87 atom and the microwave pulses used to couple the energy levels of interest. We will then discuss the potentials created by time-dependent magnetic field interactions. Finally, we will investigate a particular type of RF-dressed trap, as the ring lattice geometry is beneficial for the construction of the rotation sensor.

2.1 The Sagnac Phase

The operation of the Sagnac interferometer shown in figure 2.1 can be explained through relativistic effects that lead to rotation measurements. We can start from simple Lorentzian transformations to explain what gives rise to the Sagnac phase. For this example, we assume that the waves travel around the circular loop with radius R, in counter-propagating directions, at velocity v.

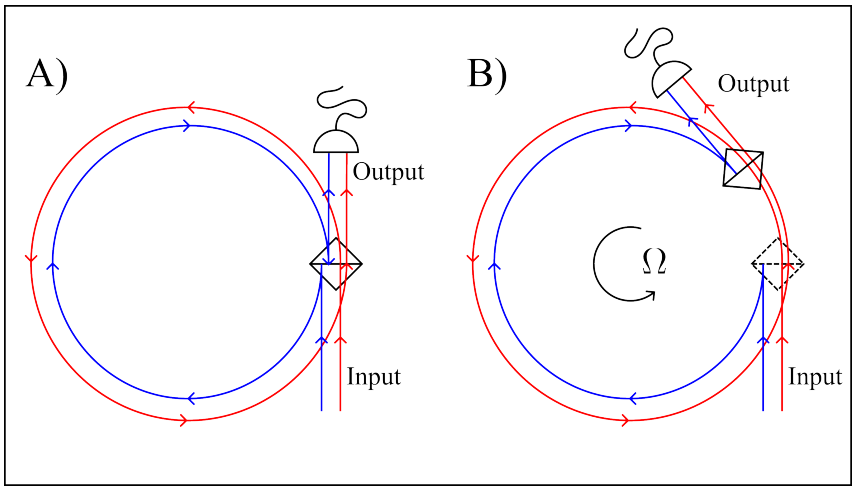

Figure 2.1: Relativistic Sagnac interferometer.

We denote the waves travelling in counter-clockwise direction with the subscript '+' and the waves travelling in the opposite direction with '−'. We assume that the entire setup is rotating with respect to an inertial frame of reference with rate Ω. The time in this rotating frame of reference, t', is transformed according to equation 2.1

$$t' = \gamma \left(t - \frac{\Omega R x}{c^2} \right), \tag{2.1}$$

where c is the speed of light, γ is the Lorentz factor, t is the time and x is the position in the inertial frame of reference.

The position in this dynamic frame of reference is given by x'.

$$x' = \gamma \left(x - \Omega R t \right), \tag{2.2}$$

where γ is defined as

$$\gamma = \frac{1}{\sqrt{1 - \frac{v^2}{c^2}}}. \tag{2.3}$$

Here, $v = x/t$ is the phase velocity. In the transformed frame of reference, we can look at the velocity $v'_{\pm}$, and path length $l'_{\pm}$, for the two waves.

$$v_{\pm} = \frac{v \pm R\Omega}{1 \pm \frac{vR\Omega}{c^2}} \tag{2.4}$$

$$l'_{\pm} = 2\pi R \pm R\Omega t'_{\pm} \tag{2.5}$$

From equations 2.4 and 2.5 we can calculate the arrival times of waves in each of the interferometer arms.

$$t'_{\pm} = \frac{l'_{\pm}}{v'_{\pm}} = \frac{2\pi R \left(1 \pm v\Omega/c^2\right)}{v \left(1 - \frac{R^2\Omega^2}{c^2}\right)}, \tag{2.6}$$

which in turn gives us the time difference Δt.

$$\Delta t = \left| t'_{-} - t'_{+} \right| = \frac{4\pi R^2 \Omega}{c^2 \left(1 - \frac{R^2\Omega^2}{c^2}\right)} \tag{2.7}$$

With atom interferometers we can use Δt scaled by the Compton frequency [38] to find the Sagnac phase, ϕ_{Sagnac}, imprinted due to rotation with respect to the inertial frame of reference.

$$\phi_{Sagnac} = 2\pi f_{Compton} \Delta t = 2\pi \frac{mc^2}{h} \Delta t \tag{2.8}$$

In the regime where $R^2\Omega^2 << c^2$ equation 2.8 simplifies to

$$\phi_{Sagnac} = \frac{4mA\Omega}{\hbar}, \tag{2.9}$$

where m is the mass of the particles, and $A = \pi R^2$ is the effective area enclosed by the interferometer path. For classical waves, one should use the frequency of the waves rather than the Compton frequency. One can notice that, in the end, the Sagnac phase depends on the rotation rate, Ω, and not the velocity of the particle.

We can also examine the errors associated with the measurement. The mass term's uncertainty is much lower than the other terms, so it can be disregarded. The Planck constant is fixed, so the only sources of uncertainty in the measurement are δA and $\delta\Omega$.

$$\begin{aligned} \delta\phi^2_{Sagnac} &= \left(\frac{\partial\phi_{Sagnac}}{\partial A}\delta A\right)^2 + \left(\frac{\partial\phi_{Sagnac}}{\partial\Omega}\delta\Omega\right)^2 \\ &= \left(\frac{m\Omega}{h}\delta A\right)^2 + \left(\frac{mA}{h}\delta\Omega\right)^2 \end{aligned} \tag{2.10}$$

The first term in equation 2.10 tends to 0 if $\Omega = 0$. We can achieve this through compensation of the rotation by placing our setup on a rotating platform that cancels the motion with respect to the inertial frame of reference. When motion around the axis of rotation is compensated completely, the device measures no phase shift, and the rotation rate is inferred from the corrections that had to be applied to the system. This technique is called gimballing and allows us to minimise the errors associated with δA. Another solution would involve moving the atoms in the two interferometer arms at different rates to make sure that they meet at the same location within the inertial frame. This will be discussed in further sections of this chapter. The second term corresponds to systematic errors that cannot be avoided.

2.2 The ^{87}Rb Atom

It is important to understand the underlying structure of the atom in question before we continue to look at a specific case. A comprehensive description and many useful data on the atomic structure of ^{87}Rb are compiled in the paper by D. Steck [2]. Another useful reference may be the textbook by C.J. Foot [39]. We begin by looking at the energy-level structure defined by the interactions between the single outermost electron and the nucleus of the atom.

The energy structure of group IA elements is very similar to Bohr's model of an atom [40] which only considers a single electron orbiting the positively charged nucleus. Bohr's model of an atom describes the energy-level structure that only depends on the fundamental quantum number n.

$$E_n = -\frac{Z^2 R_E}{n^2}, \tag{2.11}$$

where Z is the atomic mass of the atom in question and R_E is the Rydberg energy. This, however, does not represent the energy-level structure of heavier atoms, and quantum defect correction has to be introduced to match the experimentally observed spectral data. The binding energy required to kick the electron out of its orbit then follows the modified relation.

$$E_B = -\frac{Z^2 hc}{(n-\delta_s)^2}, \tag{2.12}$$

where h is the Planck's constant, and $\delta_s = 3.19$ is the quantum defect associated with the electronic spin that interacts with the nucleus of the atom. Quantum defect values for various alkali metal atoms can be found in [39]. The outer electron of ^{87}Rb is in the energy state given by the fundamental quantum number $n = 5$.

Electrons have a magnetic moment $\boldsymbol{\mu_S}$ proportional to the spin angular momentum vector, $\boldsymbol{S}$. When these electrons orbit a positively charged nucleus, they see an effective magnetic field $\boldsymbol{B}$ which depends on the total angular momentum $\boldsymbol{L} = \boldsymbol{r} \times \boldsymbol{p}$. Here, $\boldsymbol{r}$ is the position of the electron with respect to the nucleus and $\boldsymbol{p}$ is the momentum of the electron. The

energy shift due to this spin angular momentum and orbital angular momentum follows the relation in equation 2.13.

$$\Delta E = -\boldsymbol{\mu_S} \cdot \boldsymbol{B}, \tag{2.13}$$

which is directly proportional to quantity $\boldsymbol{L} \cdot \boldsymbol{S}$. To find the expression for $\boldsymbol{L} \cdot \boldsymbol{S}$, we introduce a quantity $\boldsymbol{J}$, known as the total angular momentum of the electron.

$$\boldsymbol{J} = \boldsymbol{L} + \boldsymbol{S}. \tag{2.14}$$

Taking the dot product of $\boldsymbol{J}$ with itself we find that

$$2\boldsymbol{L} \cdot \boldsymbol{S} = \boldsymbol{J}^2 - \boldsymbol{L}^2 - \boldsymbol{S}^2. \tag{2.15}$$

J can take values in the range $|L - S| \leq J \leq |L + S|$ that determine the ground state of ^{87}Rb with $L = 0$, $S = 1/2$ and $J = 1/2$ as well as the first excited state with $L = 1$, $S = 1/2$, and $J = 1/2$ or $J = 3/2$. This fine structure of the atom determines the optical transition lines, known as the D_1 line for the $5^2S_{1/2} \leftrightarrow 5^2P_{1/2}$ transition and the D_2 line for the $5^2S_{1/2} \leftrightarrow 5^2P_{3/2}$ transition. The D_1 transition for ^{87}Rb corresponds to a wavelength of about 795nm, while the D_2 line can be seen at 780nm.

The further splitting of the ground and excited states describes the hyperfine structure of the atom as a result of the coupling between the total electron angular momentum $\boldsymbol{J}$ and the total nuclear angular momentum $\boldsymbol{I}$. The total angular momentum of the atom is presented as a quantity $\boldsymbol{F}$.

$$\boldsymbol{F} = \boldsymbol{J} + \boldsymbol{I} \tag{2.16}$$

F can take values in integer steps that fall within the range $|I - J| \leq F \leq |I + J|$. ^{87}Rb has nuclear angular momentum $I = 3/2$ and therefore, for a ground state $J = 1/2$, F can take values of 1 or 2. By the same example, the excited state $5^2P_{1/2}$ can have values $F = 1, 2$ and the state $5^2P_{3/2}$, corresponding to the line D_2, has possible values

$F = 0, 1, 2, 3$. The Hamiltonian in this case is represented by

$$\hat{H}_{hfs} = A_{hfs}\boldsymbol{I}\cdot\boldsymbol{J} + B_{hfs}\frac{3\left(\boldsymbol{I}\cdot\boldsymbol{J}\right)^2 + \frac{3}{2}\boldsymbol{I}\cdot\boldsymbol{J} - I\left(I+1\right)J\left(J+1\right)}{2I\left(2I-1\right)J\left(2J-1\right)}, \tag{2.17}$$

which leads to eigenenergies that correspond to hyperfine structure energy shift.

$$\Delta E_{hfs} = \frac{1}{2}A_{hfs}K + B_{hfs}\frac{\frac{3}{2}K\left(K+1\right) - 2I\left(I+1\right)J\left(J+1\right)}{2I\left(2I-1\right)2J\left(2J-1\right)}, \tag{2.18}$$

where A_{hfs} is the magnetic dipole constant, B_{hfs} is the electric quadrupole constant that has a value of 0 for the states $J = 1/2$, and K is given by

$$K = F\left(F+1\right) - I\left(I+1\right) - J\left(J+1\right). \tag{2.19}$$

The values for A_{hfs} and B_{hfs} can also be found in [2]. Equation 2.18 defines the energy level shifts due to hyperfine structure that can be interrogated by a laser. For the purposes of this experiment, the D_2 line is of greater interest because of the existing cycling optical transition that can be used to capture and cool atoms. The energy level diagram of the transition D_2 is provided below.

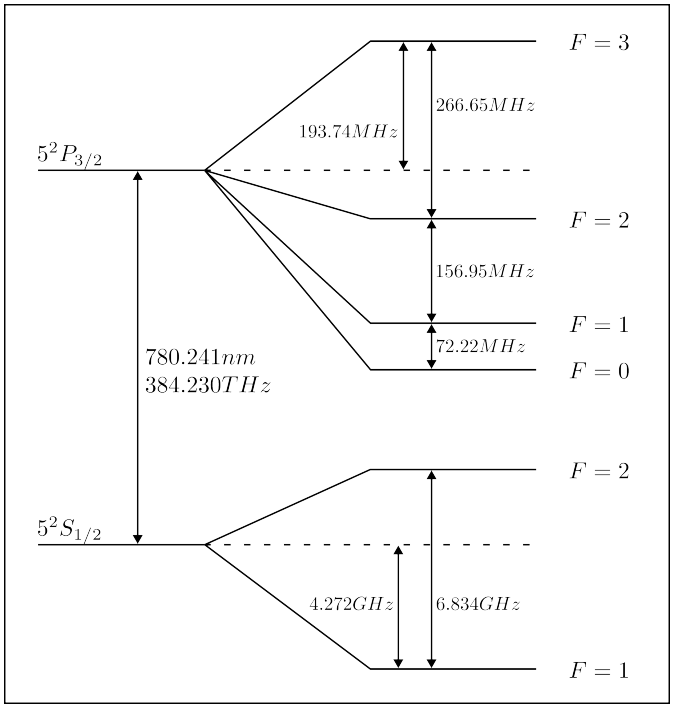

Figure 2.2: D_2 line ^{87}Rb structure. Data taken from [2].

Now we can look at the structure that forms due to interactions between applied static magnetic fields and the atomic spin. The Hamiltonian for this interaction is

$$\hat{H}_{DC} = -\boldsymbol{\mu_{tot}} \cdot \boldsymbol{B} = \frac{\mu_B}{\hbar} \left(g_S \boldsymbol{S} + g_L \boldsymbol{L} + g_I \boldsymbol{I} \right) \cdot \boldsymbol{B}, \tag{2.20}$$

where μ_B is the Bohr magneton, $\hbar$ is the reduced Planck's constant, $\boldsymbol{B}$ is the applied external magnetic field, and g are the g-factor constants that take into account changes in the electron spin, electron orbital, and nuclear parts of the magnetic moment. If the applied magnetic field provides energy shifts smaller than the fine structure, then the Hamiltonian can be described by quantum numbers $\boldsymbol{J}$ and $\boldsymbol{I}$. Without any loss of generality, we can choose the magnetic field to be pointing along the z-axis. This leaves us with the Hamiltonian expression that can be written as

$$\hat{H}_{DC} = \frac{\mu_B}{\hbar} \left(g_J \hat{J}_z + g_I \hat{I}_z \right) B_z. \tag{2.21}$$

The Hamiltonian can be simplified even further if the applied magnetic field introduces energy shifts that are smaller than hyperfine splittings [41]. The equation in that case can be described by a single quantum number $\boldsymbol{F}$

$$\hat{H}_{DC} = \mu_B g_F \hat{F}_z B_z, \tag{2.22}$$

where F_z and B_z are projections of $\boldsymbol{F}$ and $\boldsymbol{B}$ on the z-axis, and g_F is called the hyperfine Landé g-factor. g_F can be expressed as

$$\begin{aligned} g_F &= g_J \frac{F\left(F+1\right) - I\left(I+1\right) + J\left(J+1\right)}{2F\left(F+1\right)} + g_I \frac{F\left(F+1\right) + I\left(I+1\right) - J\left(J+1\right)}{2F\left(F+1\right)} \\ &\approx g_J \frac{F\left(F+1\right) - I\left(I+1\right) + J\left(J+1\right)}{2F\left(F+1\right)}, \end{aligned} \tag{2.23}$$

with g_J expressed as

$$\begin{aligned} g_J &= g_L \frac{J(J+1) - S(S+1) + L(L+1)}{2J(J+1)} + g_S \frac{J(J+1) + S(S+1) - L(L+1)}{2J(J+1)} \\ &\approx 1 + \frac{J(J+1) + S(S+1) - L(L+1)}{2J(J+1)}. \end{aligned} \tag{2.24}$$

The simplified result for g_j comes from assuming approximate values $g_s \approx 2$ and $g_L \approx 1$ [2]. the Hamiltonian from equation 2.22 is described by the linear Zeeman effect which leads to energy level splitting, determined by the quantum number m_F, corresponding to the projection of the total atomic angular momentum onto the quantisation axis set by the applied magnetic field [42].

$$\Delta E_{|F,m_F\rangle} = \mu_B g_F m_F B_z \tag{2.25}$$

The m_F can take values $|-F| \leq m_F \leq |F|$ and for the ground states of ^{87}Rb the two ground states have similar magnitudes but opposite signs $g_{F=1} \approx -g_{F=2} \approx -1/2$ [43]. The states of interest for us are the low-field seeking states that have the potential minimum at zero magnetic field. Wing [44] stated that by generalising Earnshaw's theorem one can deduce that there may only exist magnetic field local minima but no maxima can occur. This means that we can only use low-field seeking states when trapping atoms in DC traps. This may not be the case for dynamic potentials.

The states of interest for this device are $|F = 2, m_F = 1\rangle$ and $|F = 1, m_F = -1\rangle$ due to having a very similar energy shift $\Delta E_{|F=2,m_F=1\rangle} \approx \Delta E_{|F=1,m_F=-1\rangle}$. This ensures that even in spatially varying magnetic field, the transition frequency between the two states is constant.

2.3 The Ramsey Sequence

To measure the Sagnac phase, an optical gyroscope needs interfering photons, mirrors and beam splitters. The matterwave counterpart can use microwave frequency pulses as optical components to power a Ramsey interferometer [45]. Multiple pulses can be used to operate a Ramsey - Bordé interferometer [46], which reduces common-mode noise during the measurement.

The theoretical description of the interaction between the spins of the atoms and the introduced MW field can be found in [39]. The system Hamiltonian, H_R^α, only needs to describe the transitions between the two RF-dressed states of interest, labelled as $|1\rangle = |F = 1, \bar{m}_F = -1\rangle$ and $|2\rangle = |F = 2, \bar{m}_F = 1\rangle$, separated by energy $\hbar\omega_0$, equivalent to the bare transition clock frequency $\hbar\omega_{\text{hfs}}$. The bar over the label of the state indicates that we are dealing with adiabatic RF-dressed states rather than bare atomic states. The formalism describing these states will be provided in the following sections of this chapter. The system is driven by an arbitrarily polarised MW field with Rabi frequency $\Omega_{MW,Rabi}$, detuning $\Delta_{MW} = \omega_{MW} - \omega_0$, and phase α

$$\hat{H}_R^\alpha = \Omega_{MW,Rabi} \left(\cos(\alpha)\hat{\sigma}_x + \sin(\alpha)\hat{\sigma}_y\right) + \Delta_{MW}\hat{\sigma}_z. \tag{2.26}$$

Here, $\hat{\sigma}_{x,y,z}$ are Pauli matrices and $\Omega_{MW,Rabi}$ is dependent on MW field amplitude as well as polarisation [1]. The interferometer sequence displayed in figure 2.3 consists of three MW pulses separated by time intervals T. First, a MW pulse prepares a superposition between $|1\rangle$ and $|2\rangle$ after which atoms are transported around the ring track for time T. At the halfway point, a MW π - pulse is applied to act like a mirror before the atoms are driven back to their initial position. Finally, after the atoms have returned, a third MW pulse performs the last $\pi/2$ - pulse to read out the Sagnac phase.

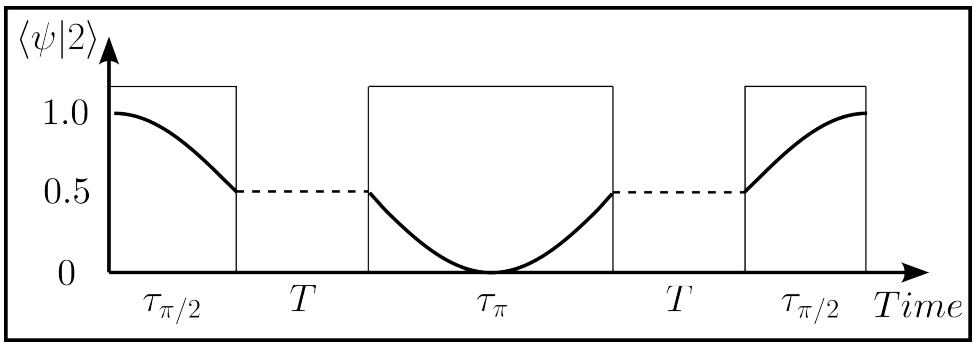

Figure 2.3: Expectation value evolution as a function of time during the experiment

The state evolution operator, $\hat{U}$, is represented as

$$\hat{U}^{\alpha}(\tau) = e^{-i\hat{H}_R^{\alpha}\tau}, \tag{2.27}$$

where τ is the length of a particular time period in the experimental sequence. The π - pulses are defined so that $\tau_{\pi,\frac{\pi}{2}} \times \Omega_{MW,Rabi} = \pi, \frac{\pi}{2}$. The evolution of time is described by operators that have $\Omega_{MW,Rabi} = 0$ and $\tau = T$, where T is the time interval between the π- and $\pi/2$- pulses. The total sequence applied to the initial state $|2\rangle$ transforms the wavefunction as shown below

$$|\psi_{Sagnac}\rangle = \hat{U}_{\frac{\pi}{2}}^{\alpha}\hat{U}(T)\,\hat{U}_{\pi}^{0}\hat{U}(T)\,\hat{U}_{\frac{\pi}{2}}^{0}|2\rangle\,. \tag{2.28}$$

The operators can be represented as rotations on the Bloch sphere in figure 2.4. During the free propagation time atoms can acquire different phases, indicated by multiple arrows on the Bloch sphere. This can happen due to atomic thermal motion within the trap. A π-pulse applied half-way through the free propagation stage minimises the dephasing effects.

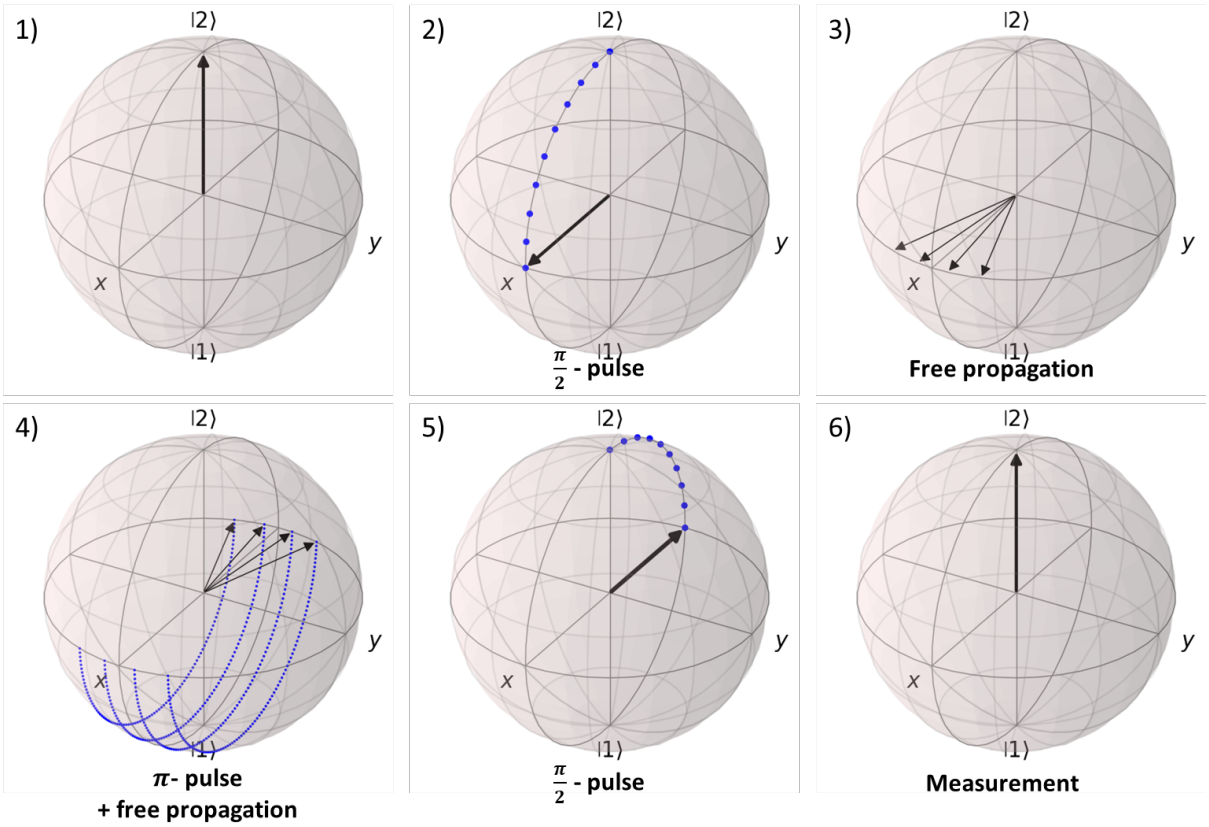

Figure 2.4: Ramsey sequence represented as rotations around the Bloch sphere. Black arrows indicate the state of the atoms and blue traces show the time evolution of the state during MW pulses.

2.4 RF-Atom Interactions

In this section, we will tackle the description of atomic spins interacting with DC and RF fields in order to shed some light on how the RF dressed potentials work. The total magnetic field, $\boldsymbol{B}_{tot}$, applied to the system can be split into static magnetic field and RF field contribution.

$$\boldsymbol{B}_{tot} = \boldsymbol{B}_{DC} + \boldsymbol{B}_{RF}(\omega t) \tag{2.29}$$

It is useful at this point to consider a frame of reference that rotates about the static field vector at Larmor precession frequency in order to look at the components of the AC magnetic field that have non-zero coupling terms. For this, we introduce circular components that will form a complete basis.

$$\hat{\boldsymbol{e}}_+ = \frac{1}{\sqrt{2}}\left(\hat{\boldsymbol{e}}_x + i\hat{\boldsymbol{e}}_y\right) \tag{2.30a}$$

$$\hat{\boldsymbol{e}}_- = \frac{1}{\sqrt{2}}\left(\hat{\boldsymbol{e}}_x - i\hat{\boldsymbol{e}}_y\right) \tag{2.30b}$$

$$\hat{\boldsymbol{e}}_\pi = \hat{\boldsymbol{e}}_z, \tag{2.30c}$$

where $\hat{\boldsymbol{e}}_+$ corresponds to σ_+ polarisation, $\hat{\boldsymbol{e}}_-$ to σ_-, and $\hat{\boldsymbol{e}}_\pi$ corresponds to π-polarised RF field. Also, from equation 2.22 we can work out the Larmor precession frequency for atoms in a fixed magnetic field.

$$\omega_{Larmor} = \frac{\mu_B g_F \hat{F}_z B_z}{\hbar} \tag{2.31}$$

We can define an arbitrarily polarised RF field, $\boldsymbol{B}_{RF}(t)$, oscillating at angular frequency ω_{RF}.

$$\boldsymbol{B}_{RF}(t) = \left(B_{RF+}\hat{\boldsymbol{e}}_+ + B_{RF-}\hat{\boldsymbol{e}}_- + B_{RF\pi}\hat{\boldsymbol{e}}_\pi\right) e^{i\omega_{RF}t} + c.c. \tag{2.32}$$

The Hamiltonian for magnetic field interactions, $\hat{H}_B$, is then expressed as

$$\hat{H}_B = \frac{\mu_B g_F}{\pi}\left(\hat{F}_z B_{DC} + \left(\frac{1}{\sqrt{2}}\left(\hat{F}_+ B_{RF+} + \hat{F}_- B_{RF-}\right) + \hat{F}_\pi B_{RF\pi}\right) e^{-i\omega_{RF}t}\right) + h.c., \tag{2.33}$$

where the angular momentum operators follow the relations below.

$$\hat{F}_\pi \left|F, m_F\right\rangle = m \left|F, m_F\right\rangle \tag{2.34a}$$

$$\hat{\boldsymbol{F}}^{\mathbf{2}} \left|F, m_F\right\rangle = F\left(F+1\right)\hbar^2 \left|F, m_F\right\rangle \tag{2.34b}$$

$$\hat{F}_\pm \left|F, m_F\right\rangle = \sqrt{\left(F \mp m_F\right)\left(F \pm m_F + 1\right)} \left|F, m_F \pm 1\right\rangle \tag{2.34c}$$

and

$$\left[\hat{F}_\pi, \hat{F}_+\right] = \hat{F}_+ \tag{2.35a}$$

$$\left[\hat{F}_\pi, \hat{F}_-\right] = -\hat{F}_- \tag{2.35b}$$

$$\left[\hat{F}_+, \hat{F}_-\right] = 2\hat{F}_\pi \tag{2.35c}$$

$$\left[\hat{\boldsymbol{F}}^2, \hat{F}_{\pm,\pi}\right] = 0. \tag{2.35d}$$

The derivation of these relations can be found in textbooks, such as the one by A. Messiah [47]. We apply a rotation operator that rotates about z-axis at Larmor precession frequency. The unitary rotation operator is represented by

$$\hat{U}_\pm = e^{i(\varphi + s\omega_{RF}t)\hat{F}_z}, \tag{2.36}$$

where the sense of rotation, $s = \pm$ is determined by the g-factor as

$$s = \frac{g_F}{|g_F|}. \tag{2.37}$$

Under this rotation, we can define the wavefunction ϕ.

$$\phi = \hat{U}_{\pm}\psi \tag{2.38}$$

which follows the time-dependent Schrödinger equation.

$$\hat{H}\psi = i\hbar\frac{\partial\psi}{\partial t} \tag{2.39}$$

From this we can obtain the time evolution of the wavefunction.

$$i\hbar\frac{\partial\phi}{\partial t} = i\hbar\frac{\partial\hat{U}_{\pm}}{\partial t}\psi + \hat{U}_{\pm}\hat{H}\psi = i\hbar\frac{\partial\hat{U}_{\pm}}{\partial t}\hat{U}_{\pm}^{\dagger}\phi + \hat{U}_{\pm}\hat{H}\hat{U}_{\pm}^{\dagger}\psi \tag{2.40}$$

Because $\hat{U}_{\pm}$ commutes with $\hat{F}_z$, this gives $\left[\hat{U}_{\pm}, \hat{F}_z\right] = 0$, and therefore $i\hbar\frac{\partial\hat{U}_{\pm}}{\partial t}\hat{U}_{\pm}^{\dagger} = -\hbar\omega_{RF}\hat{F}_z$. This result allows us to express the Hamiltonian in the rotating frame of reference as

$$\hat{H}_{rot} = i\omega_{RF}\hat{F}_z + \hat{U}_{\pm}\hat{H}_B\hat{U}_{\pm}^{\dagger}. \tag{2.41}$$

Plugging equation 2.33 into 2.41 gives

$$\begin{aligned}\hat{H}_{rot} = \frac{\mu_B g_F}{2}\Bigg(&\left(B_{DC} - \frac{\hbar\omega_{RF}}{\mu_B\left|g_F\right|}\right)\hat{F}_z + \left(B_{RF\pi}e^{i\pm\omega_{RF}t} + B_{RF\pi}^{*}e^{i\mp\omega_{RF}t}\right)\hat{F}_{\pi} \\ &+\hat{U}_{\pm}\left(\frac{1}{\sqrt{2}}\left(\hat{F}_{+}B_{+} + \hat{F}_{-}B_{-}\right)e^{-i\omega_{RF}t}\right)\hat{U}_{\pm}^{\dagger}\Bigg) + h.c..\end{aligned} \tag{2.42}$$

For an applied AC magnetic field at frequency ω_{RF}, there will be a static magnetic field which satisfies condition $\omega_{RF} = \omega_{Larmor}$. This resonant DC field, B_{res}, can be written as

$$B_{res} = \frac{\hbar\omega_{RF}}{\mu_B\left|g_F\right|} \tag{2.43}$$

We use the Baker-Campbell-Hausdorff equation [48] to take into account the terms $\hat{U}_{\pm}$.

$$e^{\alpha\hat{F}_z}\hat{F}_{\pm}e^{-\alpha\hat{F}_z} = e^{\pm\alpha}\hat{F}_{\pm} \tag{2.44}$$

This allows us to rewrite the Hamiltonian in the rotating frame of reference.

$$\begin{aligned}\hat{H}_{rot} = \frac{\mu_B g_F}{2} \Big(& (B_{DC} - B_{res})\, \hat{F}_z \\ & + \left(B_{RF\pi} e^{i\pm\omega_{RF}t} + B^*_{RF\pi} e^{i\mp\omega_{RF}t}\right) \hat{F}_\pi \\ & + \frac{1}{\sqrt{2}} \Big(\hat{F}_+ B_+ e^{(-1+s)i\omega_{RF}t} + \hat{F}_- B_- e^{(-1-s)i\omega_{RF}t} \\ & + \hat{F}_- B^*_+ e^{(1-s)i\omega_{RF}t} + \hat{F}_+ B^*_- e^{(1+s)i\omega_{RF}t} \Big) \Big),\end{aligned} \tag{2.45}$$

where s is defined in equation 2.37. By applying the rotating wave approximation it is assumed that all terms oscillating at high frequencies have zero effect on average and therefore can be dismissed. We can see that depending on the value of s only B_+ or B_- terms have no time dependency. This result indicates that atoms in $F = 2$ manifold with $s = 1$ are only coupled with σ_+-polarised RF field and atoms in the $F = 1$ states with $s = -1$ only interact with σ_--polarised field. The Hamiltonian can then be simplified to

$$\hat{H}^{\pm}_{rot} = \frac{\mu_B g_F}{2} \left((B_{DC} - B_{res})\, \hat{F}_z + \frac{1}{\sqrt{2}} \left(\hat{F}_\pm B_\pm + \hat{F}_\mp B^*_\pm \right) \right). \tag{2.46}$$

The effective magnetic field, $\boldsymbol{B}_{eff}$, that interacts with the atoms is

$$\boldsymbol{B}_{eff} = (B_{DC} - B_{res})\, \hat{\boldsymbol{e}}_z + \frac{1}{2} \left(B_\pm + B^*_\pm \right) \hat{\boldsymbol{e}}_x. \tag{2.47}$$

We can define a quantity defining RF detuning from the atomic resonance, Δ_{RF}, and the polarisation-dependent term, proportional to the Rabi frequency, Ω_{RF}.

$$\hbar\Delta_{RF} = \frac{\mu_B g_F}{2} (B_{DC} - B_{res}) \tag{2.48}$$

$$\hbar\Omega^{\pm}_{\mathrm{RF}} = \frac{\mu_B g_F \left| B_\pm \right|}{2} \tag{2.49}$$

From equation 2.47 we can see that in the rotating frame of reference the atomic spin is at an angle θ_{RF} with respect to the quantisation axis. The angle is determined by detuning and RF field strength.

$$\theta_{RF} = \arccos\left(\frac{-\delta}{\Omega_{\mathrm{RF}}}\right) + \frac{s-1}{2}\pi \tag{2.50}$$

The time-independent interactions between the atoms and the applied RF field are based on the fact that the atomic spin precession is fast enough to follow the changes in θ_{RF} as the atoms traverse the spatially variable magnetic field due to thermal motion. Experimentally, not being able to follow this condition results in atomic spins spontaneously flipping and leaving the trap. In order for the equations above to be valid, the condition for adiabatic state following must be followed.

$$\frac{\partial\theta_{RF}}{\partial t} << \omega_{Larmor} \tag{2.51}$$

The eigenenergies of this rotated Hamiltonian represent the magnetic field dependence of the energy levels. In this case, we need to consider the quantum number $\bar{m}$ rather than m_F because we work in the transformed frame of reference under the assumption that $B_{DC} - B_{res} >> 1$ where RWA is valid.

$$E_{F,\bar{m}} = -\mu_B g_F \bar{m} s \sqrt{\frac{|B_{\pm}|^2}{2} + (B_{DC} - B_{res})^2} \tag{2.52}$$

The eigenstates of $\hat{H}^{\pm}_{rot}$ will coincide with the states defined by $\hat{H}_{DC}$ in the non-resonant case; however, a multiple integer of photon energies has been added to make the eigenenergies cross where $\Delta_{RF} = 0$. Due to the perturbation terms this becomes an avoided crossing with the spacing between the eigenstates of $\hat{H}^{\pm}_{rot}$ being separated by $\hbar\Omega^{\pm}_{\mathrm{RF}}$ as seen in figure 2.5. The eigenstates of $\hat{H}^{\pm}_{rot}$ are superpositions of the unperturbed Hamiltonian's eigenstates, so it is not appropriate to discuss atoms that absorb single photons. Instead, we can say that the atomic states are dressed with the RF field.

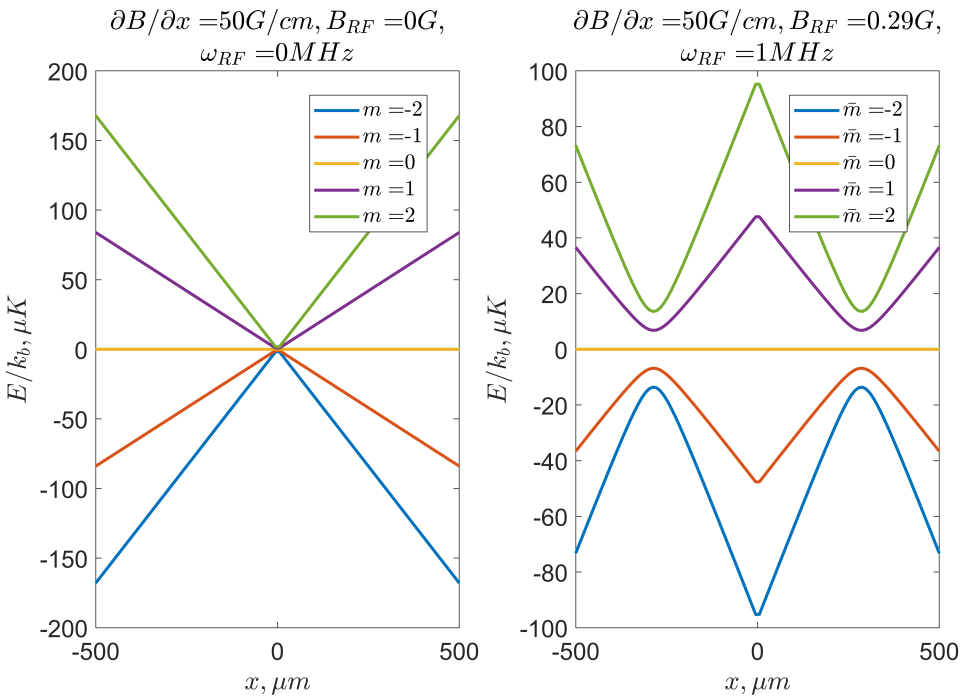

Figure 2.5: $F = 2$ bare state potential vs. RF-dressed potential in a 1D quadrupole trap.

In this picture the atoms traversing the resonant field region are adiabatically transitioning between different eigenstates of the unperturbed Hamiltonian, which results in the atoms being confined by a surface defined by the condition $\omega_{Larmor} = \omega_{RF}$. The transition probability for a two-level system is given by the Landau-Zener formula [49, 50].

$$P = 1 - e^{-2\pi\Gamma}, \tag{2.53}$$

where Γ is the adiabaticity coefficient given by

$$\Gamma = \frac{\omega_{Larmor}^2}{\frac{\partial \Delta_{RF}}{\partial t}} \tag{2.54}$$

Equation 2.54 tells us that the Larmor precession frequency, ω_{Larmor}, needs to be large to retain the atoms within the RF-dressed potential after many transits across the avoided crossing. This condition is hard to overcome in a quadrupole trap, since the majority of atoms will sit near zero-field region, where the Larmor precession frequency is small. We overcome this issue by placing the atoms into an Ioffe-Pritchard type trap which has a magnetic field zero replaced by a magnetic field minimum with nonzero value. Due to

technical reasons, the magnetic trap minimum field is selected to be such that the spurious harmonic components of the RF sources would not flip the atomic spins, thus preventing a loss channel.

We can now use these RF-dressed adiabatic potentials described in equation 2.52 to guide atoms in a state-dependent way to operate the Sagnac interferometer. The RF polarisation can have controlled spatial dependency with respect to the static magnetic field, which will be exploited to create dynamic atom traps.

2.5 State-Dependent Guide

The theory from the previous sections is combined to define a trap used to transport the atoms in a state-dependent way. The first thing to consider is the formation of purely magnetic DC trapping potentials, followed by the introduction of RF fields that will shape our trap and allow dynamic control of local trap minima. The trapping scheme is outlined in detail in [51].

The DC trap in our design is formed by running currents of equal magnitude in the four parallel wires running in counter-propagating directions. This forms an upright 2D quadrupole trap that extends along the parallel wires. The height at which the magnetic field zero occurs, z_0, is given by equation 2.55

$$z_0 = \frac{1}{2}\sqrt{4dG + 4G^2 - w^2}, \tag{2.55}$$

where w is the wire width, G is the gap between the axis of symmetry and the centre of the middle conductor, and d is the distance between the outer conductor and the nearest middle conductor, as described in Figure 2.6.

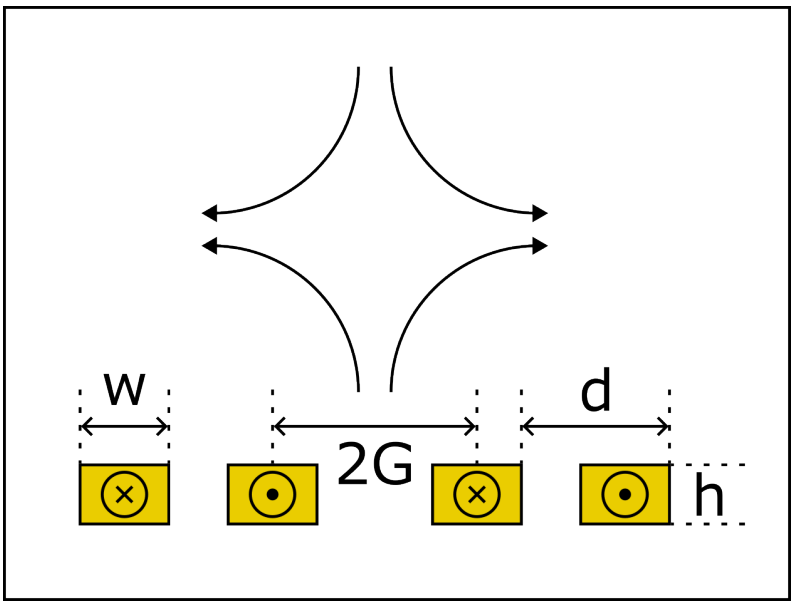

Figure 2.6: Schematic diagram of a 2D quadrupole created by four infinitely long conductors.

The field gradient in this case is given by

$$\frac{\partial B}{\partial z} = \frac{2\mu_0 I}{\pi} \frac{z_0 d}{G\,(d+G)\,(d+2G-w)\,(d+2G+w)}, \tag{2.56}$$

where μ_0 is the Bohr magneton. These calculations can be found in T. Bishop's thesis [16].

This infinite trap approximation can be used to create a trap geometry where the parallel wires form concentric rings rather than extend in straight lines towards infinity. In doing so, we can create a circular track required to operate the Sagnac interferometer.

Given that the radius R of the concentric wires is much larger than the extent of the trap, the magnetic field for this DC trap can be expressed in polar coordinates defined in figure 2.7.

$$\boldsymbol{B}_{DC} = qr \begin{pmatrix} -\cos\theta\cos\phi \\ -\sin\theta\cos\phi \\ \sin\phi \end{pmatrix} \tag{2.57}$$

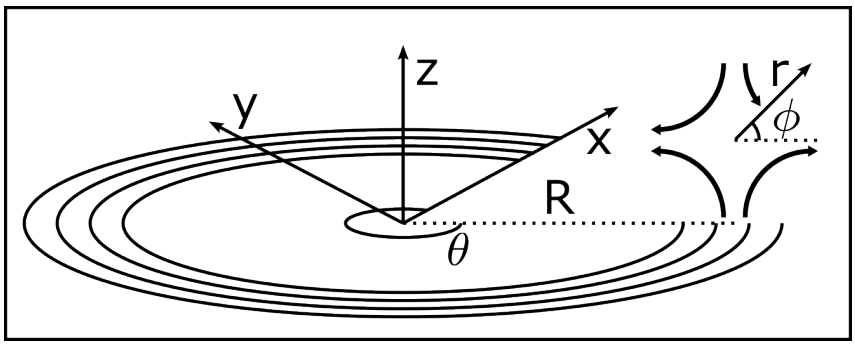

Figure 2.7: DC ring quadrupole diagram

Looking at equations 2.57 and 2.52 one can notice that by introducing an RF dressing field, the trapping potential confines the atoms at a fixed distance r_{res} from the DC field minimum. The value of r_{res} is determined by the condition $B_{DC} = B_{res}$ and, therefore, can be expressed as

$$r_{res} = \frac{1}{\partial B_{DC}/\partial r} \frac{\hbar\omega_{RF}}{\mu_B g_F}. \tag{2.58}$$

In a 3D quadrupole trap the dressing frequency defines a resonant shell surface that is observed by producing a frequency ramp from zero to a finite value. The size of the shell depends on the final value of ω_{RF} and the magnetic field gradient of the trap. In the figure 2.8, it can be seen that the shell radius increases when vertically polarised dressing field frequency is ramped up. It is also clear that the atoms leave the equator in the x-y plane and end up in the location where the static magnetic field is collinear with the RF dressing field polarisation, therefore, atoms end up at the poles because of the polarisation-dependent term in Equation 2.52. The RF field at the equator is perpendicular to the DC field and thus can be expressed as a superposition of field polarised along $\hat{\boldsymbol{e}}_+$ and $\hat{\boldsymbol{e}}_-$, whereas at the poles the only non-zero RF field component is $\hat{\boldsymbol{e}}_\pi$. This results in vanishing coupling regions at the top and bottom of the trap, where the atoms fall back into the centre of the DC quadrupole trap.

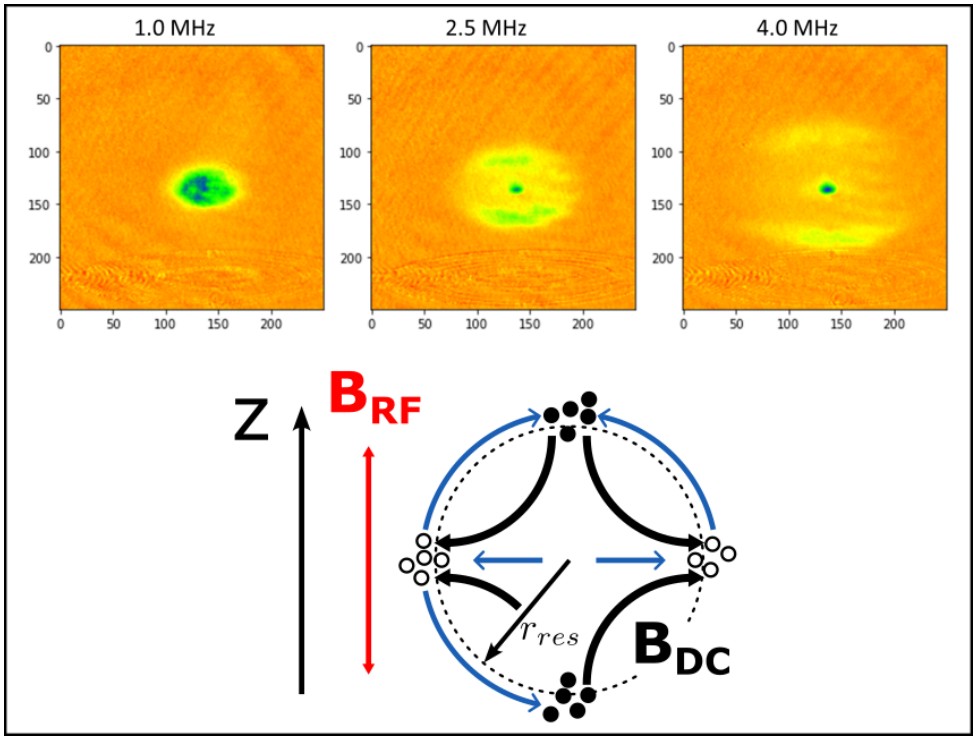

Figure 2.8: RF-dressed 3D quadrupole trap produced with a vertically polarised RF field. The top row shows false coulour absorption images of atoms with different dressing frequencies. The blue lines in the bottom diagram show the path that the atoms take and the black arrows show the DC magnetic field lines.

In a ring quadrupole trap the zero-coupling regions are eliminated by introducing an orthogonal field component pointing radially outward with a 90 degree phase shift. The

directions of the two field components produced by separate coils are shown in figure 2.9. As a result, an elliptically polarised RF field, called the smoke-ring field, is applied to the atoms. With this geometry, a potential minimum forms on a torroidal surface at distance $r = r_{res}$ from the centre of the DC quadrupole field. The total RF dressing field that creates a resonant torroidal potential is given by

$$\boldsymbol{B}_{RF}^{(t)} = \frac{a_+}{\sqrt{2}} \begin{pmatrix} \cos\theta \\ \sin\theta \\ i \end{pmatrix} \frac{a_-}{\sqrt{2}} \begin{pmatrix} \cos\theta \\ \sin\theta \\ -i \end{pmatrix}, \tag{2.59}$$

where a_+ and a_- are magnitudes of the orthogonal circular RF field components.

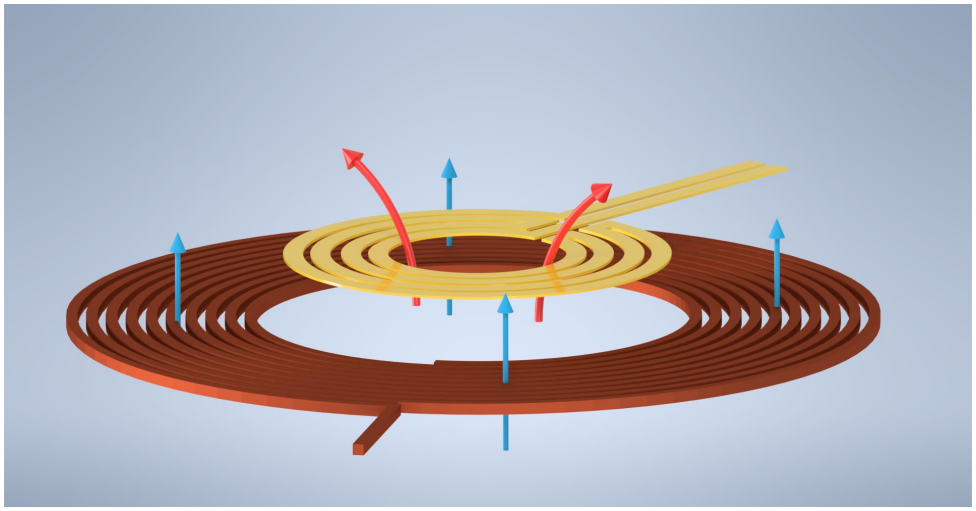

Figure 2.9: RF field produced by the copper RF chip in the radial direction (red) and vertically polarised RF produced by the PCB coil underneath (blue) create the smoke ring field $\boldsymbol{B}_{RF}^{(t)}$ above the gold atom chip wires.

The introduced RF dressing field is assumed to be uniform across the extent of the trap, so there are no potential variations due to RF field magnitude drop-off as we move away from the surface. The vertically polarised field produces a potential minimum at the location where the RF field is aligned with the DC field. The second, radially symmetric field is superimposed in the same location with a 90 degree relative phase shift to keep the atoms confined to the resonant surface. If we consider the atoms in the $F = 2$ states, only the projection of the AC field onto the $\hat{\boldsymbol{e}}_+$ component will interact with the ensemble. The magnitude of the coupled RF field at $r = r_{res}$ can be described by the equation below.

$$\left|B_{RF}^{(t)}\right|^2 = |\boldsymbol{B}_{RF}\cdot\hat{\boldsymbol{e}}_+|^2 = \frac{|a_+|^2+|a_-|^2}{+} + \frac{|a_+a_-|}{2}\cos\left(2\phi+\alpha\right), \tag{2.60}$$

where $\alpha = \arg(a_+) - \arg(a_-)$. For purely circular cases, where $a_+ = 0$ or $a_- = 0$, the potential minimum becomes independent of θ or ϕ, and therefore the RF field couples across the entire torroidal surface with equal strength. When $a_\pm > 0$, the dressing field becomes elliptical and the potential minima form at locations $\phi = \alpha/2$ and $\phi = \alpha/2 + \pi$. With linearly polarised RF we have conditions $a_\pm > 0$ and $a_+ = a_-$ leading to zero coupling regions where the atomic states become degenerate and atoms are lost from the trap. These configurations are represented in figure 2.10. With these considerations in mind, we chose an RF field that is elliptically polarised to localise the atoms at $\phi = \pm\pi/2$.

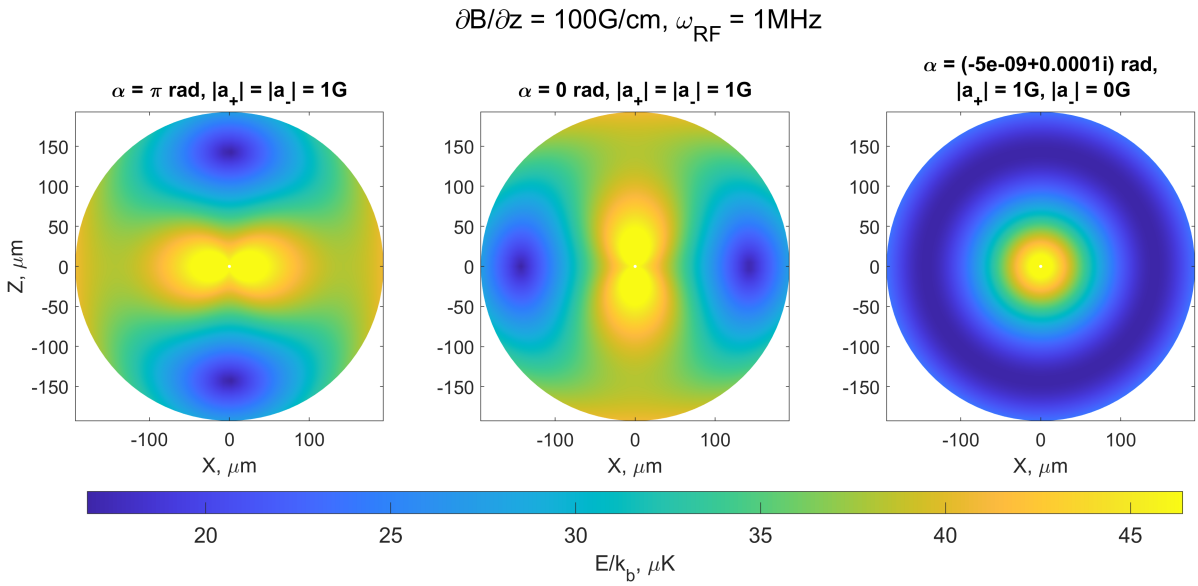

Figure 2.10: Cross-section view of an RF-dressed torroidal trap for $|F=2, \bar{m}_F = 1\rangle$ state. Changing the relative phase between the two circular RF components modulates the ϕ coordinate of the traps. Setting one of the two circular components to zero removes the localisation of the trapping potentials along ϕ.

The radial symmetry of this trap is broken by introducing another, much weaker, RF field that interferes constructively or destructively with the radial part of the smoke ring field as shown in figure 2.11. In this way, the atoms are still mainly confined to $\phi = \pm\pi/2$, but the confinement along θ is modulated. This symmetry-breaking field is called the multipole field and it allows one to produce potential minima along the extent of the circular trap. The multipole AC field can be written as

$$\boldsymbol{B}_{RF}^{(m)} = \left|B_{RF}^{(m)}\right| r^{n-1} \begin{pmatrix} \sin\left((n-1)\,\theta - n\theta_0\right) \\ \cos\left((n-1)\,\theta - n\theta_0\right) \\ 0 \end{pmatrix}, \tag{2.61}$$

where n is the order of the multipole field and θ_0 is an arbitrary rotation of the multipole field around the z-axis. The quadrupole order determines the number of minima created around the ring trap.

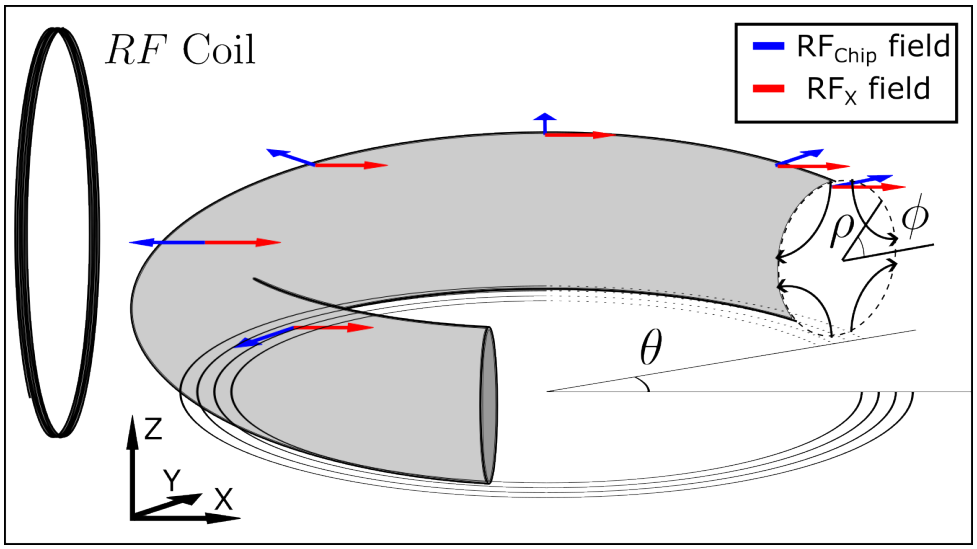

Figure 2.11: DC and RF fields forming the adiabatic RF-dressed ring lattice potentials. Only the radially symmetric part at $\phi = \pm\pi/2$ is contributing to confinement along θ.

The higher order quadrupole field produces trap minima with closer spacing; however, the trap depth decreases exponentially with n. One can superimpose two multipole fields of the same order, n, with $\theta_0 = 0$ and $\theta_0 = \pi/2n$ to create a multipole field with arbitrary in-plane polarisation. Such a combined field produces an RF field of general form which can be expressed in terms of circular components with arbitrary amplitudes $\mathcal{U}_{\pm}$

$$\boldsymbol{B}_{RF}^{(g)} = \frac{\mathcal{U}_+}{\sqrt{2}} \left(re^{i\theta}\right)^{(n-1)} \begin{pmatrix} i \\ 1 \\ 0 \end{pmatrix} + \frac{\mathcal{U}_-}{\sqrt{2}} \left(re^{i\theta}\right)^{(n-1)} \begin{pmatrix} i \\ -1 \\ 0 \end{pmatrix}. \tag{2.62}$$

We then project the RF field onto the $\hat{\boldsymbol{e}}_+$ component to observe the effects of the AC field on the atoms in the $F = 2$ manifold.

$$\begin{aligned} B_+^{(g)} &= \boldsymbol{B}^{(g)_{RF}} \cdot \hat{\boldsymbol{e}}_+ \\ &= -\mathcal{U}_+ r^{(n-1)} \frac{1+\sin\phi}{2} e^{-in\theta} + \mathcal{U}_- r^{(n-1)} \frac{1-\sin\phi}{2} e^{in\theta} \end{aligned} \tag{2.63}$$

One can see that for $\phi = \pi/2$ the RF field is pointing along the z-direction and the $\mathcal{U}_-$ term becomes zero while $\mathcal{U}_+$ becomes maximised. The opposite happens at $\phi = -\pi/2$ and $\mathcal{U}_+$ vanishes completely. The ring lattice structure can be reproduced by looking at the vector sum of the smoke ring field and the multipole field projected onto $\hat{\boldsymbol{e}}_+$.

$$\begin{aligned} |B_+|^2_{\phi=\pm\frac{\pi}{2}} &= \left| B_+^{(m)} + B_+^{(t)} \right|_{\phi=\pm\frac{\pi}{2}} \\ &= \frac{\left(a_+ + a_-\right)^2}{4} + \left|\mathcal{U}_\pm r^{(n-1)}\right|^2 + \left(a_+ + a_-\right) \left|\mathcal{U}_\pm r^{(n-1)}\right| \sin\left(n\theta \mp \varphi_\pm\right) \end{aligned} \tag{2.64}$$

Considering $\hat{\boldsymbol{e}}_-$ we can get a full picture of how potentials behave in both F manifolds. We find that in this particular configuration, where the traps are formed at $\phi = \pm\pi/2$, the effects of the two circular RF components coupling to the atoms are completely decoupled. Following this, the polarisation of the RF field determines the location of potential minima around the trap for the $F = 1$ and $F = 2$ traps completely independently of each other. The RF-dressed potentials can be used to drive the atoms around a circular trap in a state-dependent fashion by changing the polarisation of the multipole field. This is achieved by applying two linearly polarised RF fields in the plane and changing their amplitude as well as their phase relative to $\boldsymbol{B}_{RF}^{(t)}$. Atom transport is already possible with only one multipole RF source; however, the position of the traps in $F = 1$ manifold will not be decoupled from the position of the traps in $F = 2$, making the gimballing of the system impossible.

2.5.1 Numerical Simulation

A numerical approach can be used to determine the trapping potential across the entire resonant surface. With a DC field pointing in various directions across the trap volume, we can rotate an arbitrary RF field into a frame aligned to the local field direction and rotating at the local Larmor frequency to numerically calculate the coupling strength of the RF field components. We look at the DC field direction in every point and estimate the rotation required to get the vector to align with the z-axis in the new frame of reference, shown in figure 2.65. The DC field vectors in our case can be described by equation 2.57. The angles θ and ϕ are defined in figure 2.7.

The rotation applied to the system at each point in space first aligns the DC field vector with the x-z plane by applying rotation around the z-axis, $U_z(-\theta)$, by an angle $-\theta$, and then another rotation around the y-axis, $U_y(-\phi)$, by an angle $-\phi$.

$$\boldsymbol{B}'_{DC} = U_y(-\phi)\, U_z(-\theta)\, \boldsymbol{B}_{DC} = |B_{DC}|\, \hat{e}'_z \tag{2.65}$$

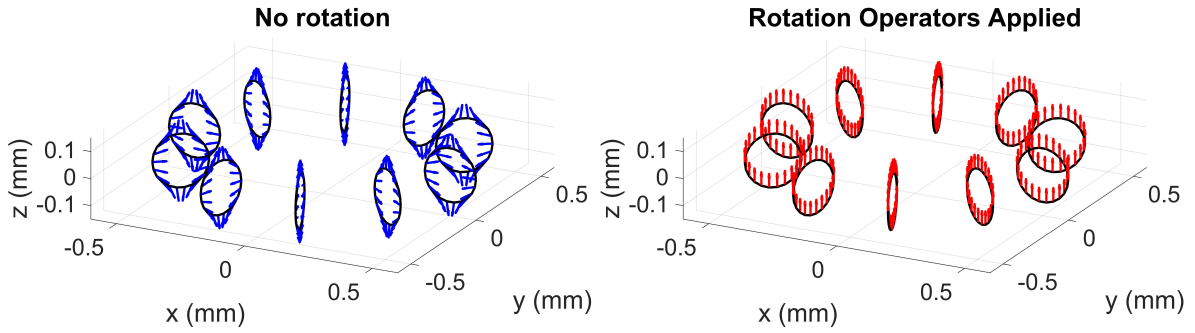

Figure 2.12: DC fields of a ring quadrupole potential at the resonant surface represented as vectors with no active transformations on the left and with $U_y(-\phi)\, U_z(-\theta)$ applied to $\mathbf{B}_{DC}$ on the right.

The same rotation operators are applied to the applied RF field and only the contribution of σ^+ is taken into account when estimating $|B_{RF}|$. This rotation leads to a complex potential landscape seen in figure 2.13 which can be shaped by changing the polarisation of the applied RF field.

$$\boldsymbol{B}'_{RF} = U_y\left(-\phi\right) U_z\left(-\theta\right) \boldsymbol{B}_{RF} \tag{2.66}$$

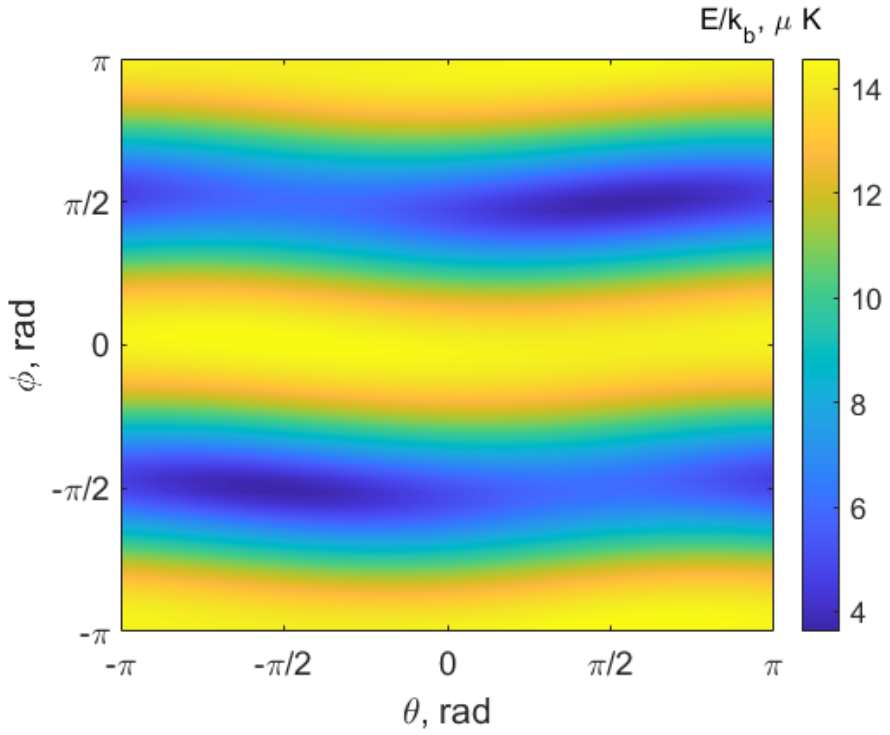

Figure 2.13: RF dressed ring quadrupole trapping potential for atoms in state $|F = 2, \bar{m}_F = 1\rangle$. The Rabi frequency associated with z-field is 300 kHz, 100kHz with radial field, and 25kHz with RF field in x-direction.

Chapter 3

Experimental Setup

This chapter covers the practical aspects of putting the setup together. There are many pieces of equipment that need to be adjusted and timed just right to provide any sign of results. The experimental setup can be separated into several broad categories, including analogue and digital control, vacuum setup, laser delivery system, DC field generating structures, RF setup, and control electronics. We will begin by exploring the conductor structures, starting from the largest ones outside the vacuum chamber and ending with microfabricated wires inside spanning only 40μm across. Then we will have a look at RF & MW electronics that drive AC magnetic fields with high precision before we move on to the vacuum system description. Finally, we will cover the laser system and the optics required to prepare cold atomic ensembles as well as atom probing.

At the heart of the experiment is the atom chip assembly, containing the electromagnet chip (EM chip), the RF chip, and the ultra-high-vacuum compatible PCB bonded together and mounted onto a CF-160 vacuum flange. As seen in Figure 3.1, there are also out-of-plane RF coils and a MW antenna placed close to the PCB. The entire flange is placed inside the vacuum chamber upside down to prevent Rb atoms from falling onto the surface and introducing contamination. Laser light is delivered through the side windows and a large viewport at the bottom of the chamber.

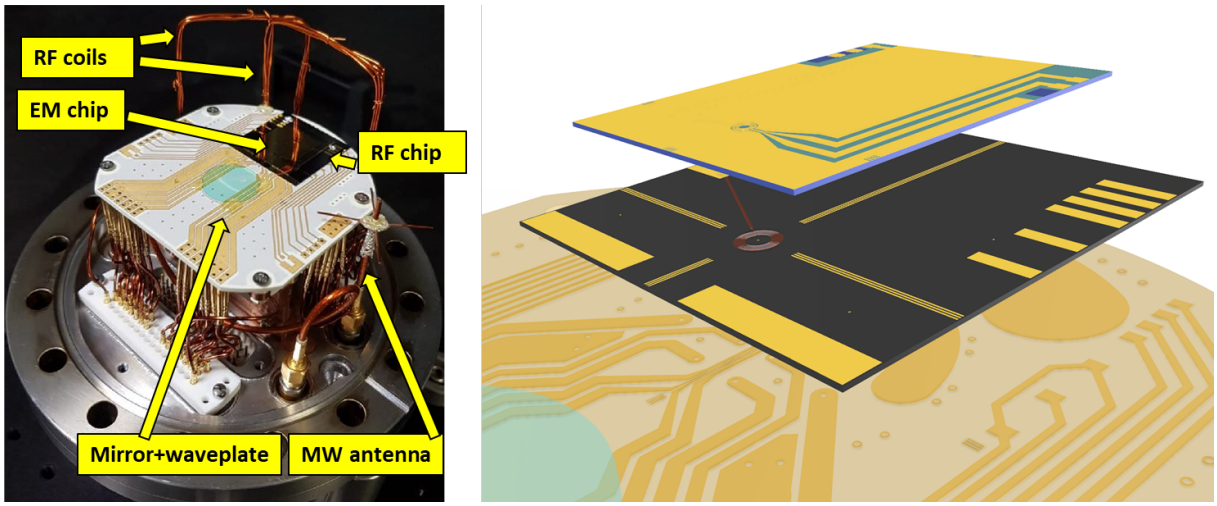

Figure 3.1: Experimental setup on a CF-160 flange.

The entire experiment is controlled by a National Instruments PXI system which incorporates a computer and an FPGA into a 19-inch rack-mounted enclosure. The block diagram of all connections to the PXI system is given in figure 3.2. The PXI system produces analogue and digital signals with 2μs resolution and allows the user to interact with the experiment via the LabView interface. Analogue signals control currents in wires, laser frequency, and MW/RF signal amplitudes. The digital channels are responsible for relay switching, actuating mechanical shutters, enabling laser output, setting the RF frequency ramps, and switching MW/RF output.

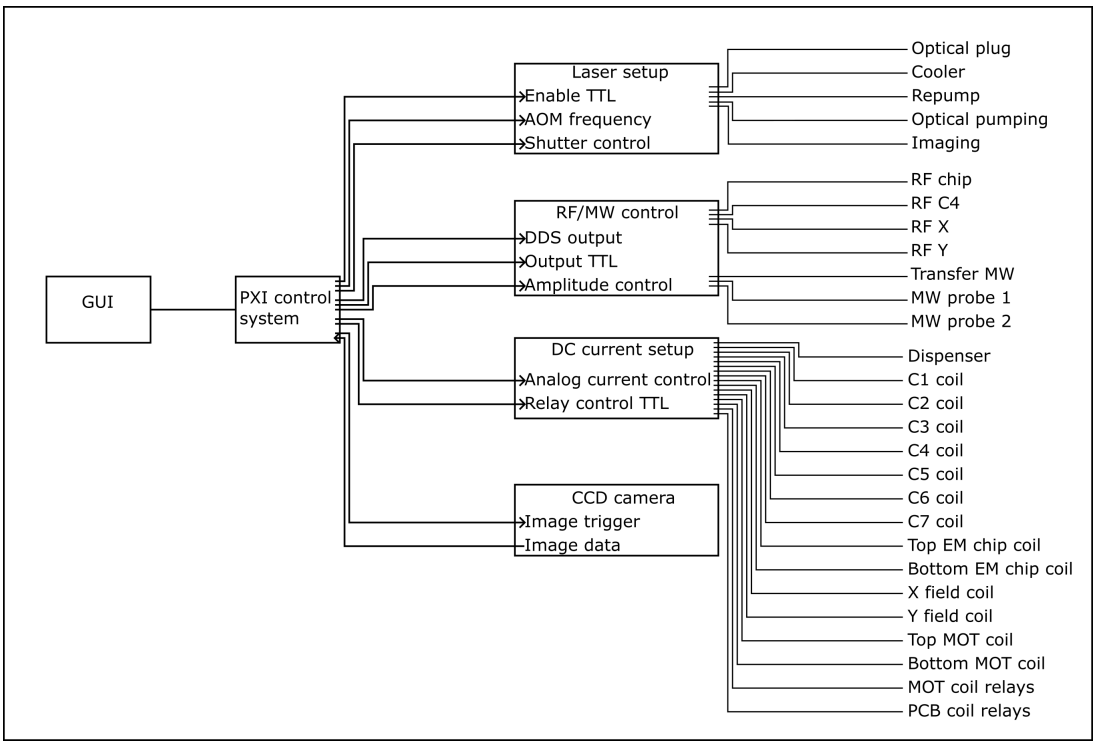

Figure 3.2: PXI system control diagram.

3.1 Conductor Structures

3.1.1 External Coils

There are three pairs of external coils present in the setup. The first pair is a set of two circular coils in anti-Helmholz configuration, producing magnetic fields for the magneto-optical trap. The MOT coils have 240 turns in each of them (20 layers with 12 windings each) with a rectangular wire cross section of $3.15 \times 1.4\text{mm}^2$, internal diameter of 80mm, outer diameter of 115mm, and nominal height of 46mm. The coils are driven independently by Keysight N5745A power supplies. We control each coil separately, because that allows us to change the vertical position of the quadrupole field should the need for it arise. To prevent the MOT coils from overheating, they have been placed between cooling plates that run cold water through them.

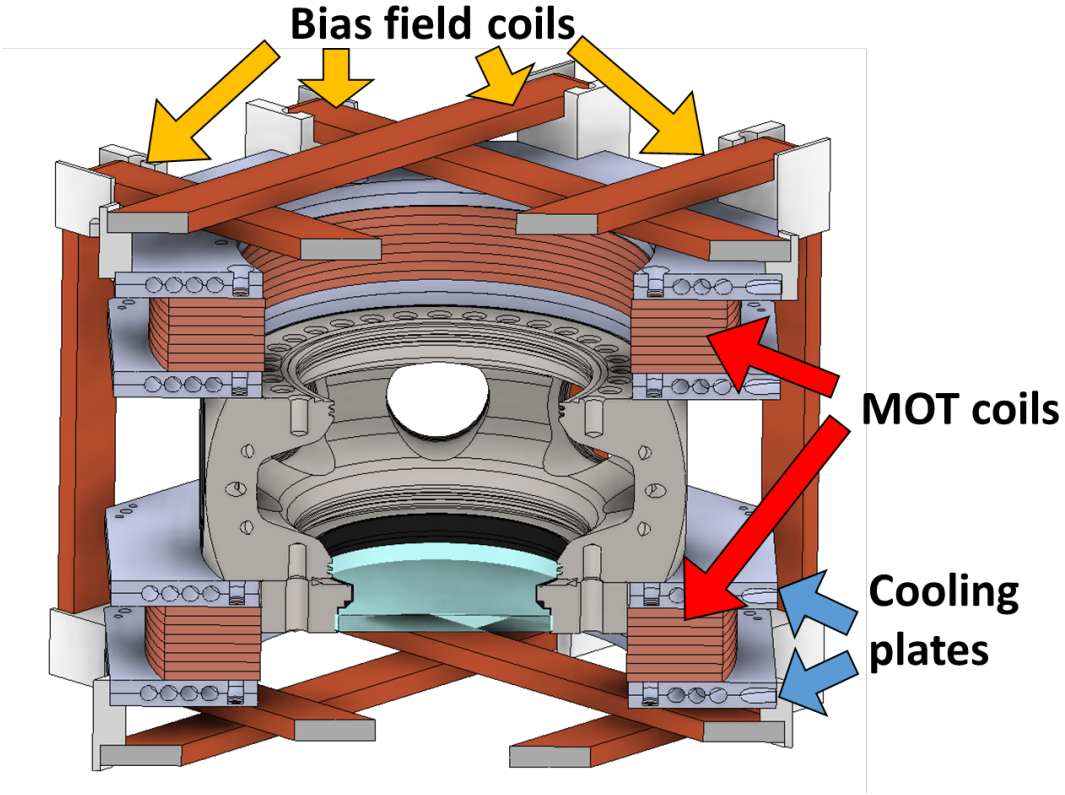

Figure 3.3: External coil configuration.

The temperature stability is especially important when trying to switch the inductive coils off and on in a very quick succession. The high inductance of the coils combined

with the changing resistivity of the wire leads to changes in the current rise and fall times. The timing of the recapture stage might drift by as much as 10ms without proper thermal management, causing the position of the magnetic trap and free falling atoms to miss each other and losing atoms from the trap as a result. Also, smoother recapture of atoms with tight timing tolerances can affect the final temperature of the trap because shaking the trap can excite vibrational modes within the atomic ensemble, leading to parametric heating.

The MOT coils have automotive relays connected in series to completely stop current flow during the late stages of the experiment. This is done because even when the power supplies are set to output no current, a small amount of residual current still affects the lifetime of the atom cloud near the chip surface. The relays are only actuated when the drive current is low to prevent relay arcing, which can weld the relay contacts shut and damage the power supplies.

The remaining two pairs of external coils produce the field in the same direction, thus producing uniform magnetic fields that can be used to adjust the position of the magnetic atom trap. The coils take a rectangular shape to minimise the distance between the conductor and the science region within the vacuum chamber. The coil pair that produces the bias field in the y-direction is wound first, because it needs to displace the quadrupole trap by a distance of 2.5 cm. Keeping the wires closer to the chamber creates larger magnetic fields and makes the setup more efficient. The coil pair that produces bias fields in the x-direction only needs to slightly adjust the position of the trap by a few millimetres rather than move it over relatively large distances. Both sets of coils are also used in the final ring quadrupole trap to cancel out any stray magnetic fields present in the lab. The compensation coils are driven by bipolar KEPCO BOP 20-20ML power supplies using their analogue input.

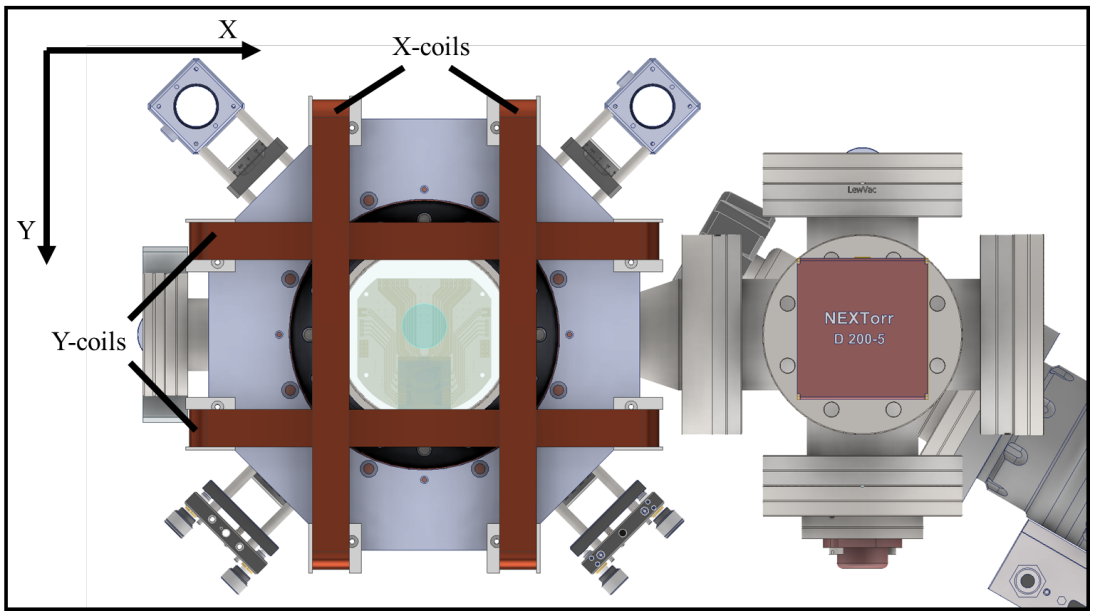

Figure 3.4: Top view of the setup external compensation coils highlighted.

3.1.2 The PCB

The vacuum-compatible PCB inside the vacuum chamber is the intermediate structure, meant to aid the transfer of atoms from the magnetic trap, generated by the large MOT coils, into the atom chip trap, which is less than a millimetre across. The circuit board shown in figure 3.5 is made of 12 conductor layers, 10 of which contain wires that form 7 concentric coils, labelled C1 - C7, going from C1 being the largest, and C7 being the smallest. The coils of decreasing radius can produce higher magnetic field gradients close to the PCB surface, thus increasing the evaporative cooling efficiency. Each coil is connected to individual uni-polar power supplies to provide more control over the generated magnetic field potentials. We found experimentally that it is more useful to run the coils C1 & C2 in reverse to produce a magnetic quadrupole field without the use of any external magnetic fields. The inherent symmetry of the PCB locates the atoms directly beneath the science region of the atom chip, making the chip trap loading procedure possible. The PCB also contains connections required to pass the DC and RF currents to RF and electromagnet (EM) chips.

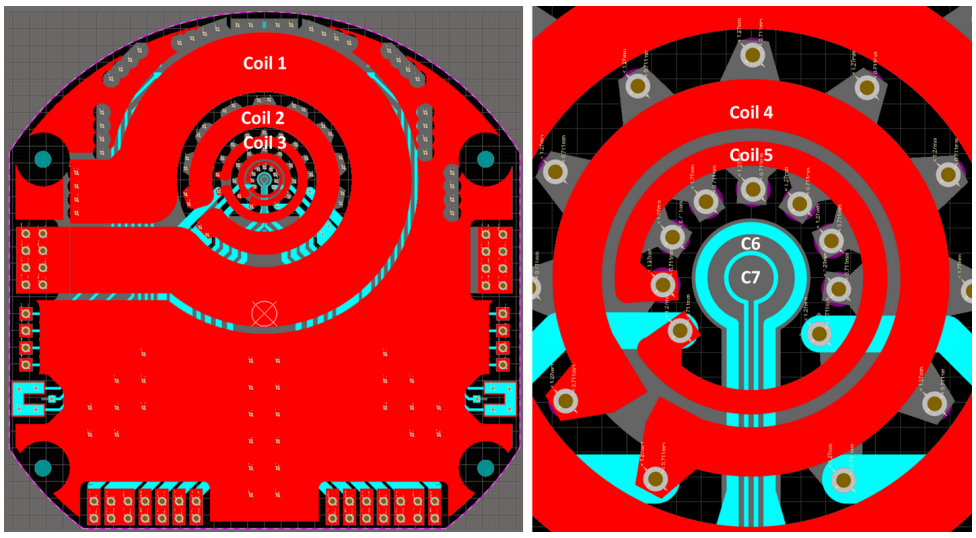

Figure 3.5: PCB coils

Some of the PCB coils also have home-built bias tees connected on the outside to allow RF current injection without disrupting the normal operating mode of the coils during the transport stage. Coil C4 runs the RF current through it to produce a vertically polarised RF field, which contributes to the formation of the RF-dressed ring lattice trap.

3.1.3 RF Antennae

The out-of-plane RF antennas were added to the setup to produce a linearly polarised RF field which can interfere with the radial field components as described in previous sections. The antennas are square-shaped with a side length of 5 cm, made of 0.5mm^2 wire with 5 turns each. The windings are attached to the PCB at a shallow angle because they would interfere with the optical path of the MOT beams otherwise. Only one antenna is required for state-dependent transport, hence, the RFx coil is connected to a high-power RF amplifier and the RFy coil is used for low-power probing and cooling.

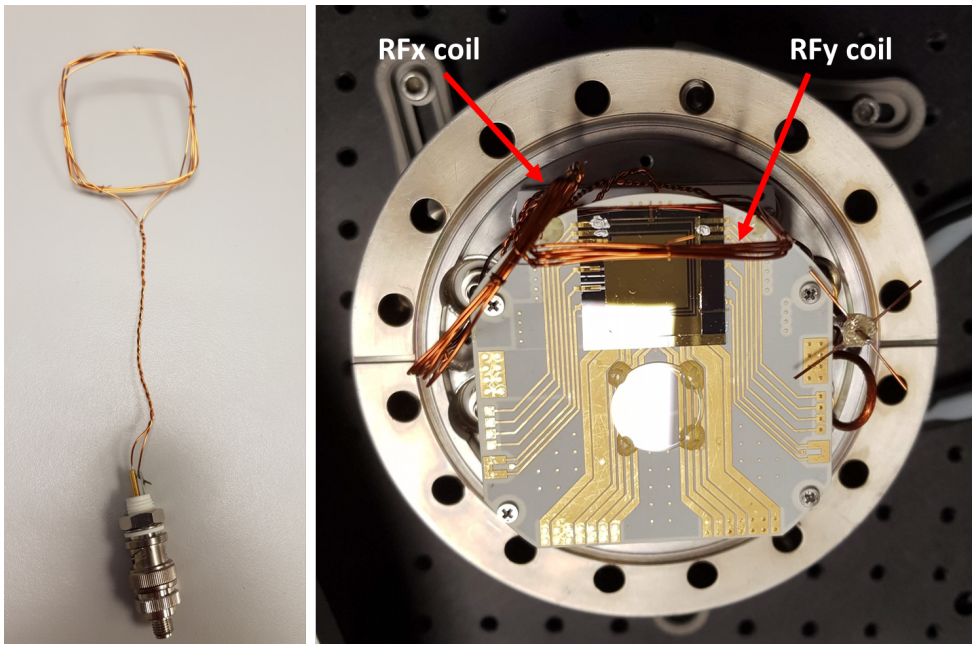

Figure 3.6: RF coils are attached to the PCB using UHV-compatible adhesive.

3.1.4 The RF Chip

The RF chip produces the radial field component required for the creation of the RF-dressed potentials. The design presented in figure 3.7 features two spiral coils with 10 turns each connected through the central via. The wires on this 280μm silicon chip are formed on each side by etching a 40μm deep groove and filling it with electroplated copper. The conductor width is 40μm, which gives it the effective cross-sectional area of 0.0016mm^2. Current vs. voltage measurements show that the DC resistance of the chip is 5.753Ω.

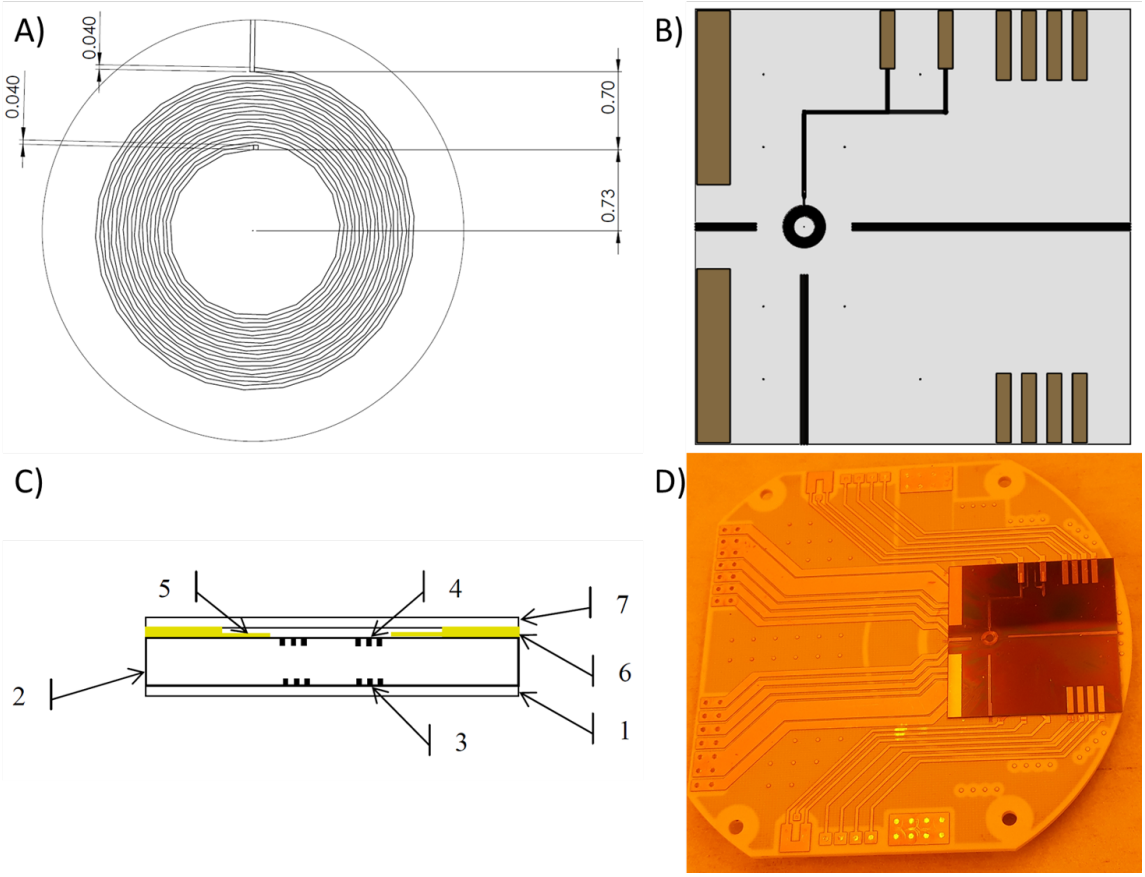

Figure 3.7: A) Drawing of the RF chip spiral; B) Top view diagram of the RF chip; C) The layers of the RF chip: 1. Protective SiO_2 layer (1μm); 2. Si susbtrate (280μm); 3. Bottom copper tracks (40μm); 4. Top copper tracks (40μm); 5. Gold alignment marks (100nm); 6. Gold pads (2μm); 7. Protective SiO_2 layer (1μm); D) The RF chip bonded on the PCB.

For AC applications, we use a vector network analyser to determine the chip's complex impedance. An RF transformer and a matching network are then specifically tuned to maintain the resonance condition of the coil at the driving frequency.

3.1.5 The Electromagnet Chip

The EM chip seen in figure 3.8 is a 2-layer design on a 280μm silicon substrate with the lead wires rotated 180 degrees from each other. This way the influence of the lead wires is eliminated by swithing to a different layer before the atoms get close to discontinuity. The design of the coils is based on equations 2.55 and 2.56. The vertical separation between the two layers was taken into account to maintain the same magnetic field gradient and ensure maximal trap overlap along the z-axis. The wires with counterpropagating currents are connected in series to reduce common-mode noise at the cost of not being able to control the position of the ring quadrupole field.

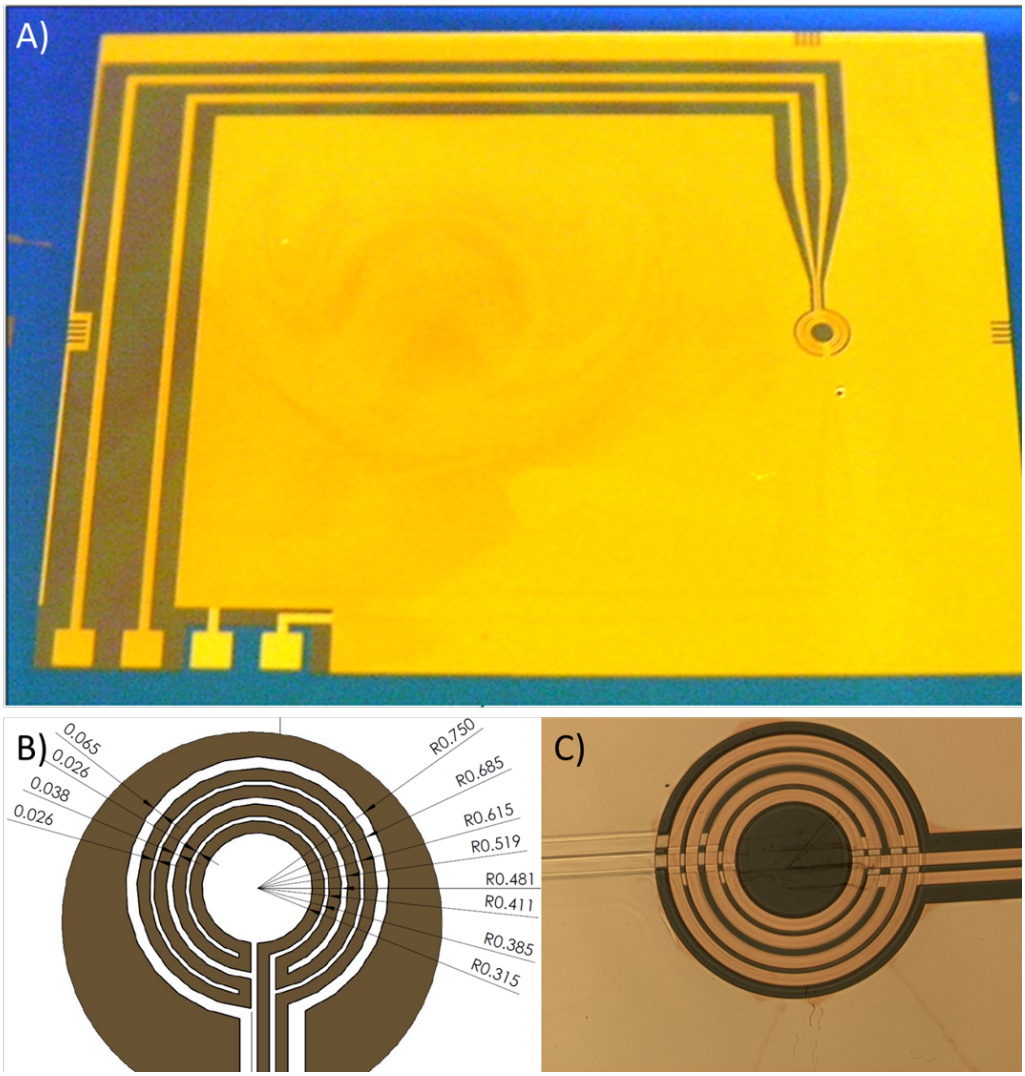

Figure 3.8: A) Picture of the electromagnet chip in the fabrication room. The gold on the chip surface acts as a mirror; B) Diagram of the EM chip top loop; C) Close-up microscope picture of the EM chip.

The gold conductor layers are evaporated on the surface under vacuum conditions until a thickness of 2μm is achieved. The layout of the layers is given in figure 3.9. The top layer of the EM chip also has 2μm gold evaporated on the remaining part of the substrate surface to form a mirror surface that is used to image the atoms by reflecting the laser light off the surface.

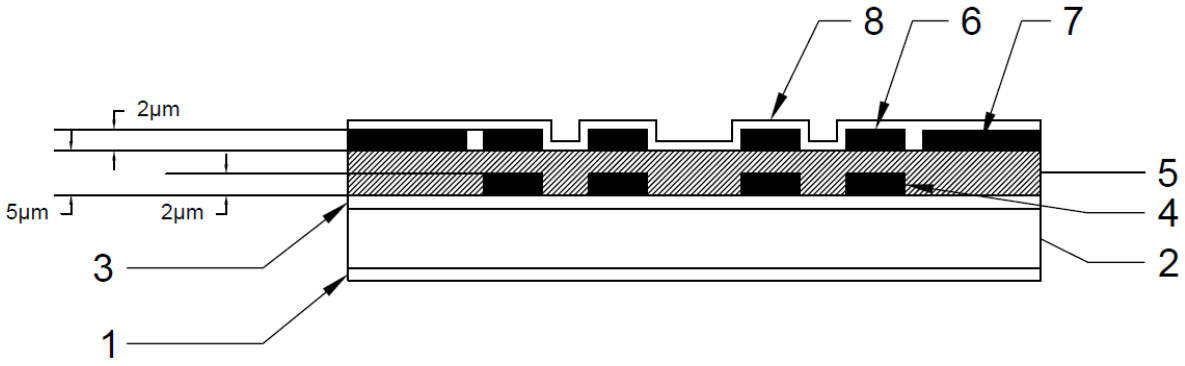

Figure 3.9: The layers of the EM chip are as follows: 1. Protective SiO_2 layer; 2. Si susbtrate (280μm); 3. Protective SiO_2 layer; 4. Bottom gold rings, (2μm); 5. SU-8 panarization layer, (5μm); 6. Top gold rings (2μm); 7. Gold mirror layer (2μm); 8. Protective SiO_2 layer (40nm)

3.2 RF & MW Electronics

3.2.1 RF Generation

The experiment uses eight phase-locked RF channels coming from two PCBZ evaluation boards based on the AD9959 chip from Analog Devices. Each of the boards features 4 RF outputs with 10-bit DAC, 32-bit frequency resolution, and a maximum output frequency of 500MHz. The clock reference for these boards is provided externally. We have found that the 10MHz clock provided by the PXI system was suffering from phase noise problems, which, as seen in figure 3.10, were eliminated by replacing the clock reference with the Stanford Research Systems CG 635 digital clock synthesiser. The phase noise measurements were performed using the HP 8563E spectrum analyser and data were collected using open source automated measurement routine software [52]. Both the PXI system and the reference clock share the same oven-controlled, GPS-stabilised 10 MHz oscillator (Jackson Labs Fury).

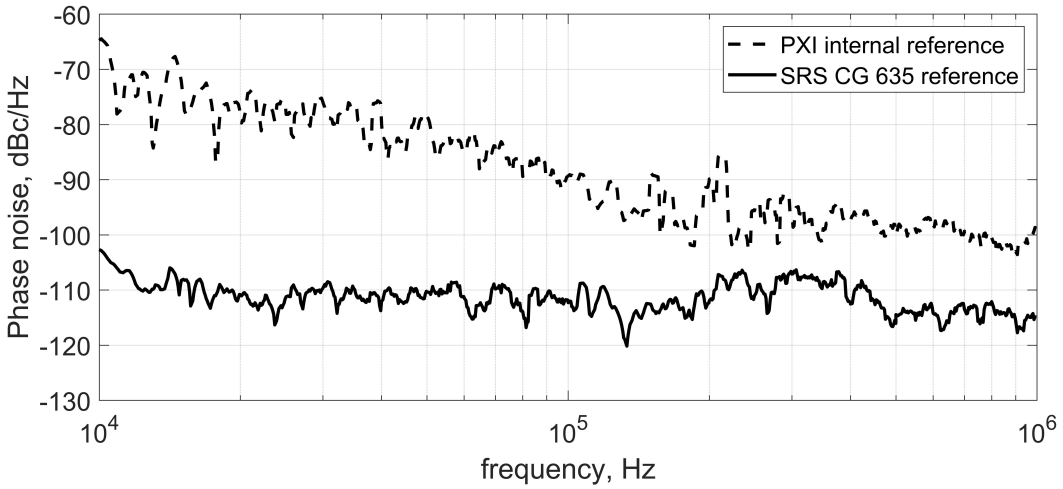

Figure 3.10: AD9959 phase noise measurement.

There are four RF output channels dedicated to generating the RF fields required to produce RF-dressed potentials. The RF outputs are equipped with switches, voltage-controlled attenuators, and amplifiers outlined in the figure below.

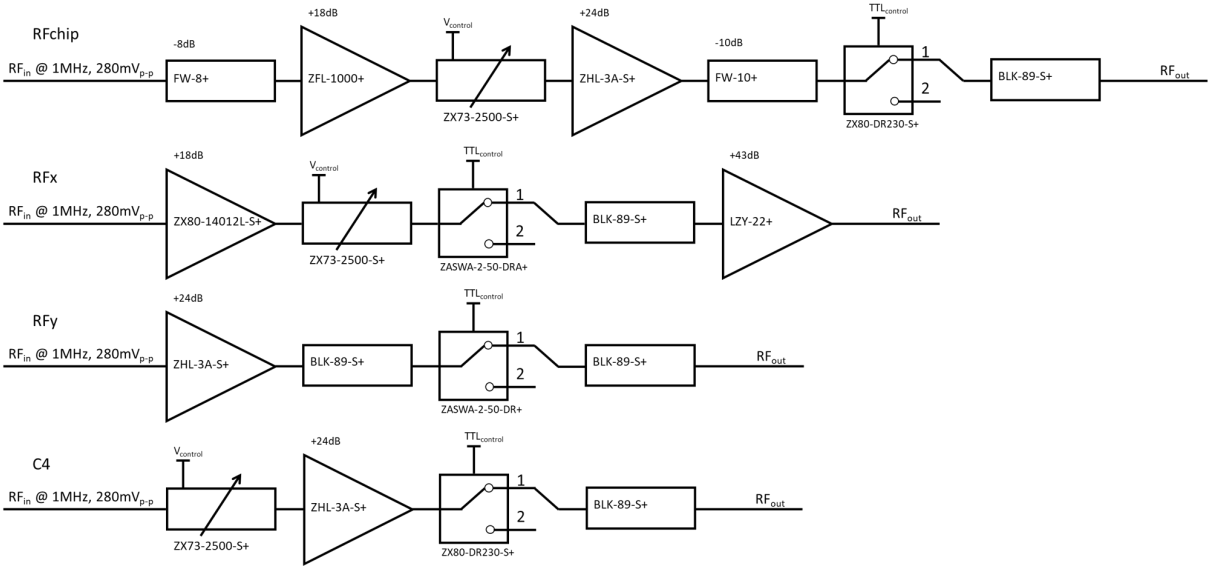

Figure 3.11: RF electronics setup

The need for voltage controlled attenuators comes from technical hardware limits that cannot produce long amplitude ramps directly from the DDS while the switches are used to make sure that no noise is introduced near the atoms when the channel is not in use.

3.2.2 Impedance Matching Electronics

The impedance of each RF coil is matched to 50Ω at 1 MHz with a corresponding LC network. We determined the impedance of each coil with a vector network analyser (Rhohe & Schwarz ZNB 20) and used open source analytic software [53] to determine the approximate values of the series and shunt components required to match the resonance condition. Since the coils are symmetric (source and ground connections can be swapped without affecting the operation mode), they are treated as balanced antennae, which require unbalanced-balanced transformers to function properly with our amplifiers. The impedance matching PCB board contains a manually wound transformer to get the real part of the load impedance close to 50Ω. The circuit is then further tuned by placing through-hole capacitors in series or parallel to remove the imaginary component as presented in figure 3.12.

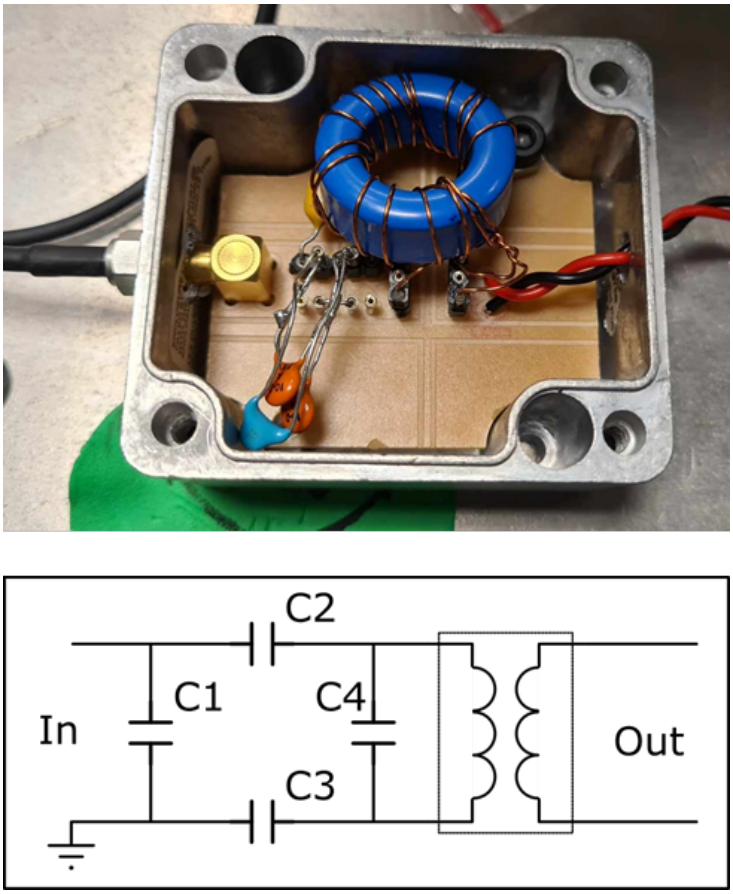

Figure 3.12: Impedance matching circuit diagram.

3.2.3 MW Setup

We have a selection of antennas that can be used to generate the MW fields necessary for the experiment. Some of these are commercially available, while others are home-built. The most basic antenna we have is the home-built UHV-compatible monopole antenna, which seen in figure 3.13. It has the advantage of being small and compact, and being very close (2 cm) to the atom chip. However, the magnetic field polarisation is fixed to be linear and parallel to the x-y plane, and the antenna has poor directivity, resulting in most of the MW power being wasted. Tuning this antenna is relatively straightforward; simply shorten the length of the central stub to satisfy the condition ($l = \lambda/4$) to increase the resonant frequency.

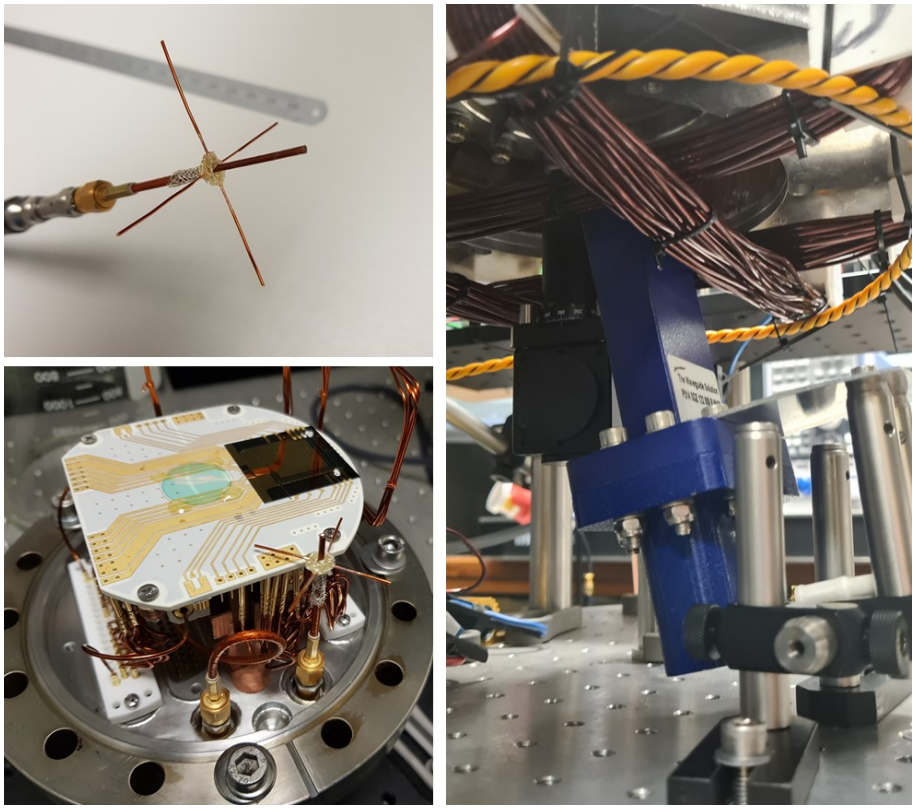

Figure 3.13: A Microwave monopole antenna is easy to build from UHV-compatible components and is close to the atom chip. A MW horn needs to be placed outside the vacuum chamber.

Other MW antennae may only be placed outside the vacuum chamber because some materials in the antenna are incompatible with the vacuum system. All external MW sources are placed underneath the vacuum chamber, where a CF-160 window allows the

MW fields to pass through. The commercially available MW horn has better directivity than the monopole antenna, with the magnetic field produced by this source being linearly polarised in the x-y plane.

Lastly, with the help of MATLAB's Antenna Designer tool, we designed a pair of helical antennas with left- and right-handed helicity as shown in figure 3.14. When driven with the same power and frequency, the right-handed antenna would not drive any Rabi cycles, while the left antenna would transfer atoms between F=1 and F=2 manifolds with high efficiency. The coupling strength of the MW field depends on the MW polarisation and the chosen transition. The theory behind MW interactions is covered in chapters 4 and 5. Since it is not obvious which MW transition is going to be used from the beginning, it is useful to have both antennae available to us.

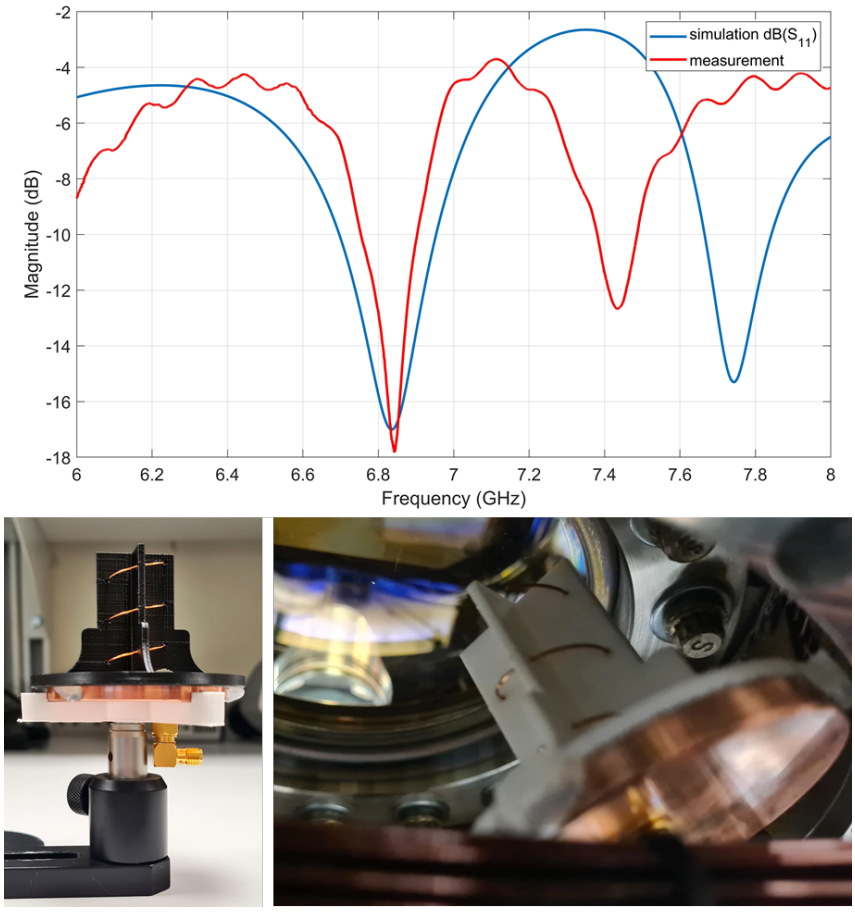

Figure 3.14: Helical antennae used to to produce circularly polarised MW fields. Top graph shows simulated vs. measured S11 component of a right-handed antenna (black). The left-handed antenna shaper printed in white PLA filament can be seen placed under the vacuum chamber window.

The MW electronics used to drive the antenna are outlined in the figure 3.15. We use a MW source with fixed frequency as a local oscillator, which is mixed with the RF signal produced by one of the DDS channels. The mixing products of the MW and RF frequencies produce sidebands, the lower of which is passed through a narrow-band filter cavity and then to a high-power MW amplifier. Multiple RF signals can be combined to produce several sidebands; however, the magnitude of each sideband becomes difficult to predict. We mainly use the monopole antenna for the MW generation, and the MW horn is set up under the vacuum chamber viewport as a pick-up to adjust the power of each sideband to make consistent measurements. The signal picked up by the MW horn is fed to a spectrum analyser for evaluation.

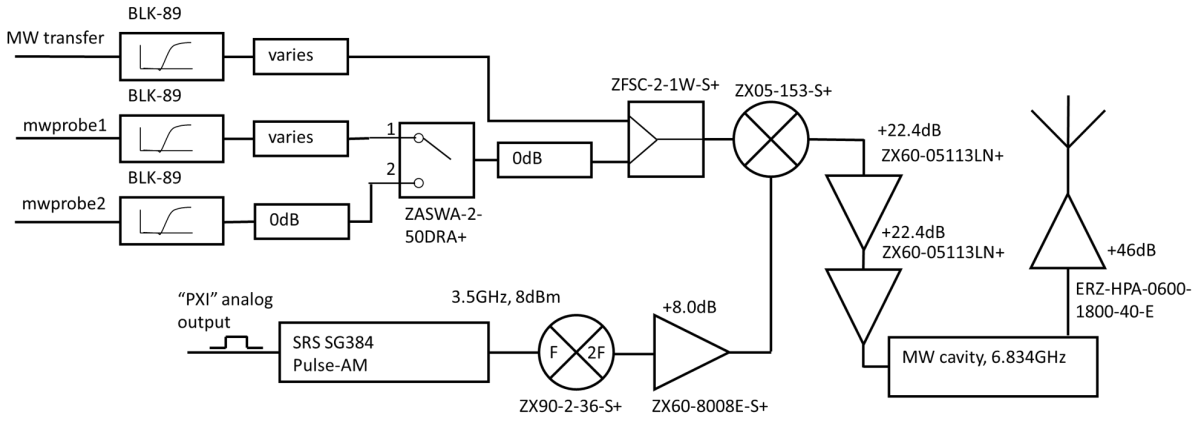

Figure 3.15: Microwave electronics setup diagram.

3.3 Vacuum Setup

3.3.1 Rate Table

The experiment is placed on top of a rotating platform, driven by a 2 kW electric motor, referenced to an optical encoder wheel with 1 arcsecond resolution, to provide a reliable way to measure rotation during the experiment and cancel out the phase accumulation of the Earth's rotation if needed. The platform seen in figure 3.16 is held in place by an air bearing to minimise vibrations caused by the motion of the platform. Additionally, a pressure sensor is installed to prevent motor drive from engaging if the air bearing pressure becomes too low.

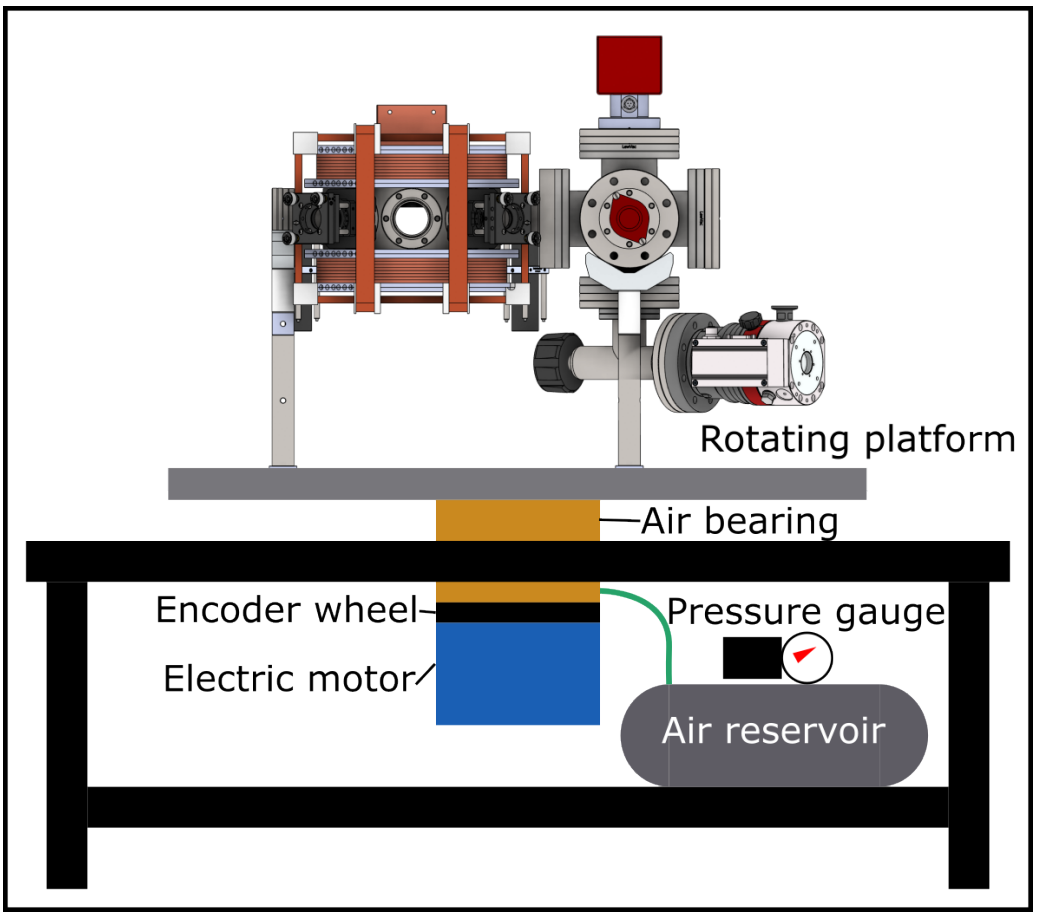

Figure 3.16: The rate table setup.

3.3.2 UHV Chamber

The experiment is carried out in a vacuum chamber with eight CF-60 side windows, a CF-160 bottom window, and a CF-160 wire feed-through at the top, allowing for 200 individual wire connections via four D-sub 50 connectors as seen in fugure 3.17. The internal volume of the system is approximately 20 litres. The NEXTorr D 200-5 combination pump, manufactured by SAES Getters, is used to maintain the pressure inside the chamber below 1×10^{-10}mBar. It is acting as an ion pump and an absorptive getter simultaneously. We cannot provide a good number for the vacuum quality because it exceeds the reading range of the pressure gauge.

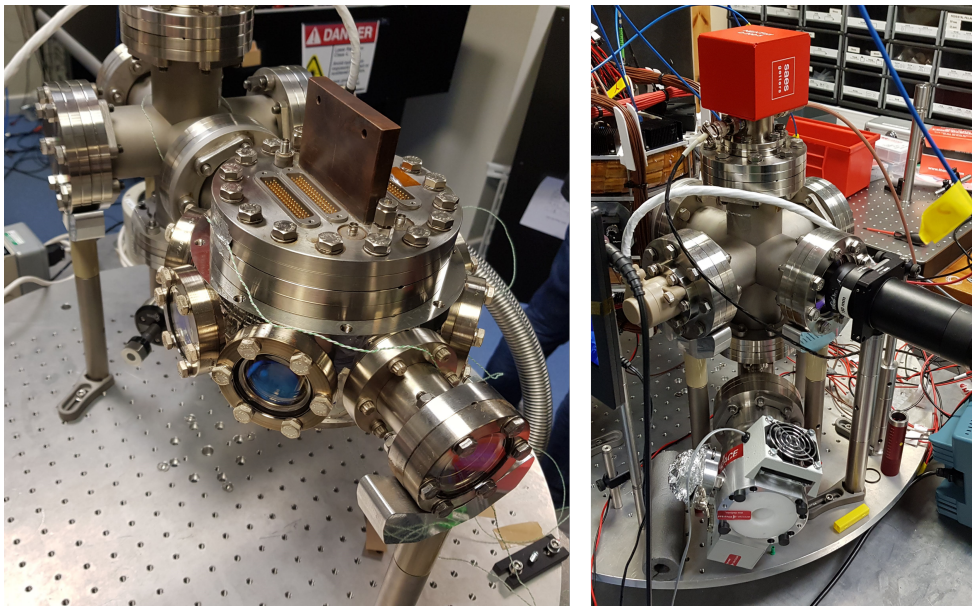

Figure 3.17: Pictures of the vacuum chamber.

Initially, a turbo pump is used to pull the vacuum, while a diaphragm pump provides the intermediate pressure needed for the turbo pump during the baking process. After the desired vacuum is achieved, the turbo pump is detached, and the chamber is sealed. The setup needs to be maintained at high temperature for more than a week to achieve high quality vacuum. The main reason for baking is to drive the moisture out of the bulk of the metal chamber. The baking temperature limit is set to 120°C by the glass transition temperature of PCB materials. The setup is wrapped with heater belts, insulated with aluminium foil, like shown in figure 3.18, and equipped with four temperature probes to

monitor temperature on the exterior surface. We have individual control over each heating belt, which makes it easier to prevent temperature gradients. Temperature differential can cause uneven thermal expansion of materials, introducing strain across glass windows and other components which leads to cracks and mechanical damage to the chamber.

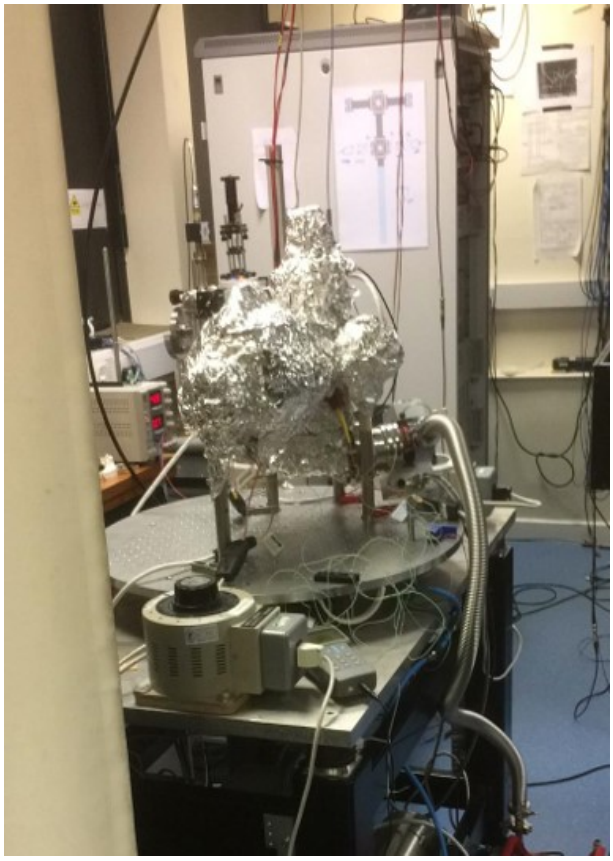

Figure 3.18: Vacuum chamber prepared for the baking process.

The bakeout procedure follows the steps outlined below. Figure 3.19 provides key measurements of vacuum chamber temperature and internal pressure during this procedure.

- Once the apparatus is put together, the valve that links the vacuum chamber and the turbo pump is opened. The rough vacuum can be achieved by the backing pump in approximately one hour without having to switch on the turbo pump.

- After a rough vacuum is established, the turbo pump is turned on. Initially, the turbo pump drive motor draws more current due to the viscosity of the air at high pressures. It can take a few hours for the pressure to drop to the point where the current from the drive motor decreases and the turbo pump is at full speed.

- The hot-filament ionisation gauge is switched on to measure the vacuum pressure. Turning the pressure gauge on at high gas pressure would lead to catastrophic failure of the device.

- The heating belts begin to raise the temperature of the chamber. The temperature of the vacuum chamber increases slowly over several days, never exceeding the maximum temperature change rate of 1°C/h. The final temperature during the baking period is 120°C.

- The following days are spent with the temperature kept at its highest until the readings on the pressure gauge decrease and remain steady. Afterward, an electric current is passed through a Rubidium dispenser to break the seal, resulting in a short-term surge in pressure.

- Temporarily heating the non-evaporable getter material causes some of the gasses to be released and pumped away by the turbo pump. The remaining gasses diffuse into the material, creating a reactive surface that can capture any gas molecules in the vacuum chamber. This conditioning procedure takes 24 hours and causes the second temporary spike in pressure.

- The temperature inside the vacuum chamber is then gradually lowered until we reach the operating temperature of the ion pump. The ion pump element is turned on and then off again before the NEG element is put in activation mode for another hour.

- The ion pump is turned on for another 15 minutes. This pulsing of the ion pump is done to ensure that there are no gasses embedded within the structure of the pump.

- The vacuum chamber is finally sealed from the turbo pump, and the temperature of the entire setup is slowly brought to room temperature over the period of 24 hours. The safest way to disconnect the turbo pump is to reduce its speed before turning off the diaphragm pump. This prevents the turbo pump from being exposed to atmospheric pressure while its rotor blades are still in motion.

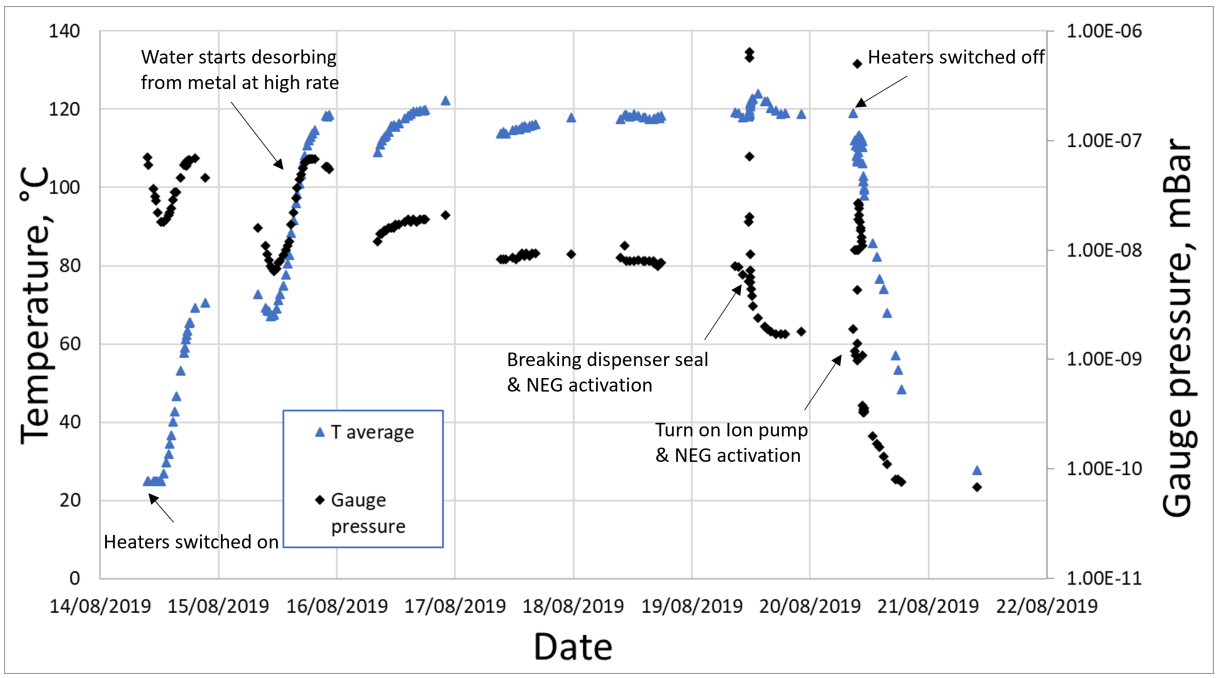

Figure 3.19: Temperature and pressure change during the bakeout process.

All materials inside the chamber have been tested to ensure that they are suitable for UHV conditions. The 12-layer PCB and the UHV compatible antenna were of particular concern; however, the final vacuum achieved is below 1×10^{-10}mBar. The PCB materials, adhesives, and thermal interface compounds have been certified by ATSM E595 for use by NASA.

A copper piece called the cold finger is placed in the middle of the feedthrough flange at the top of the vacuum chamber. Its purpose is to mount the PCB and to take away the heat generated in the wires trough ohmic losses. The thermal interface between the PCB and the cold finger is a silver-filled paste from the Kurt J. Lesker company, and the PCB material of choice is manufactured by Rogers Corporation. The circuit board is made of RO4350B laminate with 2 oz. copper cladding, separated by RO4450F prepreg. The RF chip is bonded on top of the PCB using a UHV compatible adhesive, and the chip itself contains only non-outgassing materials, such as silicon, evaporated gold pads, electroplated copper traces, and a silicon dioxide insulation layer. The atom chip at the top of the stack contains materials similar to those of the RF chip; however, a distinct difference between the two chips is the two-layer evaporated gold structure on top of the atom chip. The first gold layer is evaporated onto the silicon substrate, which is then

covered in 5 microns of SU-8 polymer, known for its hardness, UHV compatibility, and flat surface finish.

Electrical connections between different layers of the PCB structure seen in figure 3.20 are made by either gold wire ball bonding or silver-filled conductive epoxy where the ball bonding process poses a high risk of damaging the chip. The layer at highest risk of damage during the ball bonding process is the top layer of the atom chip. The reason for the increased risk is the fact that the upper gold layer of the atom chip rests on top of the SU-8 polymer. When the ball bonder applies pressure required to cold-weld the gold wire to the atom chip pad, the polymer underneath fails and causes a failure known as "cratering". Due to the high failure risk, it was opted to make the top layer connections using silver-filled conductive epoxy, which was subsequently cured in an oven. An extensive overview of gold wire ball bonding can be found in [54].

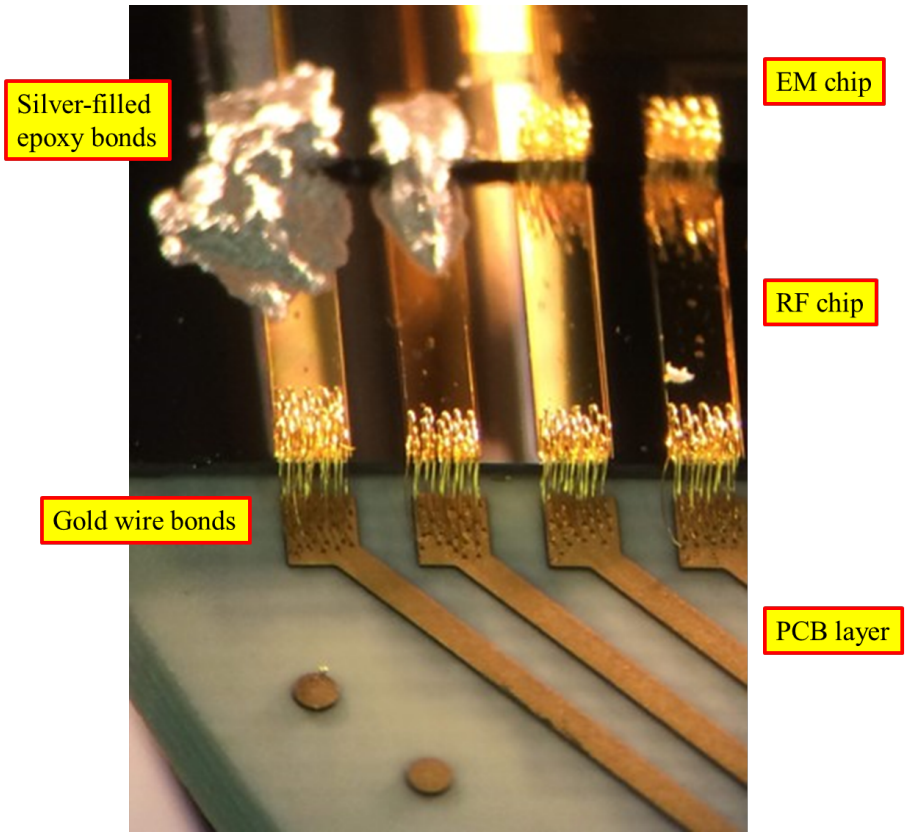

Figure 3.20: Atom chip bonding connections. The bonds in the top left corner of the picture were done using silver-filled epoxy rather than gold wire ball bonding technique. Epoxy bonding is only used for gold pads resting on top of SU-8 layer to prevent chip pad damage.

In addition to the existing conducting structures, a monopole MW antenna has been placed inside the vacuum. This antenna is composed of an SMA cable, made by LewVac, kapton-insulated copper wire, and a UV-curable adhesive, OP-67-LS, manufactured by Dymax. This adhesive has since been replaced by OP-81-LS, which offers better outgassing properties, but is more difficult to store. The UV curable adhesive is also used to attach a combination mirror and $\lambda/4$ waveplate, produced by LENS-Optics GmbH. The waveplate was placed on top of the PCB, and the glue was then applied in 4 locations around the optical component to secure it to the surface. This optical component is a part of magneto-optical trap setup and it facilitates cold atom cloud preparation away from the chip surface.

This experiment utilises a Rubidium metal dispenser as its atom source. The dispenser contains isotopes with concentrations that match their natural abundance, meaning that the atomic vapour is composed of 72.2% ^{85}Rb and 27.8% ^{87}Rb. The dispenser is manufactured by SAES Getters and is placed in a ceramic holder to protect other components of the setup from thermal damage.

3.4 Optical Setup

3.4.1 Laser Locking, Tuning and Beam Shaping

The optical bench contains beams from 3 laser systems. Two commercially available systems, TA Pro and DL Pro, are made by Toptica, and a compact laser for experiments in matter wave interferometry (CLEMI), is developed by C. Rammeloo at University of Birmingham. The CLEMI system is housed in a 19-inch rack from which an optical fibre delivers light to the optical bench. The lasers emit light at four distinct frequencies around the D_2 transition line (780nm), each with its own purpose. The laser locking scheme is displayed in figure 3.22 and the diagram of the laser setup is provided in figure 3.21. An additional laser table is dedicated to a tunable, high-power Titanium-Sapphire laser with a set wavelength of 760 nm to serve as a 'plug' for the optically plugged quadrupole trap (OPQT) setup described in chapter 4. The laser light is transferred from the optical benches to the experimental setup via polarisation maintaining single-mode optical fibres. About $1W$ of the power is delivered into the vacuum chamber.

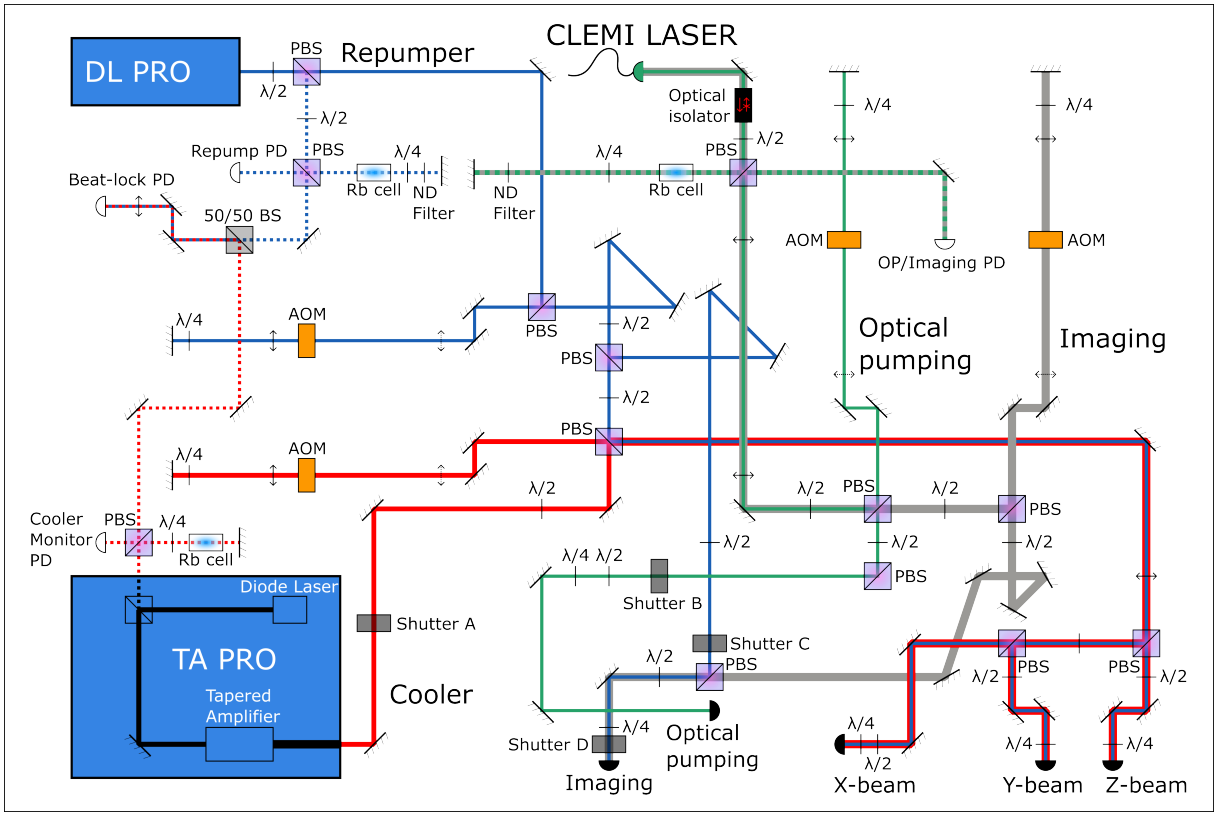

Figure 3.21: Schematic diagram of the optical bench setup.

The DL Pro and CLEMI lasers are locked to ^{87}Rb reference using Doppler-free saturated absorption spectroscopy (SAS) [55], and the TA Pro is phase-locked to the DL Pro using the electronics described in [56]. The counterpropagating pump and probe beams in a vapour cell eliminate the broadening effects due to thermal motion of atoms within a vapour cell and provide a stable frequency reference for laser locking. The error signal required for frequency stabilisation is derived by modulating the laser diode current at high frequency, typically over 100 kHz, which is later demodulated and passed through low-pass filter and into a proportional-integral feedback control loop for the laser. More details on the derivation of the error signal can be found in [57].

The CLEMI system provides laser fibre-coupled light output for imaging the atoms and the optical pumping procedure. It is capable of producing up to 400 mW of laser power at 780 nm, however, only about 80 mW of power is used for the experiment. The spectral feature used for laser locking is a crossover peak equidistant between the $F = 2 \leftrightarrow F' = 2$ and $F = 2 \leftrightarrow F' = 3$ transitions. In one path, an acousto-optical modulator (AOM) shifts the laser frequency up by 133MHz to match the resonance of $F = 2 \leftrightarrow F' = 3$ for imaging, and in the other path the frequency is adjusted by -133MHz to shift towards the $F = 2 \leftrightarrow F' = 2$ line. The laser beam in each path passes the AOM twice, therefore, doubling the frequency shift and the dynamic range of the device without steering the beam as the RF input frequency changes. The AOMs serve two roles in this setup: to adjust the laser frequency with high precision and to quickly and reliably switch the laser beams on/off. Even fast mechanical shutters take $1 - 10$ milliseconds to completely close, while an AOM is capable of shutting off the output of the beam within $< 100\mu$s.

The DL Pro system is an external cavity diode laser (ECDL) in Littrow configuration outputting a single-mode beam with 100 mW of power. This beam acts as a repumper which excites the atoms from $F = 1$ ground state to excited $F' = 2$ state and allows them to decay to the $F = 2$ manifold. The DL pro is locked to a $F = 1 \leftrightarrow F' = 1$ transition feature, whereas AOM increases the laser frequency by ≈ 157MHz to be on resonance with the $F = 1 \leftrightarrow F' = 2$ transition. The repumper beam passes the AOM twice, just like the imaging and the optical pumping beams.

The cooling laser light is provided by the TA Pro, which delivers 1.5 W of power at the output. It is a tapered amplifier system referenced by a master ECDL, similar in construction to the DL Pro system. The master laser has a fraction of its output used to phase-lock itself to the DL Pro. Both the TA Pro master and the DL Pro reference beams are spatially overlapped onto a fast photo diode using a 50/50 beamsplitter. The photodiode can detect the beat note between the two lasers, corresponding to the frequency difference of the two sources, but not the individual frequencies of the lasers. This photodiode signal is amplified and fed into a phase lock circuit [56] which allows us to dial in the required frequency difference between the stabilised DL Pro reference and the master laser of the TA pro in increments of 10 MHz. The cooler wavelength is set to be red-detuned from the $F = 2 \leftrightarrow F' = 3$ transition. This is achieved by setting the TA Pro master laser frequency to be shifted by 6.21 GHz from the $F = 1 \leftrightarrow F' = 2$ transition, which is actually blue-detuned from the $F = 2 \leftrightarrow F' = 3$ line, and then shifting the light frequency down using a double-pass AOM setup to achieve the desired detuning.

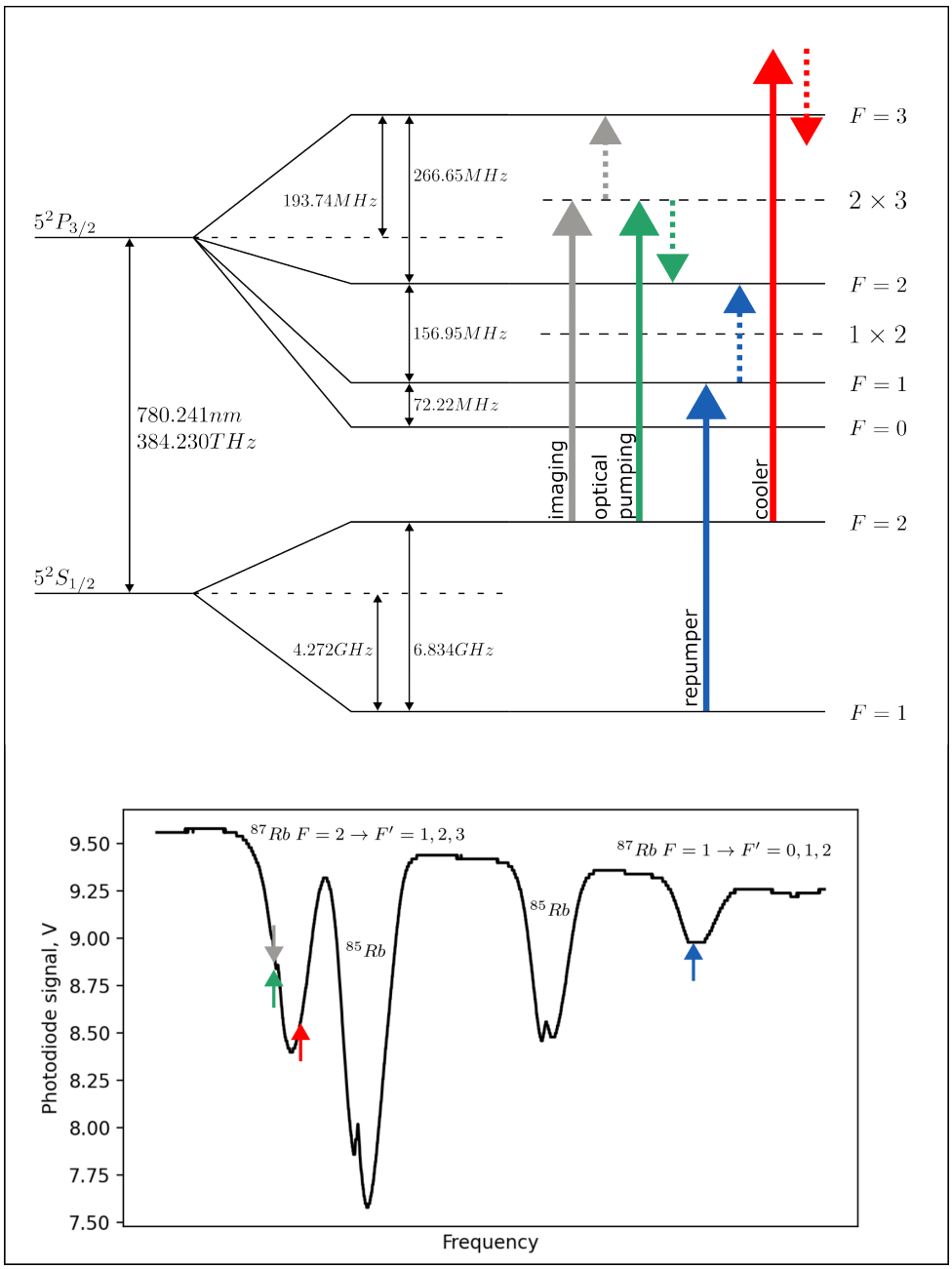

Figure 3.22: Laser locking frequency diagram (above) and typical spectroscopy signal used for laser locking (below). Arrows with dotted lines indicate AOM frequency shift.

3.4.2 On-Chamber Optics

The light delivered from the optical fibres is distributed among 6 fibre couplers affixed to the vacuum chamber with each beam direction displayed in figure 3.23. There are three retroreflected beams producing magneto-optical trap, imaging, and optical pumping beams, and the OPQT 'plug' beam.

The cooler beams in the x-y plane are 45 degrees from the y-axis and orthogonal to each other. The beams are first collimated and expanded to 25mm diameter, then, they pass through a polarising beamsplitter to clean the light polarisation before a quarter waveplate sets the appropriate circular polarisation required to produce the MOT. On the other side of the vacuum chamber there are adjustable mirrors which reflect the cooler light back. Another quarter-waveplate is placed between the mirror and the vacuum chamber in order to preserve the light-field helicity when the light propagation changes direction. The z-beam has the quarter-waveplate and mirror attached to the PCB inside the vacuum chamber instead of being positioned externally. Each cooler beam has around 30-50 mW of cooler power at the output and up to 10 mW of repumper light coupled into the same fibres. The power balance between each cooler beam needs to be adjusted carefully to optimise the size of the MOT through the use of the half-waveplates on the optical bench. We did not observe the need to balance the power output of the repumper in each of the beams, as long as sufficient repumper intensity was present in combined output of the three fibres.

The 'plug' beam is directed in the y-direction through the centre of the magnetically captured atom cloud near the PCB surface. Since this beam requires submillimeter alignment precision, a pair of mirrors are used to direct and adjust the collimated beam path. A convex lens focusses the beam to a spot about 30μm in diameter at the location of the atoms. The 1 W of laser power is terminated at the beam dump on the opposite side of the vacuum chamber.

The optical pumping beam is expanded to 50mm diameter to uniformly illuminate the free-falling atomic cloud along the x-axis. A polarising beamsplitter is placed at the fibre output before the beam passes through a quarter-waveplate to set the correct pump

beam polarisation. Only < 10mW of laser power is needed to successfully pump the atoms into the $|F = 2, m_F = 2\rangle$ state. An imaging beam fibre can also be combined through a beamsplitter to investigate the atomic ensemble during the MOT loading, CMOT, optical pumping, and magnetic recapture stages.

Imaging of the atoms is done along the x-axis when we investigate the initial stages of atomic ensemble preparation; or along the y-axis during the remainder of the experimental stages, such as evaporative cooling, atom chip loading and guiding of atoms inside the chip-based trap. Imaging along the y-axis is done by reflecting the probe light from the atom chip surface before it is captured by the CCD camera. This allows us to observe the real atom image and the reflection at the same time. We can use the two images to locate the cloud position along the y-axis as well as the distance from the chip. A narrow-band optical filter is placed in front of the CCD camera to prevent any light from the optical 'plug' beam from being scattered onto the sensor.

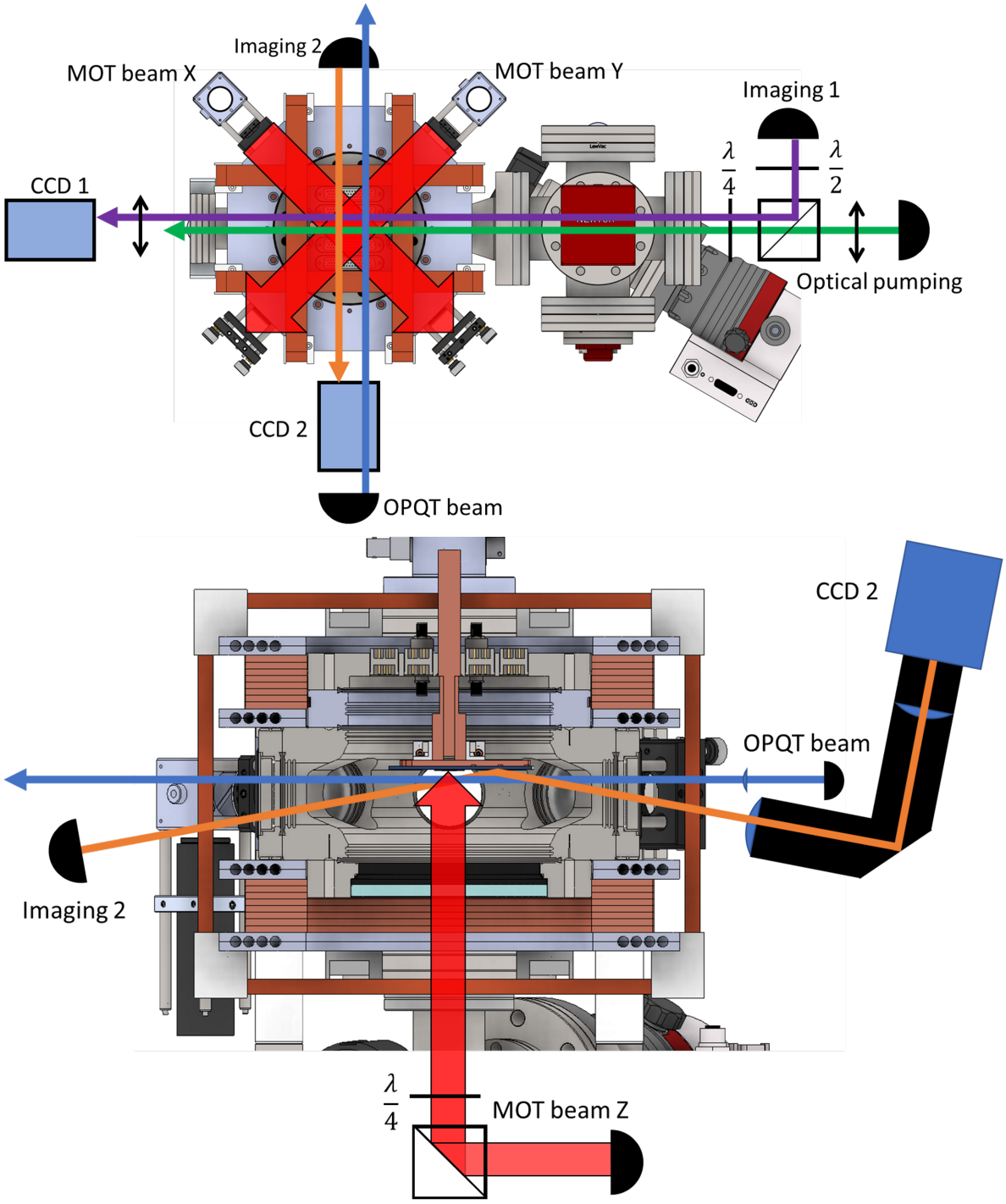

Figure 3.23: Vacuum chamber optical setup

3.5 Absorption Imaging

The analysis of ultra-cold atom clouds is usually based on absorption imaging. To perform absorption imaging, a wide-diameter laser beam illuminates a triggerable CCD camera after passing through the atomic cloud. For a resonant beam, some of the light is absorbed by the atoms, such that the cloud casts a shadow. We take three images to estimate the optical density of the cloud; see Fig. 3.24. The first image (atoms) is taken in the presence of atoms, the second image (light) is taken without atoms to reference the light distribution, and a third image (dark) is taken to measure any background illumination. The atomic density distribution can then be estimated independent of ambient lighting conditions and local intensity variations due to the beam profile and optical interference patterns. The atomic column density follows from Lambert-Beer's law and the light intensity on the CCD camera, I_0, is obtained as

$$I\left(x,y\right) = I_0 e^{-OD(x,y)} \tag{3.1}$$

with the optical density (OD) of the cloud obtained from intensity profiles of the three images taken during the experiment.

$$OD\left(x,y\right) \propto \frac{\log(I_{atoms}\left(x,y\right)) - \log(I_{dark}\left(x,y\right))}{\log(I_{light}\left(x,y\right)) - \log(I_{dark}\left(x,y\right))} \tag{3.2}$$

The atom number of the cloud in the shot can be calculated by summing over the pixel values and multiplying the result by a constant as described in [58]. Atom number is given by

$$N_{atoms} = \frac{x_{px}^2}{M_{optical}^2 \sigma_0} \sum_{x,y} OD\left(x,y\right), \tag{3.3}$$

where x_{px} is the size of the pixels, $M_{optical}$ is the magnification of the optical system, and σ_0 is the on-resonance cross sectional area of an atom that can be found in publication by D. Steck [2].

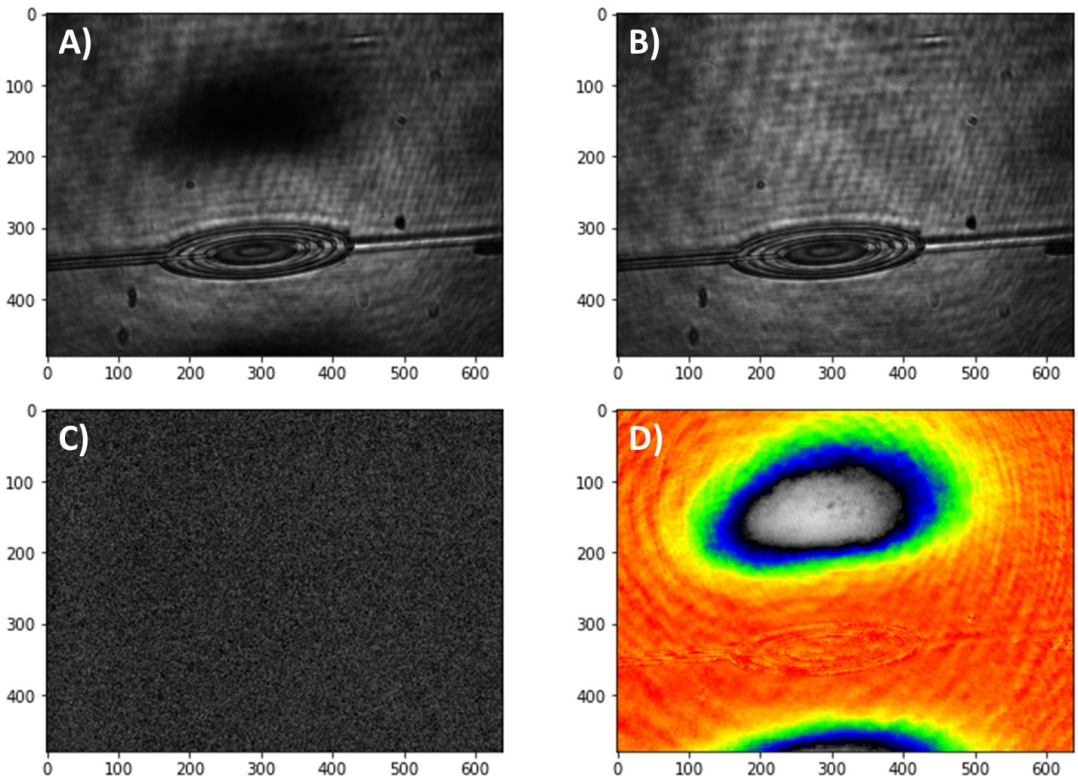

Figure 3.24: Measuring the optical density of the atom cloud (the units on the figures are in pixels). Three images are obtained: a) with a shadow cast by atoms, b) light field distribution c) background illumination. Part d) shows the processed image where brighter regions correspond to higher optical density.

Noise in the images due to camera shaking between the atom cloud, light and dark shots can cause inaccurate readings. To improve the signal to noise ratio, we exclude all parts of the image that only contain noise and no information about the atoms. We do this by manually selecting a region of interest within the image for each complete set of measurements. Subsequently, further data analysis can be implemented to reduce noise, and several noise reduction protocols have been investigated in Appendix A. This should in theory reduce the experimental time since fewer images are needed for averaging at the cost of greater initial time to obtain a good reference set.

3.5.1 Observing Atoms in $F = 1$ Manifold

We have set up a scheme outlined in figure 3.25 to observe the atoms in the $F = 1$ states without having to change the imaging setup too much. In order to do this we have coupled some of the repumper beam light into the same optical fibre as the imaging beam. To see the $F = 1$ atom manifold we first apply the imaging beam pulse that removes any remaining atoms in the $F = 2$ states that could affect our measurements, followed by a repumper pulse that brings the atoms from the $F = 1$ manifold to the $F = 2$ states. After the atoms are transferred from the state $F = 1$ to the state $F = 2$, we can proceed with the imaging of the atoms. This has proven to be a reliable way of imaging the atoms in $F = 1$ ground state; however, the atom number in this case is likely to be reduced since the atoms can decay into non-trappable states after the repumper pulse and leave the trap before being exposed to imaging light.

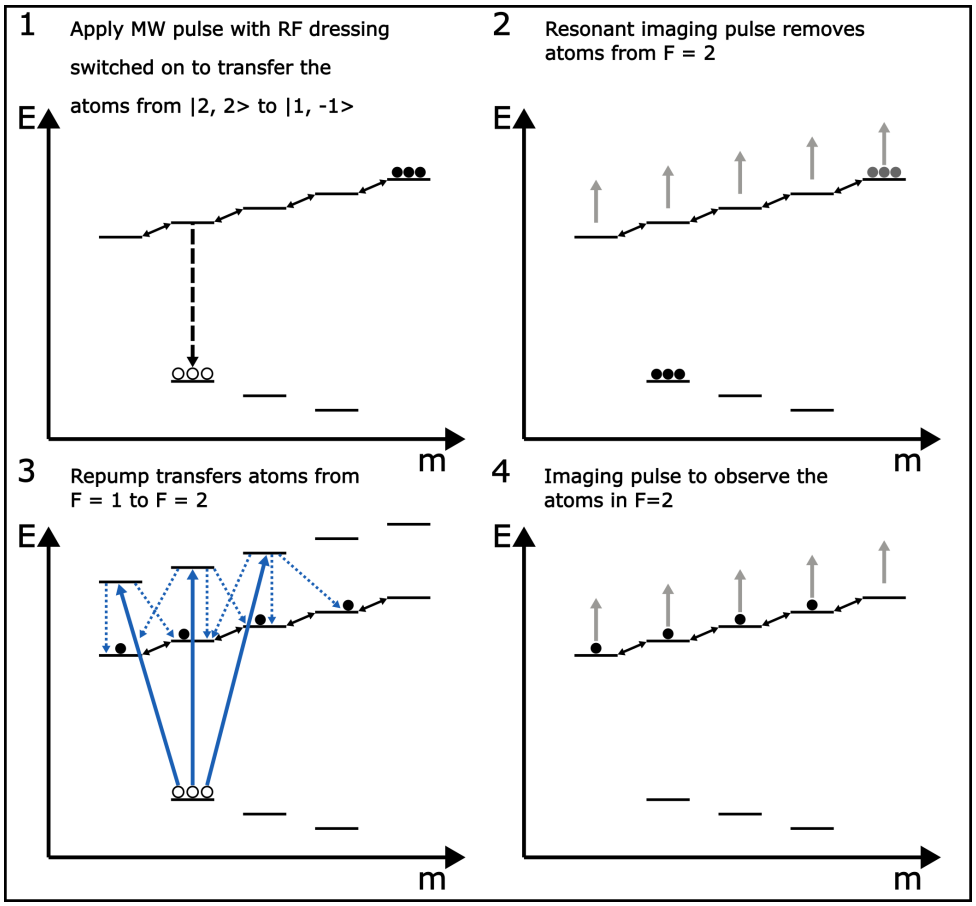

Figure 3.25: Atom imaging sequence in $F = 1$ ground state manifold. The Repump employs $F = 1 \leftrightarrow F' = 2$ transition and the Imaging beam is locked to $F = 2 \leftrightarrow F' = 3$ transiton.

Chapter 4

Experimental Results

At the beginning of the experiment $\approx 10^8$ ^{87}Rb atoms are loaded inside the magneto-optical trap (MOT) with temperature of around 1 mK. At the end of our measurement, we are only left with $\approx 10^4$ atoms inside the atom chip trap at $1\,\mu$K to complete the interferometric measurement. In this chapter, we will talk about how the experiment is run, how to characterise the setup, and how our observations inform us about the choice of experimental parameters.

4.1 Experimental Sequence

Typical sequence takes around 23 s. Most of the time is spent loading the MOT (10 s), then the atoms are transported toward the PCB (1.8 s), evaporatively cooled in the optically plugged quadrupole trap (5 s) and in the Ioffe-Pritchard type trap created by the atom chip (2.6 s). At the end of the sequence, additional waiting periods are added to ensure that the background gas pressure and setup temperature remain consistent during each run. The key parts of the experiment are provided in Figure 4.1. This chapter will focus on preparing the atoms and loading them onto the chip.

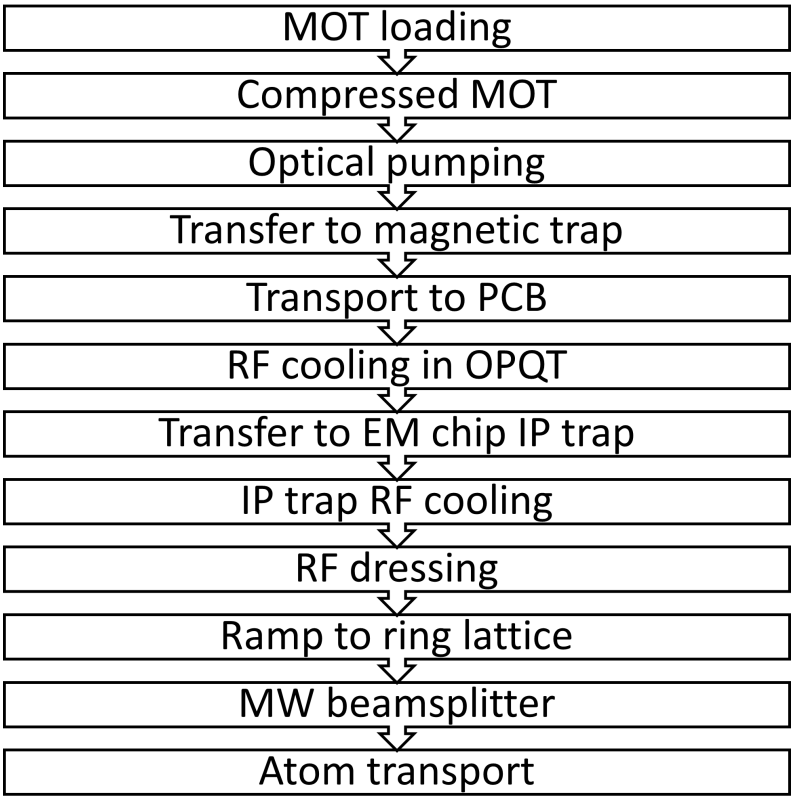

Figure 4.1: Key experimental sequence stages.

4.2 Initial Cooling

Almost every cold-atom experiment begins with a MOT. First introduced in 1987 [59], MOTs became one of the most important tools in the field of cold atom research. S. Chu, C. Cohen-Tannoudji and W. D. Phillips were jointly awarded a Nobel prize in 1997 for development of techniques used for atom trapping and cooling [60].

Our implementation of such a trap is a standard six-beam MOT that loads 6×10^8 atoms over the course of 10 s. The laser light produces a velocity-dependent force that reduces the temperature of the atom cloud and two external coils in anti-Helmholz configuration produce the magnetic field gradient leading to a position-dependent scattering force. The derivations of the equations in this section pertaining to atom trapping and cooling follow atom physics textbook authored by Foot [39].

4.2.1 Optical Molasses

The fundamental idea behind laser cooling relies on the Doppler effect causing atoms to experience a velocity-dependent force. Atoms will be moving around the vacuum chamber in all directions, however, the atoms moving towards the light source will see the light frequency increase, and the atoms moving away from the source will experience red-shifted light. The light shift, $\Delta\omega$, can be written as

$$\Delta\omega = \frac{v_{atom}}{c}\omega_L. \tag{4.1}$$

Here, v_{atom} is the velocity of an atom, c is the speed of light, and ω_L is the angular frequency of light. For the purposes of laser cooling, we can simplify the model of our atom to a two-level system with a ground and excited states, represented as $|g\rangle$ and $|e\rangle$ respectively. A red-detuned laser beam will only bridge the gap between the two energy levels when detuning is close to the Doppler shift. This causes a net force pointing along the light propagation direction when the atom's velocity component against light propagation is large enough. The net force due to photon emission vanishes because the spontaneous emission occurs in all directions at an equal rate, $\gamma_{scattering}$.

$$\gamma_{scattering} = \frac{\gamma}{2}\frac{I/I_0}{1 + I/I_0 + (\delta_\pm/\gamma)^2}, \tag{4.2}$$

where angular detuning $\delta_\pm = \omega_{light} \pm \Delta\omega - \omega_{transition}$, γ is the natural transition linewidth of the D_2 line, I is the intensity of the laser light, and $I_0 = \pi hc\gamma/3\lambda^3$ is the saturation intensity with σ_0 being the on-resonance scattering cross-section of the atom. In our case $I_0 \approx 16.7\,\mathrm{W/m^2}$ [2]. These absorption and spontaneous emission events lead to a force, F_L, defined by an angular wave vector of light, k_L;

$$F_L = \hbar k_L \gamma_{scattering}. \tag{4.3}$$

Now we introduce two counter-propagating beams to obtain the final expression for Doppler cooling force

$$\begin{aligned} F_{molasses} &= F_L(\delta_-) - F_L(\delta_+) \\ &\approx -2\frac{\partial F_L}{\partial \omega_L} k_L v_{atom} \\ &= \alpha v_{atom}, \end{aligned} \tag{4.4}$$

where α has the form given below;

$$\alpha \approx -4\hbar k_L^2 \frac{I}{I_0}\frac{-2\delta/\gamma}{\left(1 + (2\delta/\gamma)^2\right)^2}. \tag{4.5}$$

Here, $\delta = |\delta_\pm|$ and we assume that $k_L << \gamma$. The steady-state temperature is estimated from

$$k_B T(\delta) = \frac{\hbar\gamma}{4}\frac{1 + (2\delta/\gamma)^2}{-2\delta/\gamma} \tag{4.6}$$

which has a minimum value when $\delta = \gamma/2$. The lowest temperature achievable through optical molasses, T_D, also known as Doppler cooling limit [61], has the form

$$T_D = T(\delta = \gamma/2) = \frac{\hbar\gamma}{2k_B}. \tag{4.7}$$

^{87}Rb has a transition linewidth of $\gamma = 2\pi \times 6.065\mathrm{MHz}$ [2] that results in $T_D \approx 145\mu\mathrm{K}$.

4.2.2 Magneto-Optical Trap

Optical molasses force, described in equation 4.4 only depends on velocity and not position within the trap. To maintain a high density of atoms in the trap, we utilise magnetically sensitive states to change δ. The 3D quadrupole field applied to the atoms will shift the energy levels according to equation 2.25 causing the atomic transition frequency to shift by amount βz.

$$\beta z = \frac{g_F m_F \mu_B}{\hbar} \frac{\partial B}{\partial z} z \tag{4.8}$$

To illustrate the working principle of this effect, we can define a fictitious system with $F = 0$ and $F = 1$ manifolds coupled by a red-detuned light field. A diagram of such a setup is provided in figure 4.2. The selection rules dictate that in the lab frame of reference the atoms resonate with σ_+-polarised light on one side and σ_--polarised light on the other. The light force affecting the atoms inside the magneto-optical trap can then be determined by considering the combined frequency shifts caused by the velocity-dependent Doppler effect and the position-dependent Zeeman effect.

$$\begin{aligned} F_{MOT} &= -2\frac{\partial F}{\partial \omega}\left(k_L v_{atom} + \beta z\right) \\ &= -\alpha v_{atom} - \frac{\alpha\beta}{k_L} z \end{aligned} \tag{4.9}$$

Atoms are decelerated and held in position because of the differential light pressure that is exerted on them.

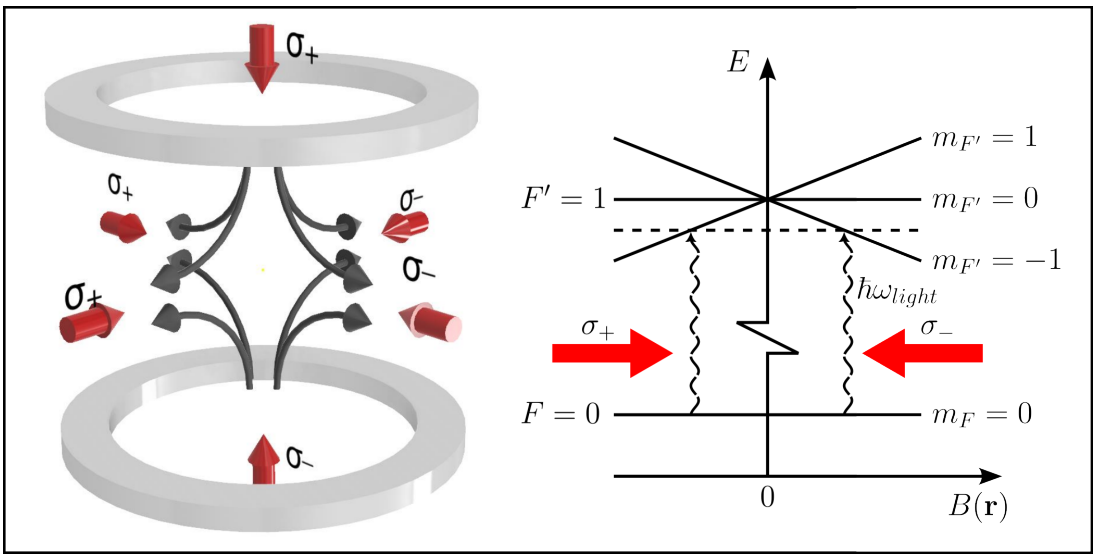

Figure 4.2: A diagram of a 3D MOT. The Zeeman effect, displayed on the right side, gives rise to position-dependent light force.

As time passes, the number of atoms within the trap will grow according to

$$N(t) = N_s\left(1 - e^{-t/\tau}\right). \tag{4.10}$$

The total number of steady-state atoms, N_s, is determined by a relatively simple equation [62].

$$N_s = \frac{V^{2/3}}{\sqrt{6}\sigma}\left(\frac{v_c^2}{M/2k_BT}\right)^2, \tag{4.11}$$

where V is the volume of the trap, v_c is the capture velocity of the atoms within the trap, M is the mass of the atom, and σ is the collisional cross section of the atom. This equation indicates that the final number of atoms in a MOT is directly proportional to how large the MOT beams are. Additionally, increasing the capture velocity, v_c, can dramatically improve our final atom number. It has been shown in [63] that the capture velocity is related to the trap depth by equation 4.12.

$$v_c^2 = \frac{2b^2U_{trap}}{M}, \tag{4.12}$$

where U_{trap} is the depth of the trapping potential, and the experimental work by [63] has found that $b = 1.29 \pm 0.12$.

Experimentally, the MOT accumulates 6×10^8 atoms over a period of 10 seconds; however, as seen in figure 4.3, the number of atoms during the loading stage appears to decrease towards the end. This is due to the reduced background gas pressure, since the ^{87}Rb dispensers are only briefly pulsed with higher current ($\approx$ 7A) at the beginning of the sequence. For the remainder of the experiment, the dispenser runs at low current ($<$ 3A) to keep the dispenser temperature high without increasing the pressure too much.

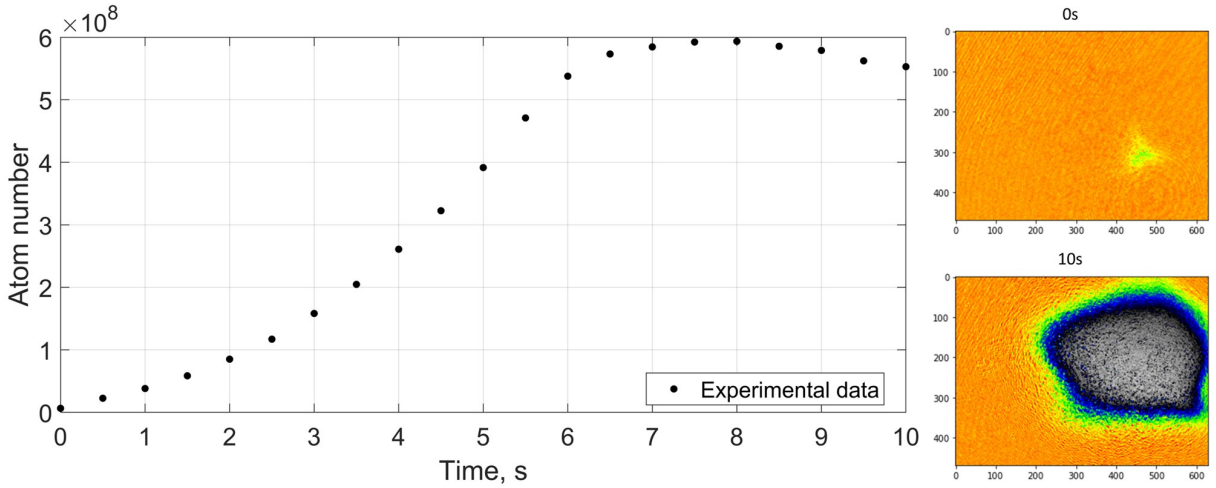

Figure 4.3: Atom number vs. time during the MOT loading stage. False-colour absorption images of the atom cloud are show on the right: top picture shows the optical density map of the atomic ensemble at t = 0 s and the bottom picture displays the image of the atom cloud at the end of the loading scheme with t = 10 s.

Figure 4.4 shows how the temperature of the MOT can be estimated by switching the MOT coils and allowing the thermal cloud to undergo ballistic expansion. The time evolution of the cross-sectional size of the atom cloud, $\sigma_{cloud}(t)$, with temperature, T, follows the equation below [64].

$$\sigma_{cloud}(t) = \sqrt{\sigma^2_{cloud}(t=0) + \frac{k_b T t^2}{M}}. \tag{4.13}$$

The camera's field of view is exceeded by the atom cloud in 6 miliseconds, thus restricting the time available for temperature measurement. The fitting process yielded a temperature of $T = 1.2 \pm 0.3$mK, which is not in agreement with the limit temperature value expressed in Equation 4.7. This higher-than-expected temperature is likely caused by the fact that the Cooler Laser detuning that maximises the atom number in the trap does not

lead to the minimum cloud temperature. Also, at low time values, a Gaussian fit is not a good measure of the atomic cloud size because the shape of the cloud is still deformed due to the non-uniform spatial intensity profile of light.

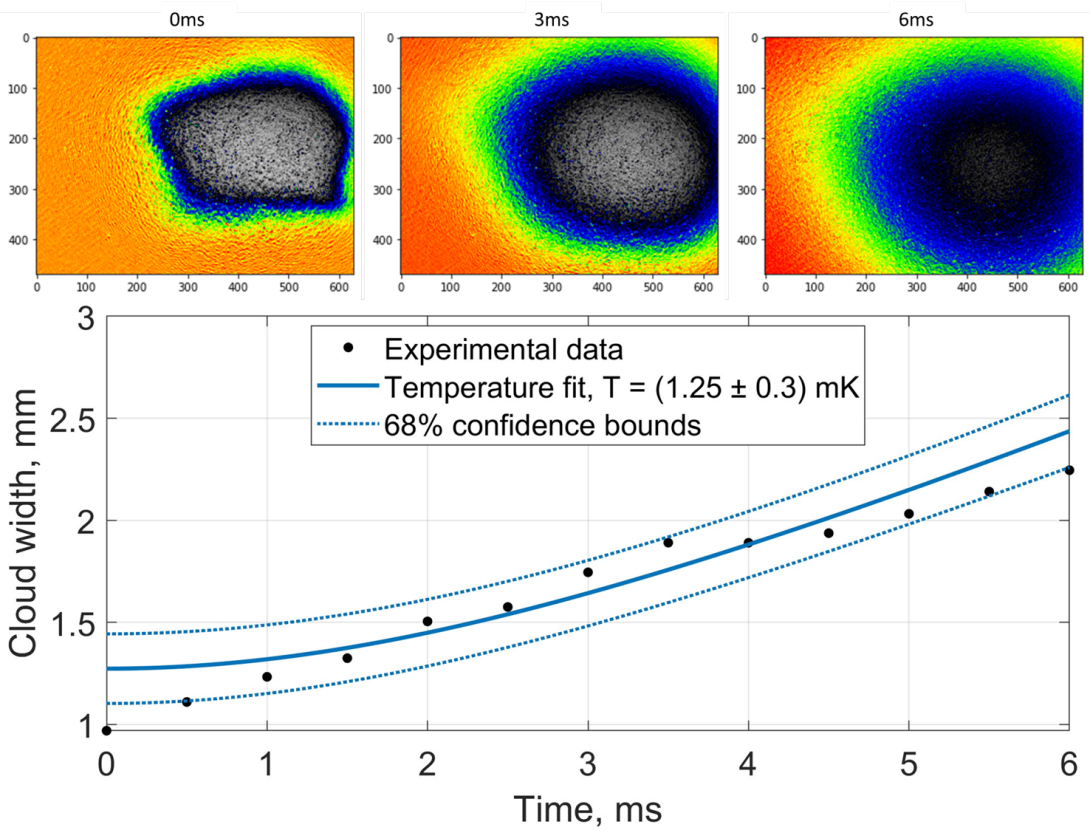

Figure 4.4: Ballistic expansion temperature measurement after MOT stage. The top row of images show the atomic ensemble expansion after 0, 3 and 6 ms.

4.3 Transfer Into Magnetic Trap

The cold atoms collected in our magneto-optical trap are further cooled and handed over to purely magnetic traps. Atom location, determined by the magnetic field minimum position, can be manipulated by applying additional fields created externally or by running currents in the local wire structures, enabling complex transport sequences. As soon as the MOT loading is complete, the MOT coils are switched off and a series of carefully timed pulses, frequency sweeps and magnetic field ramps are carried out to prepare the atoms in a pure, magnetically sensitive state. The main stages of this process involve polarisation gradient cooling, also known as the compressed MOT stage, optical pumping of the atoms into the $|F = 2, m_F = 2\rangle$ state, and switching on the magnetic fields to provide a trapping force that levitates the atoms inside the vacuum chamber.

4.3.1 Compressed MOT

The compressed MOT stage enhances the cooling capabilities of the magneto-optical trap by compressing the atom cloud and taking advantage of polarisation gradient cooling [65]. This technique allows us to achieve lower temperatures and higher phase-space densities, which are key to conducting our experiment. To do this, the magnetic field gradient confining the atoms is ramped down, and the atoms are allowed to freely expand in all directions while interacting with the light field.

As the atoms are falling under gravity, the detuning of the Cooler Beam is ramped away from the resonance frequency of the $F = 2 \leftrightarrow F' = 3$ transition. The fast-moving atoms have a different Doppler shift compared to atoms with zero velocity. We can scan the laser frequency to address all velocity groups to improve the cooling efficiency. The sweep time value is determined by looking at the number of photons required to stop an atom completely.

$$N_{photons} = \frac{v_{atoms}}{v_{recoil}}, \tag{4.14}$$

where $v_{recoil} = h/(\lambda M)$ is the recoil velocity of the atom. Atoms with temperature on the order of 1mK require around 100 photons to slow down. The atoms scatter photons at a maximum rate of $\gamma/2$ which gives a timescale for a frequency sweep duration

$$t_{sweep} = \frac{2N_{photons}}{\gamma}. \tag{4.15}$$

The minimum required sweep time for atoms at the temperature of 1 mK takes a few microseconds and is therefore mainly limited by the electronics that run the experiment. Once the ramps are complete, the polarisation gradient cooling stage takes place. The phenomenon was first discovered experimentally in 1988 [61], when lab demonstrations of laser cooling exceeded predictions set by the Doppler effect (a pleasant surprise). The theoretical explanation for polarisation gradient cooling was provided soon after in 1989 [66]. The polarisation gradient in question is formed when σ_+ and σ_--polarised light beams travel in counter-propagating directions. The superposition of these two beams

travelling along the z-axis creates a standing wave light field with a linear polarisation rotating in the x-y plane as we go along z. This spatial polarisation variation is presented in figure 4.5.

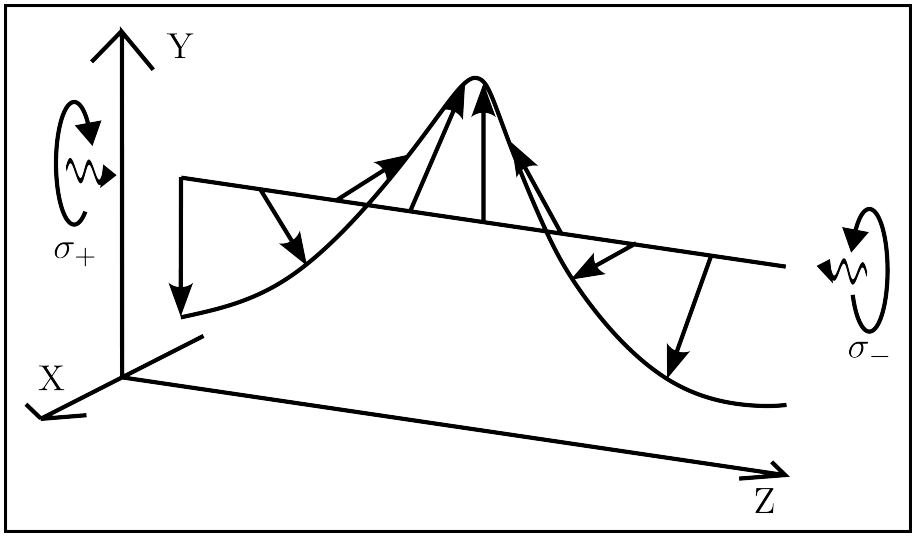

Figure 4.5: Rotation of light field polarisation in space.

As the atoms move along the z-axis with momentum kv_{atom}, the light polarisation perceived by the atoms changes. This could be described by applying a rotation operator which keeps the light polarisation constant, however, this will introduce energy shifts, caused by a fictitious magnetic field, which will manifest as a light pressure imbalance between σ_+ and σ_- fields. With red-detuned light, where $\delta = \omega_L - \omega_{transition} < 0$, and $v_{atoms} > 0$, the atoms will absorb more σ_- photons and the opposite will be true for the atoms with $v_{atom} < 0$. The magnitude of light intensity in this case determines the velocity capture range, the cooling force is independent of power, and the Doppler effect plays no role in cooling the atoms.

4.3.2 Optical Pumping

The purpose of optical pumping is to prepare the atoms in the most magnetically sensitive state $|F = 2, m_F = 2\rangle$. This state is chosen for multiple reasons. First, the magnetic fields generated by the coils can levitate the atoms with lower magnetic field gradients as discussed in the sections below. Second, the preparation of the atoms in the stretched state ensures the maximum compression required for efficient evaporative cooling. The atoms are optically pumped into the state $|F = 2, m_F = 2\rangle$ by applying a uniform bias field in the x-direction that sets the quatization axis for the atoms and shining a beam of light resonant with the transition $F = 2 \leftrightarrow F' = 2$. Depending on the light polarisation, the atoms can be pumped into one of the dark states set by the transition selection rules. The dark states, indicated by black circles in figure 4.6 ends up with the majority of the atom population, since there is no allowed transition that will pump the atoms out of those states. In the figure the transitions stimulated by the laser light are marked with solid arrows, and the spontaneous decay events are shown as grey arrows pointing down.

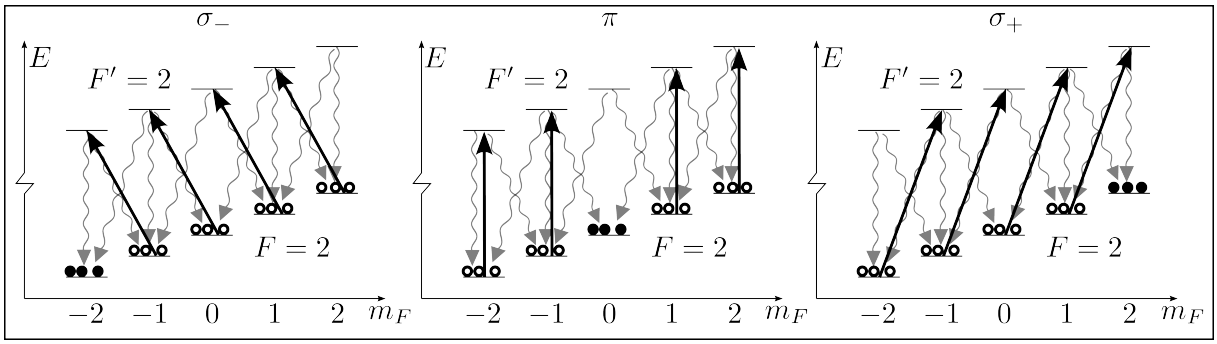

Figure 4.6: Optical pumping diagram with $\sigma_\pm, \pi$ pump polarisations.

4.3.3 Atom Capture

After the compressed MOT and optical pumping stages have been completed, the atoms are once again confined in space. However, this time, instead of light pressure exerting the majority force, it is the magnetic forces that confine the atoms inside the vacuum chamber. We use equation 2.25 to determine the minimum magnetic field gradient required to overcome the gravitational potential, $V_{grav} = Mgz$ pulling the atoms down.

$$\frac{\partial B_{DC}}{\partial z} = \frac{Mg}{\mu_B m_F g_F}, \tag{4.16}$$

where M is the mass of the atom isotope in question, and g is the gravitational acceleration constant. ^{87}Rb atoms require at least ≈ 16G/cm field gradient if they populate state $|F = 2, m_F = 2\rangle$, and ≈ 32G/cm if the atoms are in states $|F = 2, m_F = 1\rangle$ or $|F = 1, m_F = -1\rangle$. The magnetic field gradient is created by the MOT coils; however, because the atoms have fallen down during the previous stages of the experiment, the external magnetic fields need to be adjusted such that the magnetic field zero region still overlaps with now accelerated atomic ensemble.

After the atoms are recaptured in the magnetic trap, the temperature of the atoms can be measured to verify the success of the process. According to data in figure 4.7, the temperature at the end is reduced below the Doppler cooling limit, at $64 \pm 14\mu$K. Time-of-flight measurement has been used to determine the temperature of the cloud after letting it settle for 500 ms in the recaptured magnetic trap. During the ballistic expansion measurement, a non-zero magnetic field could distort the cloud expansion, giving a lower than expected temperature reading.

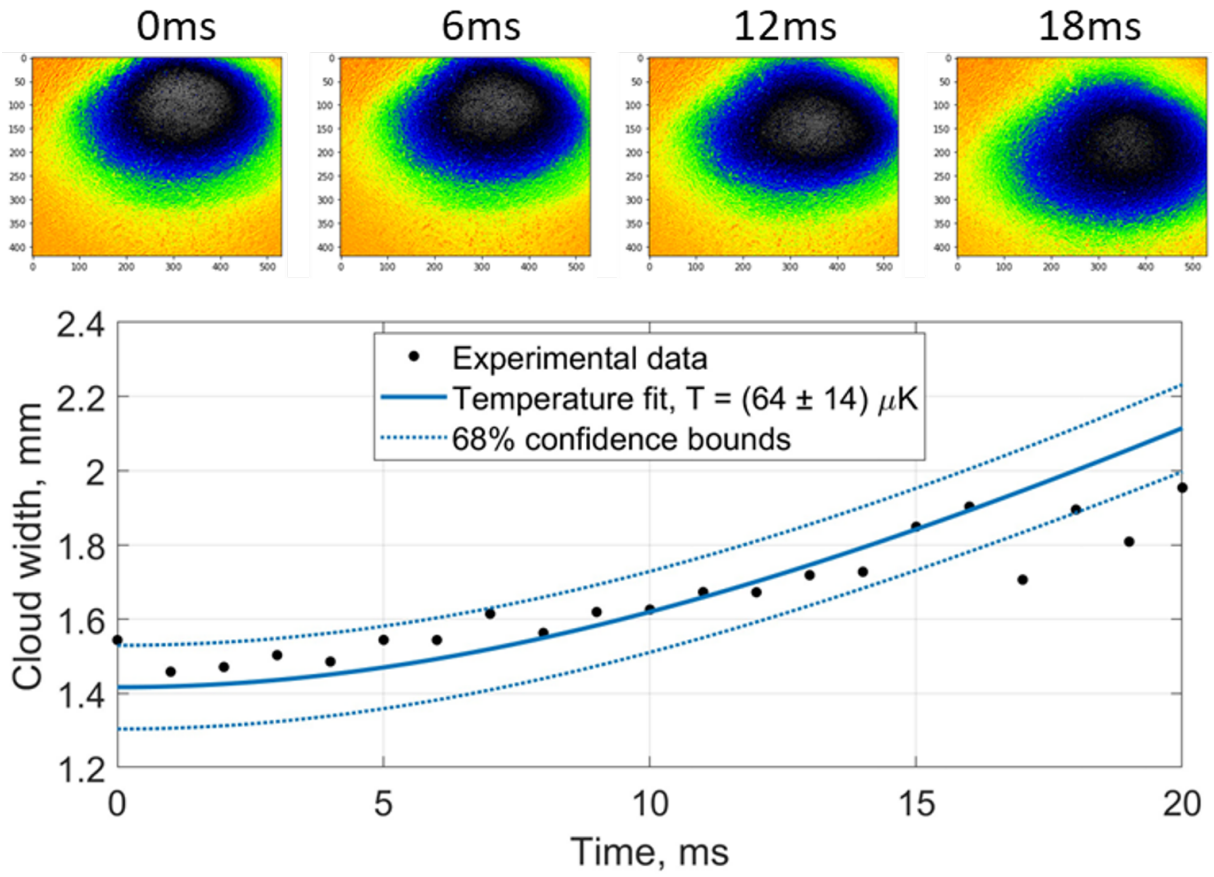

Figure 4.7: Temperature estimate from ballistic expansion after CMOT stage. The top row of images displays the atom cloud at different free-fall times during ballistic expansion.

We also employed in-situ RF thermometry, which does not necessitate switching of the magnetic trap. By introducing RF radiation a certain frequency, it is possible to selectively remove atoms at a fixed magnetic field intensity. At the resonance condition, where the frequency of the RF probe is equal to the Larmor frequency, the atomic spin is flipped and the atoms are released from the trap. This can be used to our benefit, as we can investigate the thermal distribution of the atoms one frequency at a time. By repeating the experiment multiple times with different ω_{probe} each time we can measure the fraction of atoms removed from the trap, which gives us an indication of the temperature of the atom cloud.

Depending on trap topology, the shape of the RF spectrum will look different. In our experiment we care about atoms either in a quadrupole trap, which has a linear potential gradient in all directions, or in an Ioffe-Pritchard type trap, which can be approximated as a harmonic potential. For a simple case of a quadrupole trap, we can write down a

potential equation.

$$E = m_F g_F \mu_B |\boldsymbol{B}| \tag{4.17}$$

The field magnitude B can be expressed by equation 4.18. There is a constant field gradient, q, in the x-y plane that is constant across the quadrupole trap. The factor of 2 in the z-direction gradient comes from the coil arrangement in the anti-Helmholz configuration.

$$|\boldsymbol{B}| = q\sqrt{x^2 + y^2 + (2z)^2} = qr \tag{4.18}$$

We also assume that the loss feature as a function of RF frequency will follow the normalised Boltzmann distribution, $N(r)$.

$$N(r) = NA4\pi r^2 e^{-E/k_B T} dr \tag{4.19}$$

The normalisation constant, A, should be set such that the integrated area under the distribution curve would give the total number of atoms, N. This equation subdivides the total number of atoms, N, to a number of thin equipotential shells with surface area $4\pi r^2$ and thickness dr. Each of these shells contains only atoms with energy E so the temperature T can be estimated. Probe frequency, f, is related to the equipotential radius, r through potential energy relation.

$$hf = m_F g_F \mu_B q r \tag{4.20}$$

From equations 4.20 and 4.19 we can derive the relationship between the RF probe frequency and the number of lost atoms.

$$dN(f) = NA4\pi \left(\frac{h}{m_F g_F \mu_B q}\right)^3 f^2 e^{-\frac{hf}{k_B T}} df \tag{4.21}$$

The temperature reading obtained by this method, as seen in figure 4.8, is $43.6 \pm 1.3\,\mu$K. The temperature readings obtained using these two methods were not in agreement with

each other, but both measurements were well below the Doppler cooling limit. The temperature reading obtained with RF spectroscopy is dependent on the power of the RF probe [1] and the transitions between the regimes where either the total energy or just the potential energy of the particle is measured, resulting in slightly different results [67].

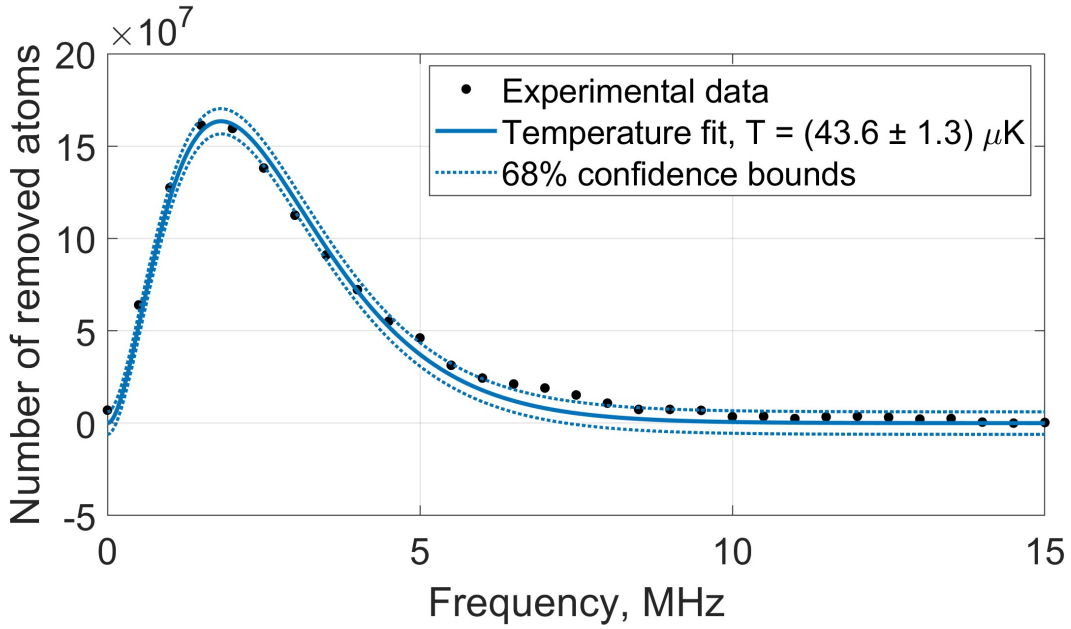

Figure 4.8: Temperature estimate from RF spectroscopy in a magnetic trap after the compressed MOT stage confirms that the atoms can be cooled down past $T_D \approx 145\,\mu$K with laser light. RF probe duration here is 550ms.

Similarly, the Ioffe-Pritchard trap has a harmonic potential that can be expressed in terms of the trap's curvature, c, and the position, r, which creates an isopotential surface.

$$E = m_F g_F \mu_B c r^2 \tag{4.22}$$

The thermal distribution for this trap is derived following the same steps as in 4.19. The scaling of this distribution with respect to the frequency of the RF probe is different. While the shape of this function represents the temperature of the cloud quite accurately, there is an additional frequency offset added by the presence of non-zero magnetic field

[1] The Rabi frequency at the atom chip trap driven by a coil of the same size and the same number of turns is 25kHz (from later data in the thesis). This was done with a 30W RF amplifier running at maximum power. The amplifier running the probe coil puts out 50mW of power (24.5x reduction in current) and the atom-coil distance between the measurement of the magnetic trap vs. measurement on the atom chip is doubled from 3cm to 6cm (another factor of 4.5 reduction in field magnitude). This leaves us with a Rabi frequency of 200Hz and the probing time is 550ms. Here, the more important issue to address would be the cloud rethermalizing during measurement rather than power broadening.

minimum at the bottom of the Ioffe-Prichard trap. The envelope of the spectrum needs to be shifted in frequency such that the beginning of the analytical solution matches with the potential minimum energy in the harmonic potential.

$$dN_{harmonic}(f) = NA2\pi \left(\frac{h}{m_F g_F \mu_B c}\right)^{3/2} \sqrt{f} e^{-\frac{hf}{k_B T}} df \tag{4.23}$$

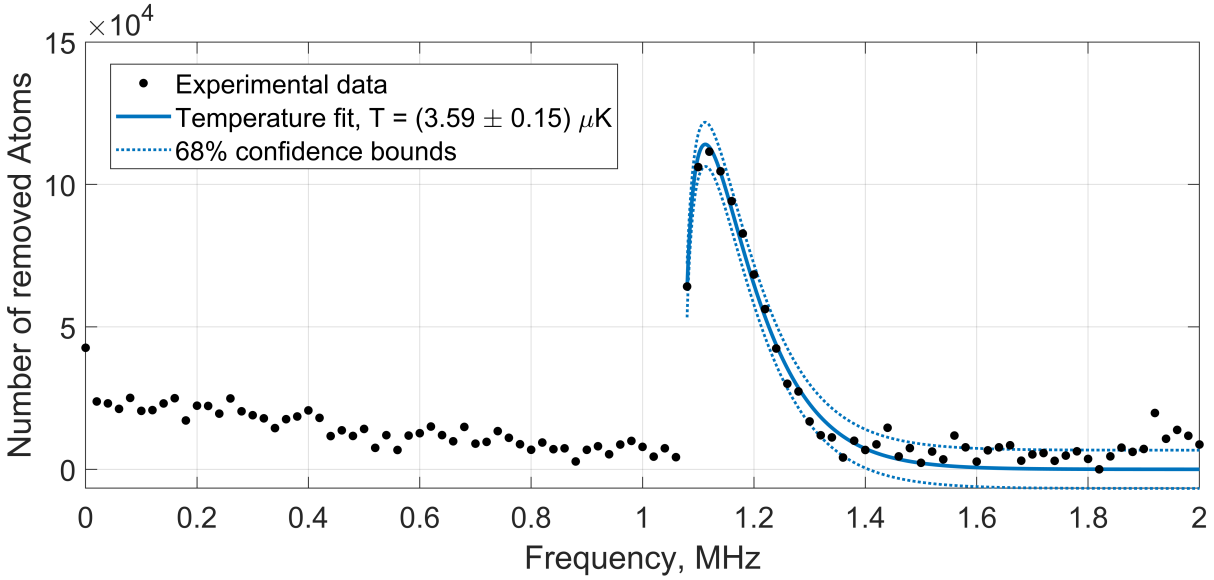

Figure 4.9: RF thermometry in an Ioffe-Pritchard type trap. The trap bottom corresponds to 1.06 MHz. The variations in atom number off-resonance can be attributed to background gas pressure variations over time.

4.4 Evaporative RF Cooling

During the magnetic transport stages of the sequence the atomic cloud temperature increases due to trap compression as well as non-adiabatic heating. Our goal is to reduce the cloud temperature to the point where it is just above the transition temperature for the formation of a Bose-Einstein condensate (BEC) [68]. Only at such ultra-low temperature we can expect to perform relevant measurements and attempt to load ring-shaped traps of the envisioned design. Low temperatures correspond to a longer de Broglie wavelength associated with the atom and, therefore, relieve the precision requirements needed to observe high-contrast interference fringes, however, achieving BEC may not be desirable due to increased collision losses. Our Sagnac interferometer requires atom clouds to pass each other at half-way point, so a lower number density is preferred at that stage of the experiment to prevent scattering losses. Figure 4.10 illustrates how evaporative RF cooling is used to achieve such temperatures. The applied RF is ramped down in frequency to remove atoms in a controlled manner starting with the highest potential energy and then moving down until only the lowest energy atoms are left. P. Valkering's thesis [69] is a useful resource for this part of the experiment. The efficiency of this process depends critically on the ratio of the collisional rethermalisation rate to the atom loss rate. If done efficiently, the lowered temperature of the cloud will raise the phase-space density (PSD), which is a good measure to describe the density of the atomic cloud, because it also takes into account the average distance between each particle. PSD is given by

$$\rho_{ps} = n\lambda_{dB}^3 = n\left(\frac{2\pi\hbar^2}{Mk_BT}\right)^{3/2}, \tag{4.24}$$

where n is the number of atoms per unit volume and $\lambda_{dB} = \sqrt{2\pi\hbar^2/Mk_BT}$ is the thermal de Broglie wavelength. A BEC is attained when the phase-space density exceeds 2.6. Intuitively, this means that a BEC is achieved when the average distance between atoms is comparable to the de Broglie wavelength. An important parameter in evaporative cooling is called the truncation parameter, η, which relates the average energy of an atom to the energy of an atom removed due to cooling processes, E_t.

$$\eta = \frac{E_t}{k_B T} \tag{4.25}$$

Provided that $\eta > 1$, the energy of the atom that is removed will be greater than the average energy of an atom in the ensemble, thus decreasing the total temperature of the cloud. To determine the energy of the atom that is removed, we use $E_t = \hbar\omega_{RF}$. The evaporative cooling process necessitates that the atom cloud re-thermalises before the RF frequency can be reduced again.

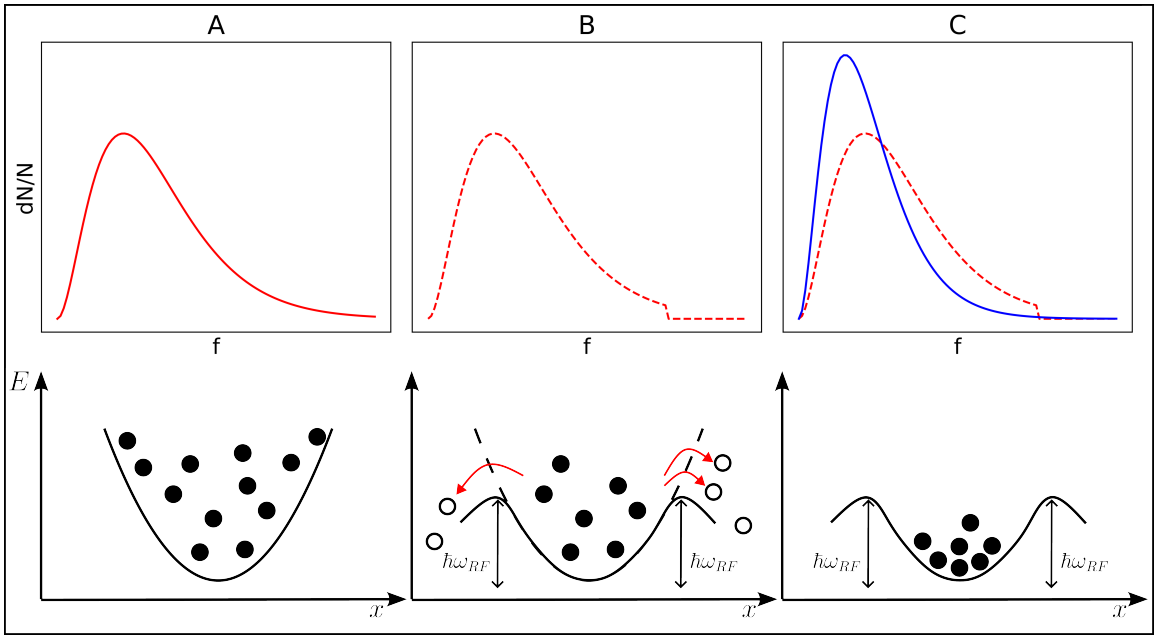

Figure 4.10: Evaporative cooling of an atomic ensemble. The top row shows the thermal distribution of the atomic ensemble as a function of frequency and the bottom row is a cartoon diagram representing atoms in a magnetic potential. In column A we have an initial thermal distribution of atoms. In column B the RF field couples the Zeeman sublevels of ^{87}Rb in a way that introduces a pathway for most energetic atoms to leave the trap, resulting in a truncated thermal distribution. In column C we can see the new steady state of the atom cloud with a reduced temperature. This process is repeated in discrete steps until desired temperature is achieved.

The duration of the rethermalisation process is equivalent to the time it takes for atoms to experience three collisions on average [70]. The average collision rate for each atom can be expressed as

$$\Gamma_{collision} = \langle v_{atom} \rangle \, \sigma \, \langle n \rangle \,, \tag{4.26}$$

where $\langle n \rangle$ is the atom number density, σ is the collisional cross section, and $\langle v_{atom} \rangle$ is the mean velocity of the atom. We can rewrite $\langle v_{atom} \rangle$ as

$$\langle v_{atom} \rangle = \sqrt{\frac{8k_B T}{\pi M}}, \tag{4.27}$$

where M is the mass of the atom. The elastic cross-sectional area of the ^{87}Rb atom in the $|F = 2, g_F = 2\rangle$ state is given by equation 4.28.

$$\sigma = 4\pi a^2 \tag{4.28}$$

Here, a takes the value found in [71].

$$a = 109 a_0, \tag{4.29}$$

where a_0 is the Bohr radius.

The final collision rate is then given by

$$\Gamma_{collision} = \sqrt{\frac{8k_B T}{\pi M}} 4\pi \left(109 a_0\right)^2 \frac{N_{atoms}}{V_{trap}}, \tag{4.30}$$

where V_{trap} is the volume of the trap. The cooling process can eventually enter a runaway regime, where the increased atom density raises the collision rate, allowing the time between cooling frequency steps to get shorter and shorter, until either we run out of atoms or a BEC forms.

The first cooling ramp shown in figure 4.11 occurs in an optically plugged quadrupole trap with frequency being ramped from 25MHz to $<$ 1MHz in 5 s. The trap temperature in the optically plugged quadrupole trap is reduced from 71μK to 21μK and the RF power is gradually reduced to prevent the atoms from entering the regime where the RF field dresses the atoms instead of kicking them out.

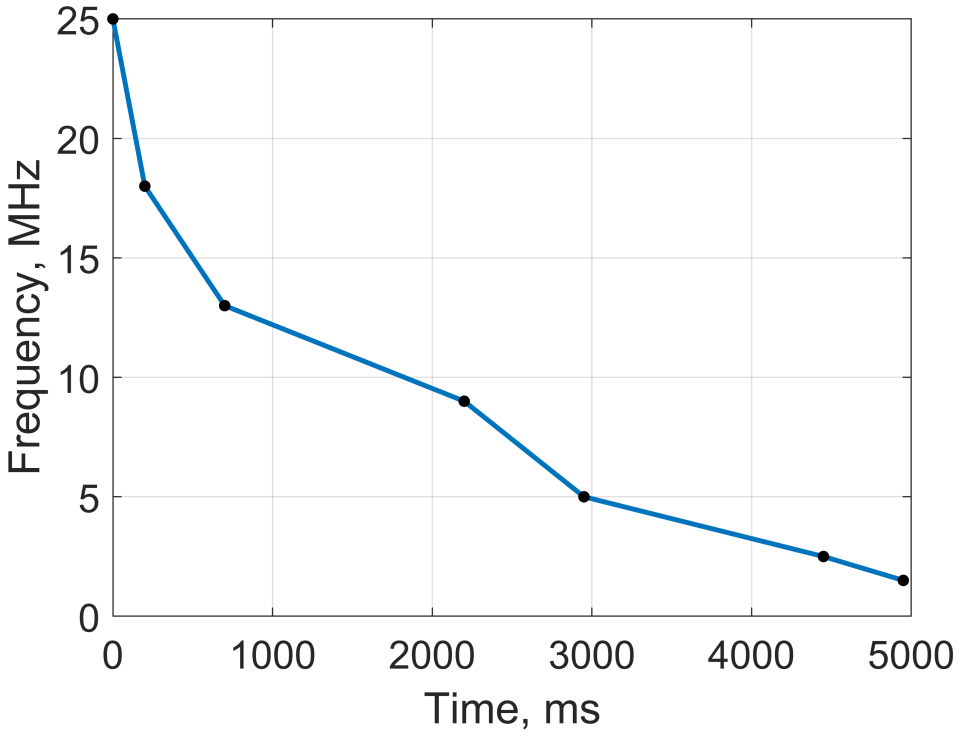

Figure 4.11: RF cooling ramp in optically plugged quadrupole trap.

4.5 Optically Plugged Quadrupole Trap

The challenge that we face is that colder atoms tend to accumulate closer and closer to the centre of the magnetic trap, where the magnetic field is minimal. For a quadrupolar trap, the minimum is at zero field where the hyperfine energy levels become degenerate and spontaneous Majorana spin flips lead to rapid atom loss. In order to go around this problem, we have multiple approaches that we can try; however, we found that using an optically plugged quadrupole trap [72, 73, 74, 75] works the best.

A more detailed derivation of the following results in this part can be found in [76]. The repulsive potential, U_{dipole}, produced by the blue-detuned light field with intensity profile, $I(\boldsymbol{r})$, is given by

$$U_{dipole}(\boldsymbol{r}) = -\frac{3\pi c^2}{2\omega_0^3}\left(\frac{\gamma}{\omega_0 - \omega_{light}} + \frac{\gamma}{\omega_0 + \omega_{light}}\right) I(\boldsymbol{r}), \tag{4.31}$$

and the scattering rate, Γ_{sc}, is expressed as

$$\Gamma_{sc}(\boldsymbol{r}) = -\frac{3\pi c^2}{2\hbar\omega_0^3}\left(\frac{\omega_{light}}{\omega_0}\right)^3\left(\frac{\gamma}{\omega_0 - \omega_{light}} + \frac{\gamma}{\omega_0 + \omega_{light}}\right)^2 I(\boldsymbol{r}), \tag{4.32}$$

where ω_0 is the angular frequency of the D_2 transition line, ω_{light} is the frequency of the applied field, and γ is the natural transition linewidth.

Several simplifications can be applied to the above equations by assuming that our light frequency is close to resonance. We can ignore the term containing $\omega_0 + \omega_{light}$ and we can also assume that $\omega_{light}/\omega_0 \approx 1$. This gives us simplified equations that depend only on detuning, $\Delta = \omega_{light} - \omega_0$

$$U_{dipole}(\boldsymbol{r}) = -\frac{3\pi c^2}{2\omega_0^3}\frac{\gamma}{\Delta} I(\boldsymbol{r}) \tag{4.33}$$

and

$$\Gamma_{sc}(\boldsymbol{r}) = -\frac{3\pi c^2}{2\hbar\omega_0^3}\left(\frac{\gamma}{\Delta}\right)^2 I(\boldsymbol{r}). \tag{4.34}$$

The Gaussian beam profile, $I(\boldsymbol{r})$, is defined by beam waist, $w(z)$, and output power, P.

$$I(z,r) = \frac{2P}{\pi w^2(z)} e^{-2\frac{r^2}{w^2(z)}}, \tag{4.35}$$

where $w(z)$ is the $1/e^2$ intensity beam radius at position z. Combining the quadrupole magnetic trapping field with the dipole beam pushing the atoms away from a zero-field region creates the trap shown in figure 4.12.

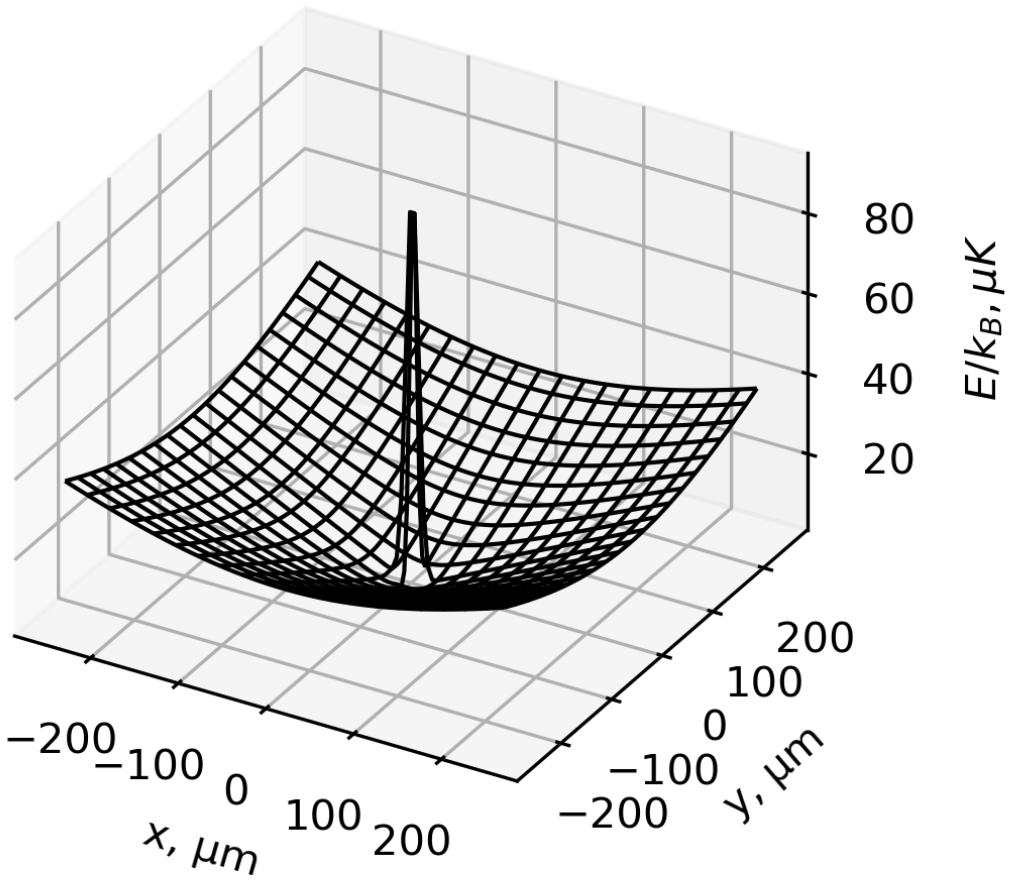

Figure 4.12: Optically plugged quadrupole trapping potential. In this particular case, the parameters are: $\partial B_{DC}/\partial r = 32G/cm$, $\lambda = 760nm$, $P = 1W$, $w(0) = 14\mu m$.

Because atoms are strongly expelled from the centre of the quadrupole potential, the atomic states always remain nondegenerate and thus Majorana losses are avoided. This technique allows us to evaporatively cool the atoms with greater efficiency, and this leads to an improved phase-space density at the end of the RF cooling ramp. The improvement is clearly visible at the end of the cooling ramp in figure 4.13.

The laser beam punching a hole in the atom cloud should ideally repel atoms without driving any transitions. Therefore, it is in our interest to maintain Γ_{sc} as low as possible while keeping the repulsive potential high enough to prevent atoms from entering a zero-field region. An important relationship to note is the one between the scattering rate and the dipole potential.

$$\hbar\Gamma_{sc} = \frac{\gamma}{\Delta} U_{dipole} \tag{4.36}$$

We can see that with increasing detuning the scattering rate decays faster than the trapping potential magnitude, however, we need a large beam intensity to maintain high potential barrier. While, in theory, a BEC can be achieved with as little as 70 mW of plug power [77], we maintain the intensity of the plug beam as high as practically possible to completely expel the atoms from a spatial region where the plug beam is focused. We found that even by reducing the plug beam power by 20% does not affect the atom number significantly compared to other sources of uncertainty, such as power fluctuations in Cooler Beam power, detuning, and background gas pressure.

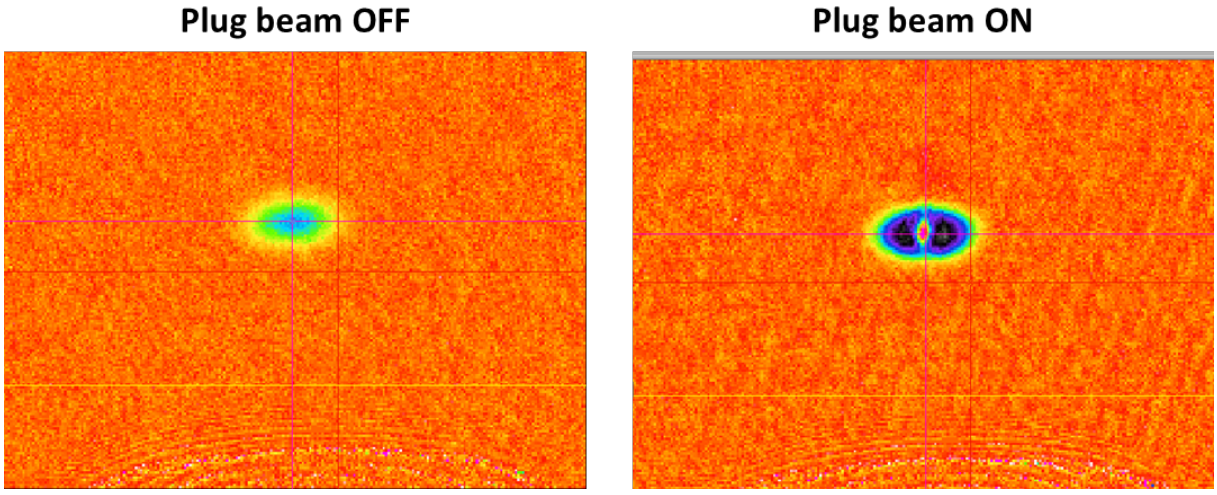

Figure 4.13: False colour absorption images of the atom cloud after identical evaporative cooling stage with and without the optical plug beam. The colours represent the optical density of the atoms. On the right, a blue-detuned laser beam with $\lambda = 760\,\text{nm}$ and ≈ 1, W power is focused at the center of the atom cloud to exclude the atoms from the region in space where $|B_{DC}(\boldsymbol{r})| = 0$ to prevent Majorana losses.

4.6 Atom Transport

Atoms can move around in space by changing the applied magnetic fields. Different configurations will cause the magnetic field zero region seen in figure 4.14 to appear at different locations. The simplest example of that would be moving an atomic ensemble along one dimension by applying a uniform bias field. In the 2D example, the DC field has the form

$$\boldsymbol{B}_{DC} = \frac{\partial B_{DC}\left(x,y\right)}{\partial r} r \begin{pmatrix} -x \\ y \end{pmatrix}, \tag{4.37}$$

where $r = \sqrt{x^2 + y^2}$, and the bias field can be described as

$$\boldsymbol{B}_{bias} = B_{bias} \begin{pmatrix} x \\ 0 \end{pmatrix} \tag{4.38}$$

with the total field written as

$$\boldsymbol{B}_{total} = \boldsymbol{B}_{DC} + \boldsymbol{B}_{bias}, \tag{4.39}$$

so the position of the zero-field region will depend on the magnitude of the bias field and the magnetic field gradient, $\partial B_{DC}/\partial r$. This method only works in the regime where B_{bias} is small because, due to the geometry of the coil, the quadrupole trap is only linear in magnetic field magnitude within a limited region in space.

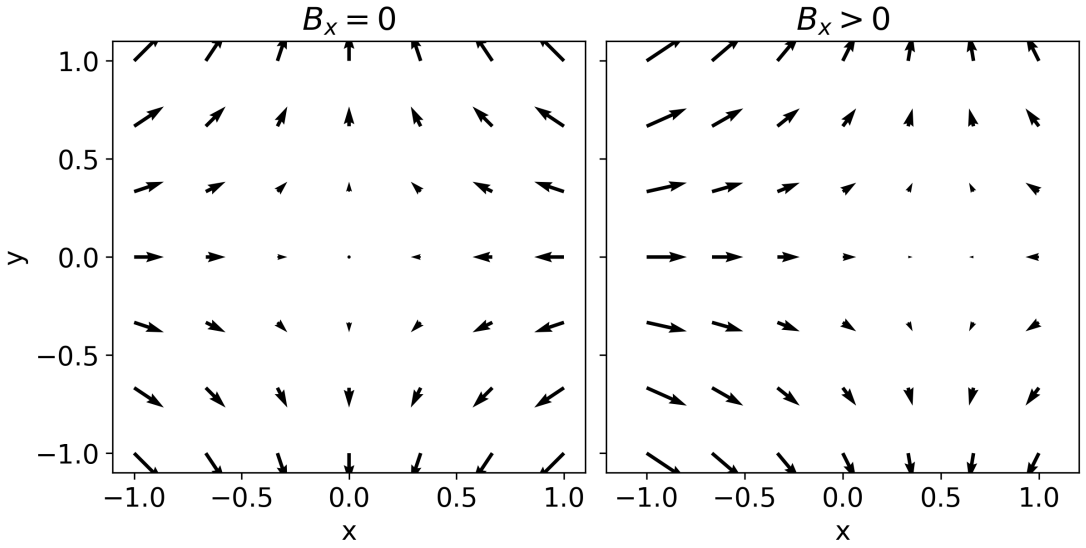

Figure 4.14: Quadrupole field zero being displaced by introducing a bias field.

In the experiment, the bias fields were adjusted in a particular order to move the atoms from an optically plugged quadrupole trap to an atom chip-based trap. Figure 4.15 shows the key parts of the loading sequence. The process involves bringing the atoms closer to the chip surface, compressing them, and then loading them into the atom chip trap. Unfortunately, due to the trap gradient and spatial mismatch, the handover procedure results in atom losses, with only about 10% of the atoms being loaded into the ring trap. We noticed that the number of atoms transferred into the ring trap increases with an increase in atom chip current; however, we are limited by the fact that the atom chip wires become too hot due to ohmic losses.

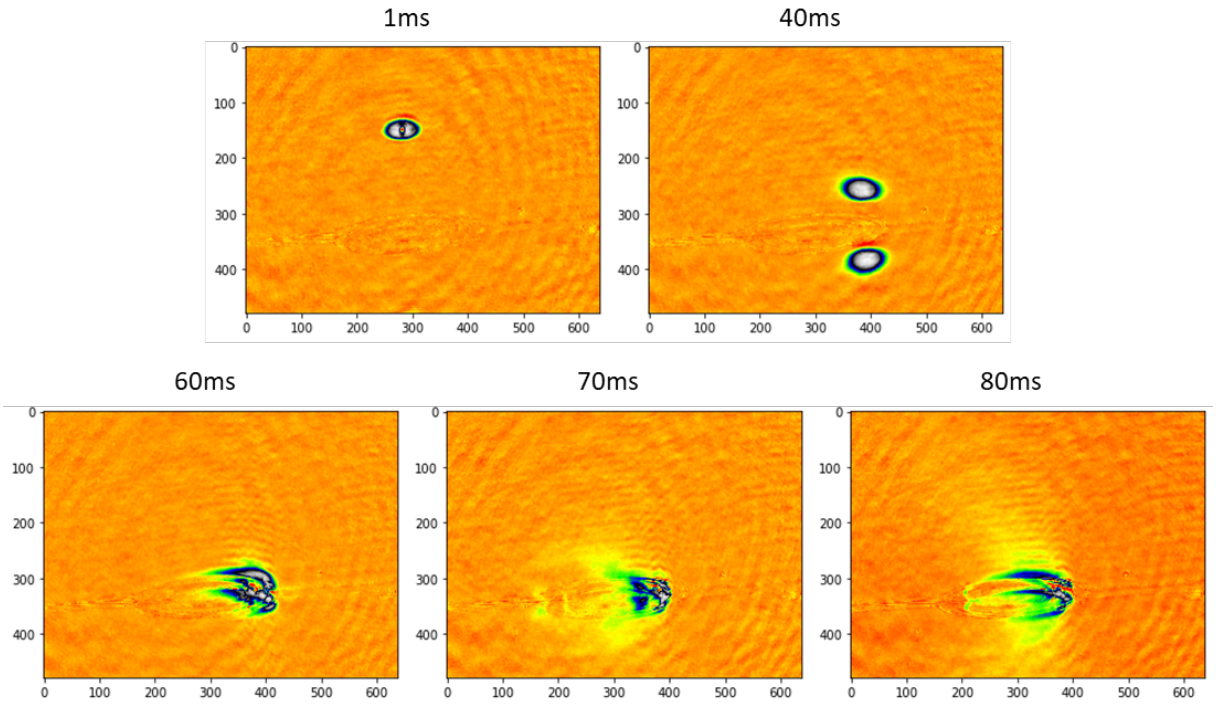

Figure 4.15: Loading of the Atom chip. False colour absorption images were taken during the atom chip loading stage with 1, 40, 60, 70, and 80 ms delay from the start of the stage. The x- and y-axes represent indices of 5.6 μm wide pixels.

The atoms can also be moved by applying currents to complex wire structures within the PCB or atom chip inside the vacuum chamber; however, the effects in this case are less predictable and require numerical analysis. The magnetic fields created by wire structures follow the Biot-Savart law, which we employ in our finite element analysis.

The simulation tools available to us can determine the position of zero-field locations as well as the size of the isopotential surface, which informs us of the trap gradient magnitude that we expect to see.

4.7 The Chip-Based Ioffe-Pritchard Trap

As mentioned in section 2.4, adiabatic loading of atoms into RF-dressed potentials requires a Larmor precession frequency above ω_{RF} at the trap bottom. The RF dressing frequency of 1MHz was chosen for two reasons. Firstly, the rotating wave approximation breaks down at a lower limit where higher order time-dependent terms under rotation about the quantisation axis are discounted. The high RF power required for atom confinement leads to the condition where $\Omega_{RF,Rabi} \approx \omega_{RF}$ and thus the RWA becomes invalid. Second, the RF electronics produce frequency harmonics, which causes increased atom losses. At the required RF power the higher harmonics are strong enough to completely remove the atoms from the trap within a few miliseconds.

The lifted trap bottom is achieved by forming an Ioffe-Pritchard-type trap with an atom chip field and bias field. The trap forms due to the residual field created by the atom-chip lead wires. A simulation of the conducting structures shown in figure 4.16 verifies that one can continuously switch between a ring quadrupole and an IP trap just by changing the applied external bias field pointing perpendicular to the lead wires. The simulation results estimate the transverse magnetic field gradient in this trap to reach $\approx 1000 \frac{\mathrm{G}}{\mathrm{cmA}}$. The size of the trap volume is limited due to the fact that the atom chip was not initially intended to form this type of trap. This particular trap configuration was only identified after examining the results of magnetic field simulations.

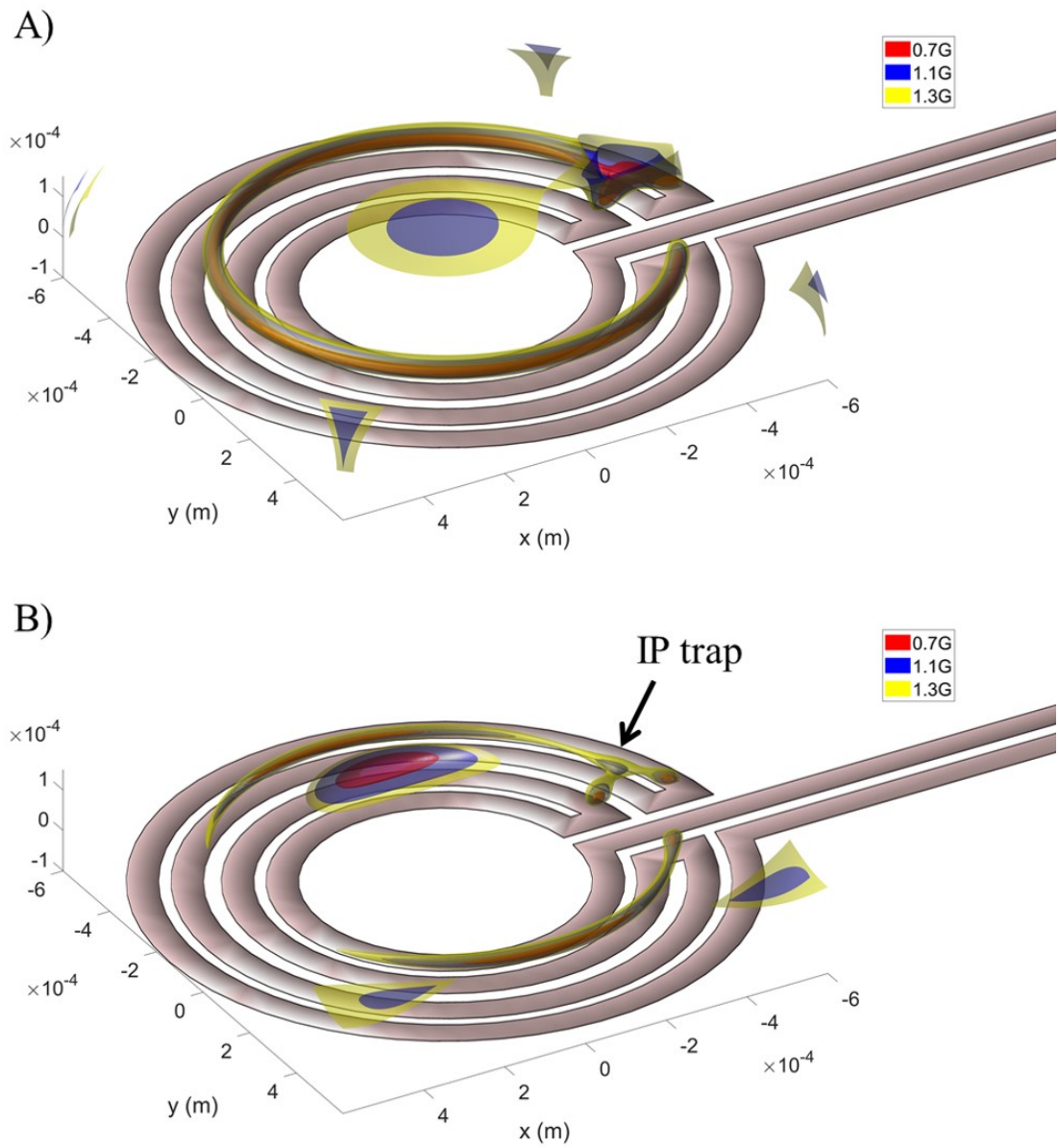

Figure 4.16: Formation of the Ioffe-Pritchard type trap by the EM chip wire structure running 0.3 A current. Ring quadrupole (A) is turned into an Ioffe-Pritchard trap (B) by applying a magnetic bias field of 1.5 G in the y-direction. Different colours indicate surfaces where the magnetic field magnitude is a constant value.

Initially, the bottom of the trap is kept low (around 0.45MHz) to maintain a high potential depth. Here, the atoms are evaporatively cooled down to $\approx 10\mu K$ with a frequency ramp from 4.00MHz to 0.95MHz in 2.6 seconds. Later, the applied external bias field is increased to set the minimum Larmor precession frequency to 1.04MHz which is just above the RF dressing frequency of 1MHz. During each operation an RF spectrum was taken to verify the success of each stage and the results have been presented in figure 4.17.

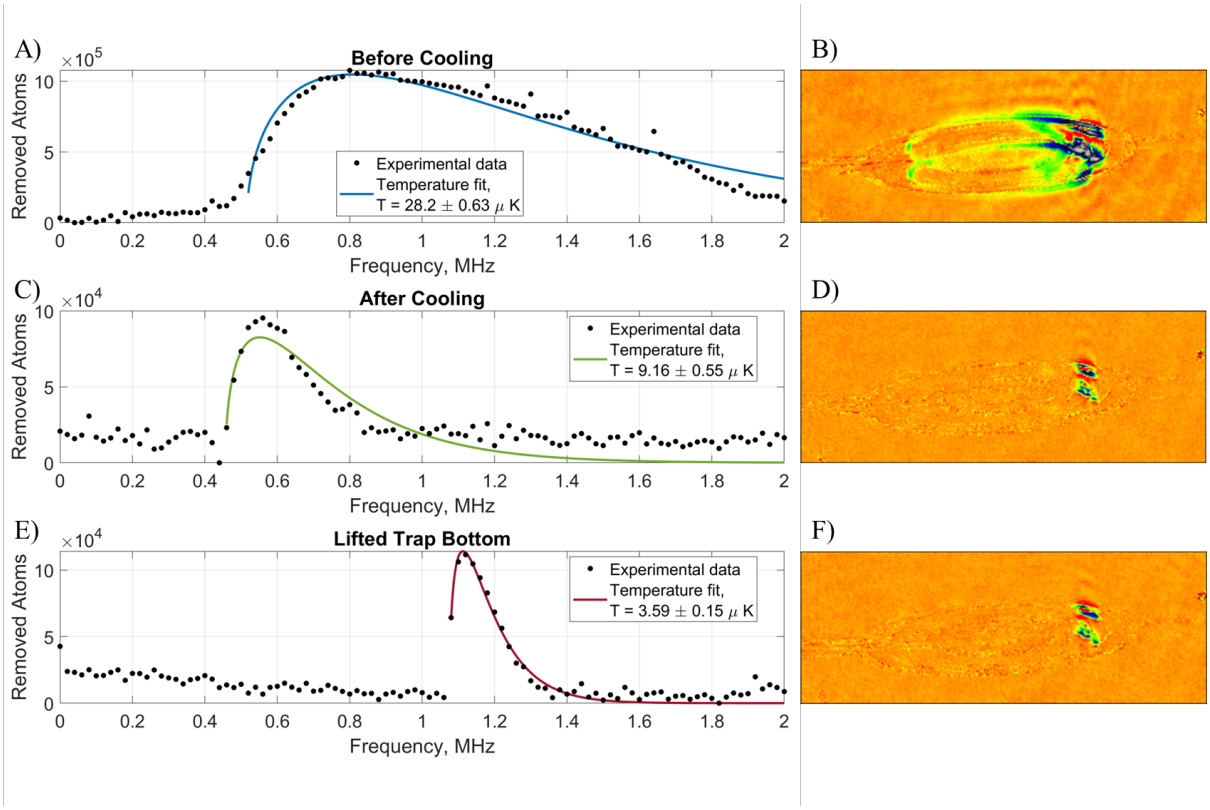

Figure 4.17: RF spectroscopy signal of atoms in IP trap before the RF cooling ramp (A, B), after RF cooling ramp (C, D), and after increasing the magnetic trap minimum field (E, F). Figures on the right (B, D, F) show false-colour absorption images of the atoms with the colour representing the optical density of the medium.

4.8 MW Pulses

So far, we have been observing atoms guided in the $|F = 2, m_F = 2\rangle$ state. As described in chapter 2, the Sagnac interferometer requires a superposition between states $|F = 1, \bar{m}_F = -1\rangle$ and $|F = 2, \bar{m}_F = 1\rangle$. We employ timed MW pulses to achieve the desired initial state. In the non-dressed picture, there are nine available MW transitions with seven distinct frequencies that can couple $F = 1$ and $F = 2$ manifolds. Each of these frequencies is labelled with a group number n like shown in the figure below.

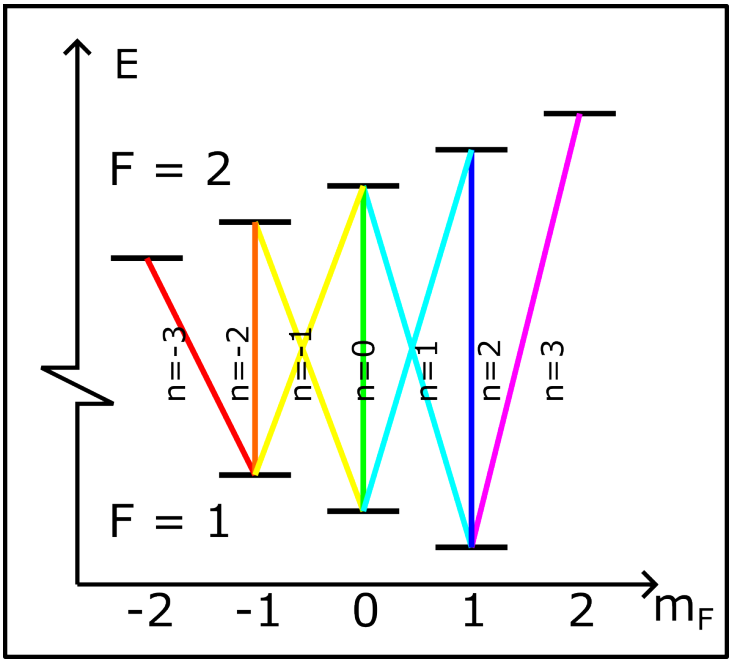

Figure 4.18: Different available MW transition frequencies within the ground state manifold depicted in different colours. Although there are 9 possible transitions, only 7 distinct frequencies are available with group labels $n = -3, -2, ..., 3$.

With atoms contained in the RF-dressed potentials, an additional structure appears [78]. The typical selection rules for each MW frequency and polarisation are no longer valid because a multi-photon transition is capable of coupling almost any two Zeeman sublevels between the two ground-state manifolds. The angular momentum can now be conserved on more transitions than before because the RF dressing field provides an additional degree of freedom to absorb excess angular momentum. The microwave spectrum of the RF-dressed atomic states features 7 groups of peaks, labelled in integer numbers from -3 to 3, each separated by $\omega_{larmor} = \omega_{RF,dressing}$ and each of the groups contains a number

of peaks equal to possible destination states, separated by effective Rabi frequency like shown in figure 4.19. For example, with the starting state $|F = 2, \bar{m}_F = 2\rangle$, there are three possible destination states: $|F = 1, \bar{m}_F = -1\rangle$, $|F = 1, \bar{m}_F = 0\rangle$, and $|F = 1, \bar{m}_F = 1\rangle$.

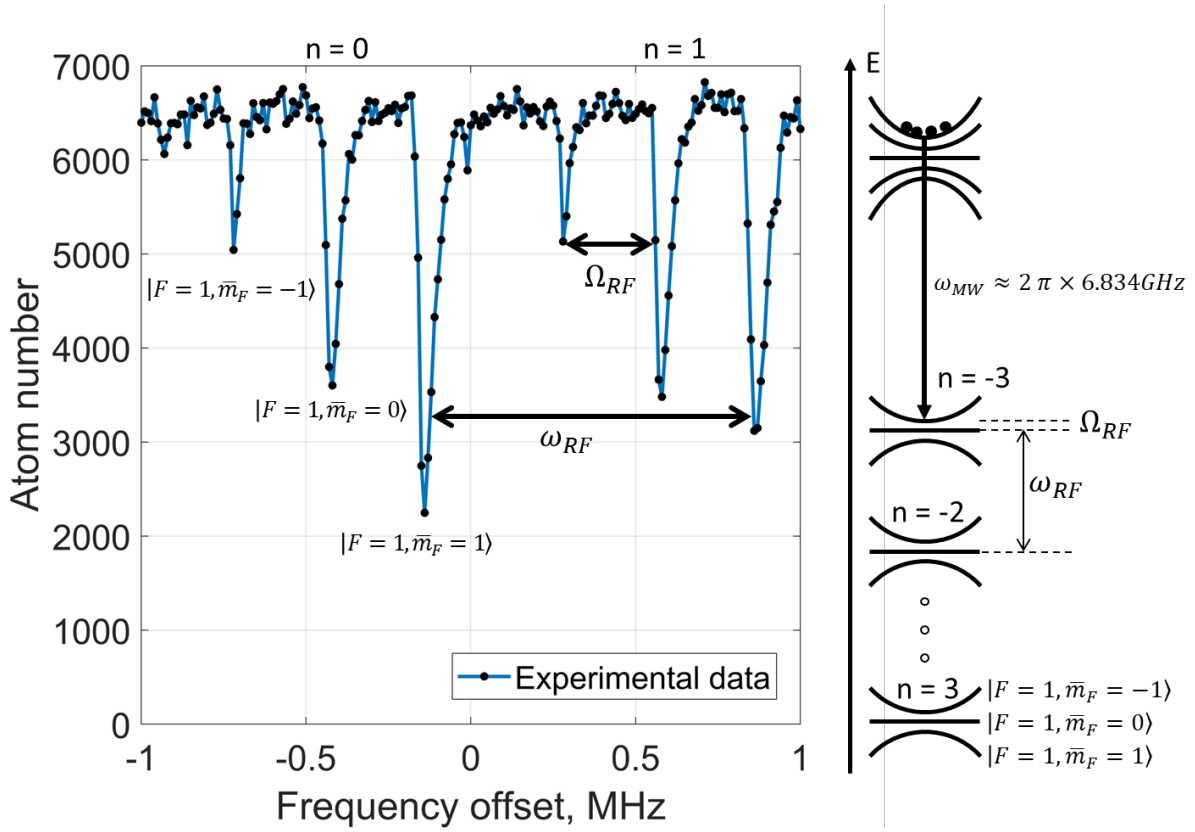

Figure 4.19: MW spectrum of RF-dressed atoms in IP trap with atoms starting in the RF dressed $|F = 2, \bar{m}_F = 2\rangle$ state. The diagram of the available transitions is displayed on the right: there are 7 groups of peaks, separated by ω_{RF}, where each peak within the group is separated by Ω_{RF} and corresponds to a specific RF-dressed state.

Figure 4.20 shows that the complex MW spectrum structure allows for seven different pathways to move atoms from the $|F = 2, \bar{m}_F = 2\rangle$ state to the $|F = 1, \bar{m}_F = -1\rangle$ state. The MW frequency is determined by measuring the coupling strength. We measure the rate of atom transfer into the $F = 1$ manifold and select the transition that transfers atoms to the $|F = 1, \bar{m}_F = -1\rangle$ state the quickest.

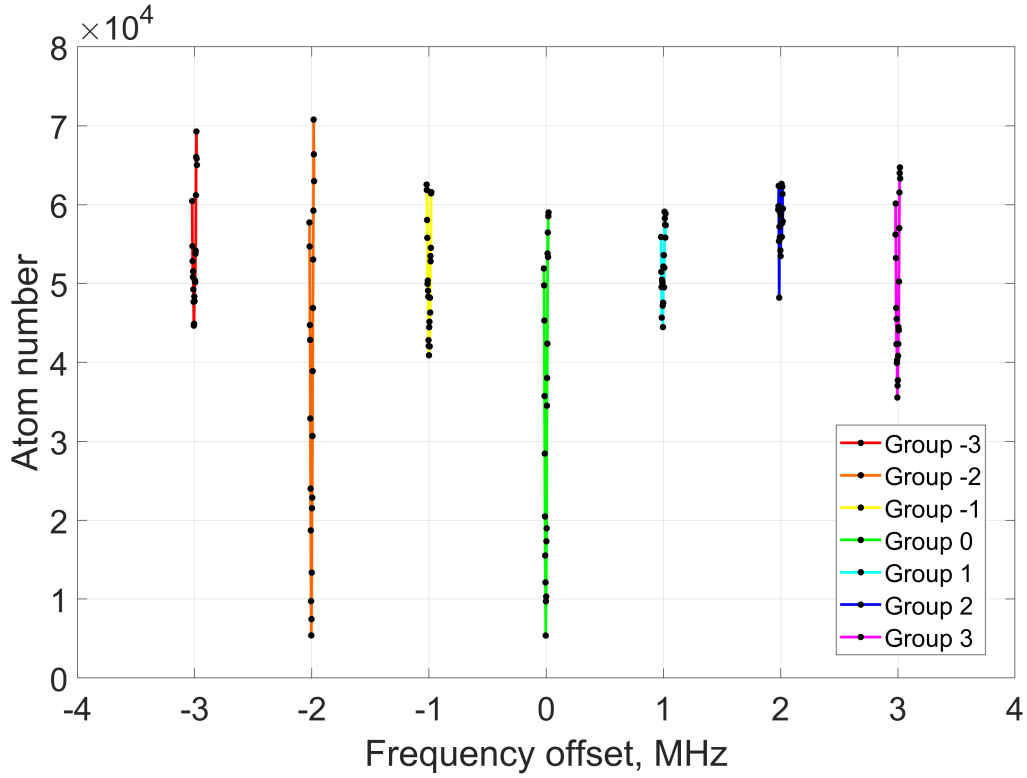

Figure 4.20: Spectroscopic measurements of MW coupling strengths for $|F = 1, \bar{m}_F = -1\rangle \leftrightarrow |F = 2, \bar{m}_F = 2\rangle$ transition across different groups. Here, 0 Hz offset corresponds to probe frequency of $\omega_{\text{probe}} = \omega_{\text{hfs}} = 2\pi \times 6.834..\,\text{GHz}$. Displayed is the number of atoms remaining in the $F = 1$ manifold with narrow frequency scans across individual transitions. If pulse durations are much shorter than a Rabi cycle, the amplitude of the peak indicates the relative coupling strength of each transition.

The transfer pulse is timed to maximise the number of atoms in the $|F = 1, \bar{m}_F = -1\rangle$ state. MW pulse timing is determined from the graph in figure 4.21. After the atoms have been transferred to the $|F = 1, \bar{m}_F = -1\rangle$ state, an imaging light pulse is used to remove any atoms that remain in the $F = 2$ manifold. The Rabi oscillations decay to 1/e amplitude within $0.073 \pm 0.005\,\text{ms}$ from F $= 1$ data and $0.095 \pm 0.022\,\text{ms}$ in F $= 2$ observations.

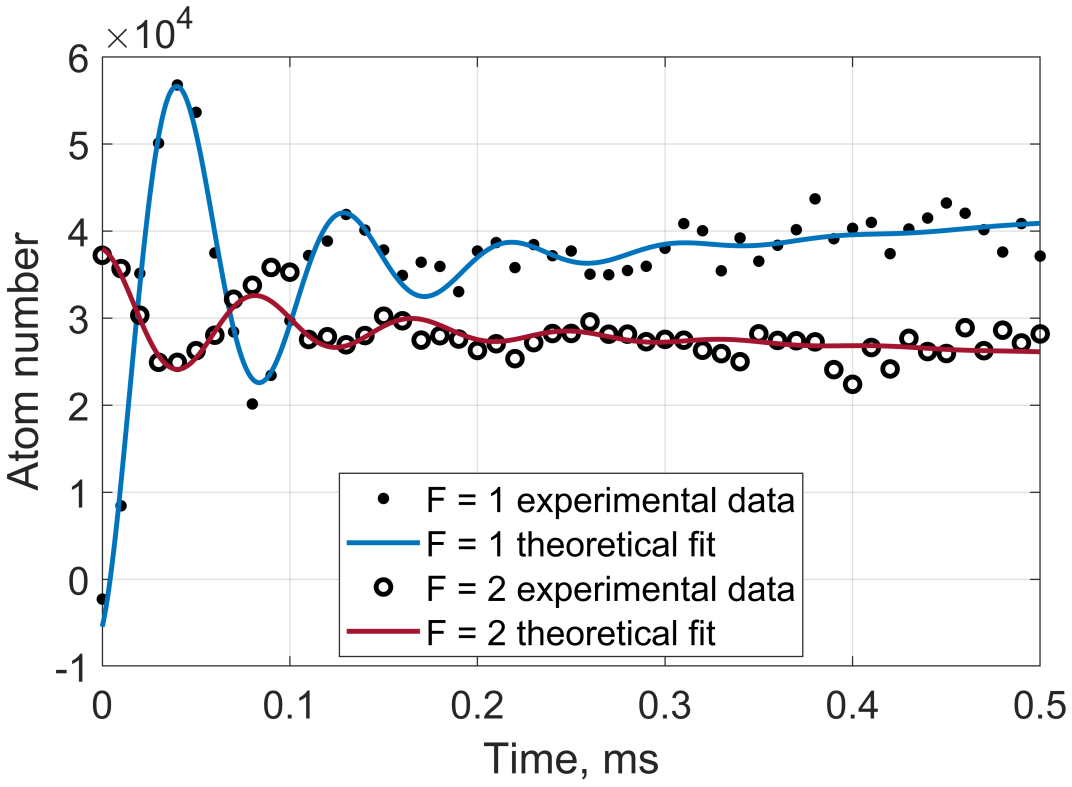

Figure 4.21: MW-driven Rabi flopping between $|F = 2, \bar{m}_F = 2\rangle$ and $|F = 1, \bar{m}_F = -1\rangle$ within group -2. The differences in the steady-state atom number for the two states can be attributed to changing background gas pressure over time. Negative starting number for F=1 is a data processing artefact.

The following MW pulse prepares the superposition between the two trappable states and, as before, we observe Rabi oscillations shown in figure 4.22 to select the most optimal group for the MW transfer pulse. We found that in our setup, group -2 works best.

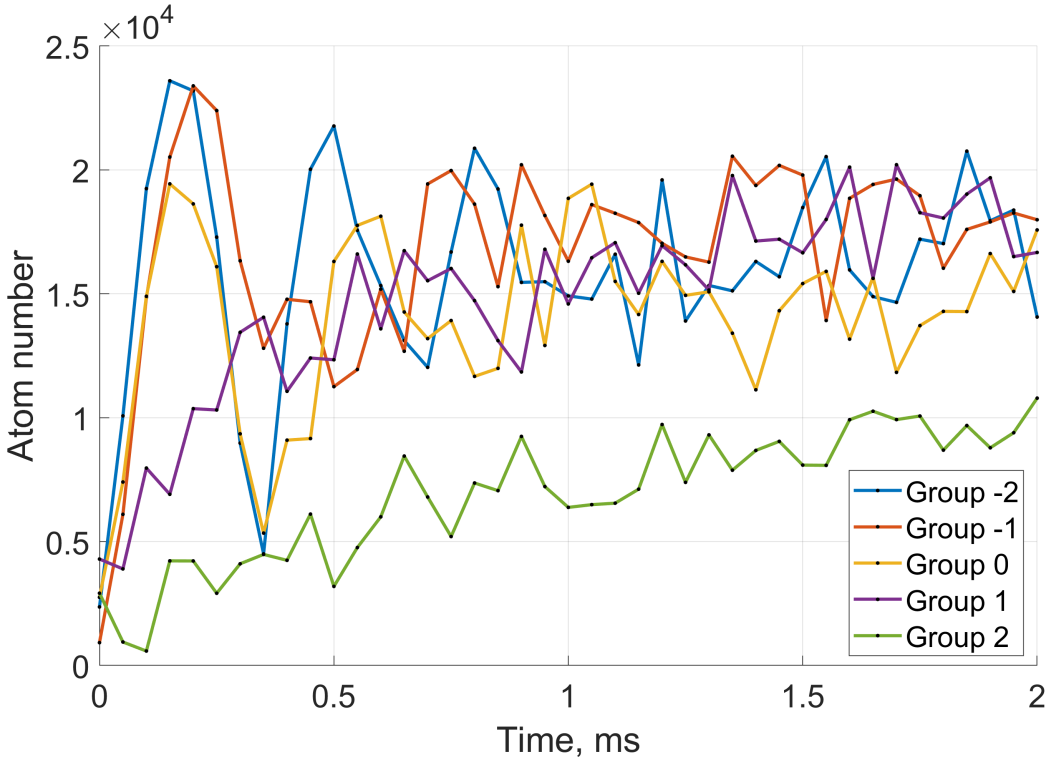

Figure 4.22: Rabi frequency measurement of $|F = 1, \bar{m}_F = -1\rangle \leftrightarrow |F = 2, \bar{m}_F = 1\rangle$ transition with different groups. X-axis represents the duration of the MW pulse.

The duration of the MW pulse is carefully timed to prepare an even superposition of $|F = 1, \bar{m}_F = -1\rangle$ and $|F = 2, \bar{m}_F = 1\rangle$. In our case, the $\pi/2$-pulse corresponds to $\approx 40\mu s$. Applying π- and $\pi/2$-pulses separated by time T, as described in Section 2.3, makes it possible to operate a Ramsey interferometer that reads out an interferometric phase as a population imbalance between states. However, for now, we only apply the first pulse in an RF-dressed IP trap because the Rabi frequency is larger than that in an RF-dressed quadrupole potential. A larger Rabi frequency increases the separation between peaks and helps to resolve the desired transition with hotter atoms.

4.9 Ramsey-Bordé Interferometer

With the MW pulse framework in place an interferometric sequence can be attempted without displacing the atoms between the pulses. As described in section 2.3, a sequence of $\pi/2-$ and π pulses, separated by time T, is applied to observe the interferometric signal which is read out as a population imbalance between atoms in the $F = 1$ and $F = 2$ manifolds. The first two MW pulses are applied in-phase with respect to each other, however, the last MW pulse has got a phase shift. Depending on the phase shift value, the measurement basis changes and thus, as seen in figure 4.23, the phase shift becomes imprinted onto the measurement result.

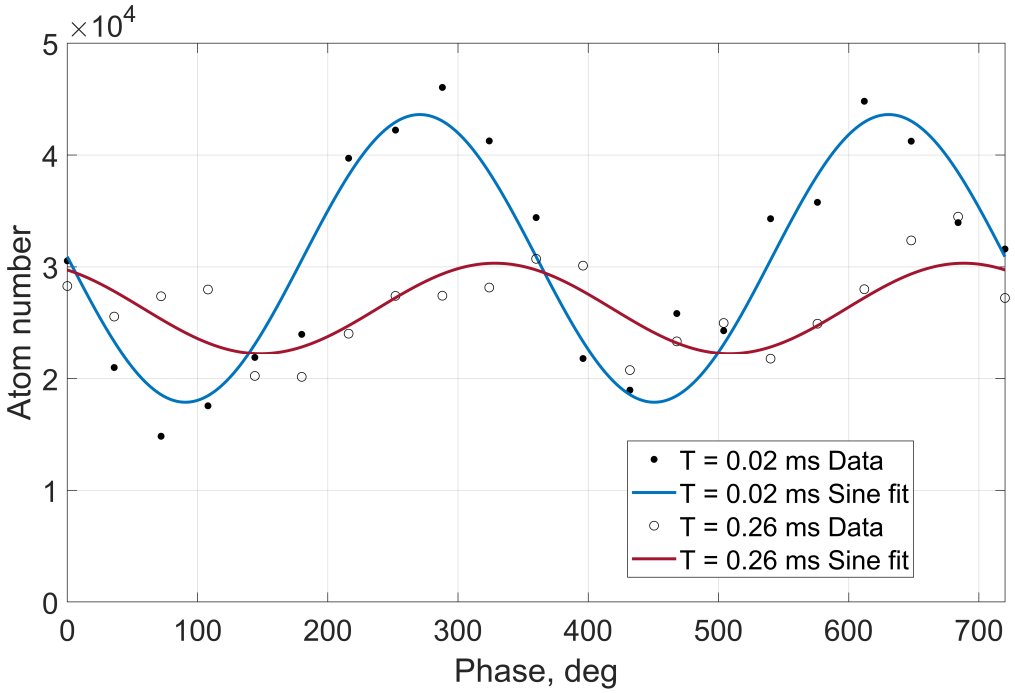

Figure 4.23: Ramsey fringes as a function of the final MW pulse phase shift with $T = 0.02ms$ and $T = 0.26ms$. Atom number measured in the $|F = 1, \bar{m}_F = -1\rangle$ state.

The contrast of the interferometer fringe defined as $C = \frac{N_{max}-N_{min}}{N_{max}+N_{min}}$ decays as a function of time T between each MW pulse [79]. In this paper multiple models are presented for different dynamical scenarios that all result in similar contrast behaviour. We choose one that describes a diffusive gas in a field gradient while the true situation in this trap can be represented by nearly ballistic motion of atoms in a harmonic potential.

$$C(T) \approx e^{(-2T/T_2)^3}, \tag{4.40}$$

where T_2 is the $1/e$ decay time of a spin-echo measurement, not to be confused with $1/e$ free induction decay time T_2^* which is typically shorter. The T_2^* time describes how fast the signal decays under constant MW radiation rather than a spin-echo sequence. From the data presented in figure 4.24 the measured value of the T_2 time was found to be on the order of 0.478 ± 0.035 ms, while the T_2^* time estimated from group $n = -2$ data in figure 4.22 is 0.65 ± 0.11 ms.

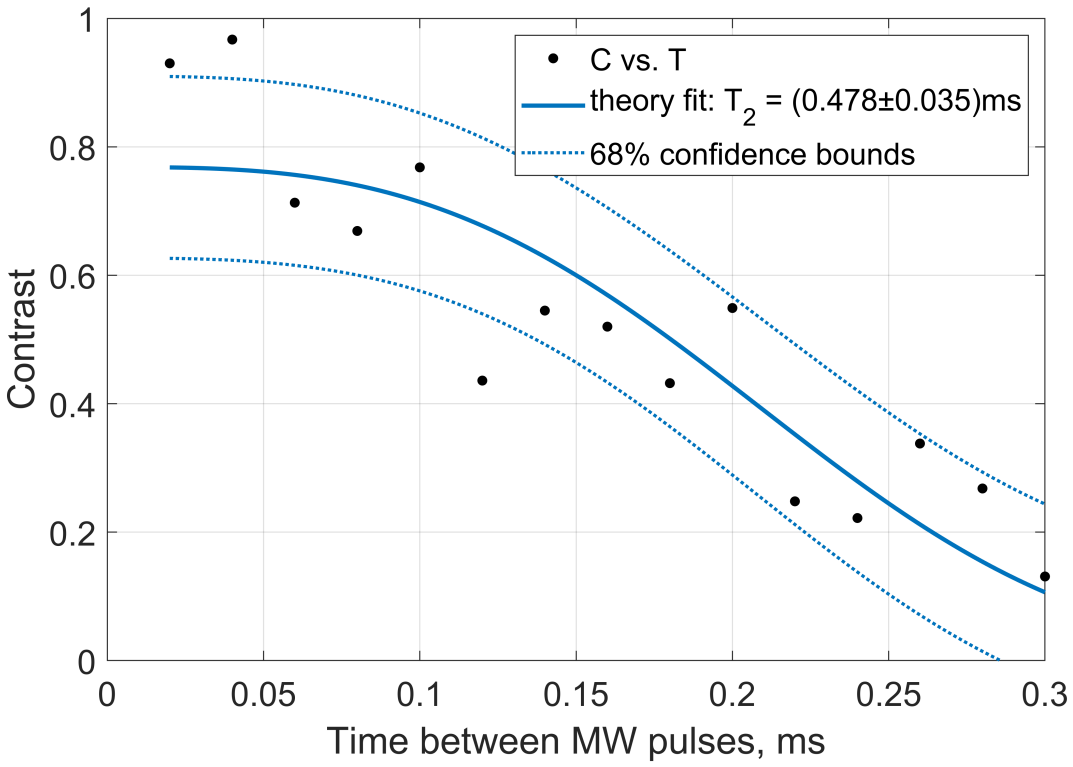

Figure 4.24: Ramsey fringe contrast decay measurement.

The decay time T_2 is governed by the width of the transition line $|F = 2, \bar{m}_F = 1\rangle \leftrightarrow |F = 1, \bar{m}_F = -1\rangle$. The sharpness of this transition line is limited by the magnetic field dependence of the energy difference between the trapped adiabatic states caused by the fact that the g-factor magnitude in ground state F-manifolds differs by about 0.5% [80]. This g-factor discrepancy can be reproduced by evaluating equations 2.23 and 2.24. Thermal motion of atoms across the magnetic trap means that the fixed transition frequency

becomes a distribution of frequencies with a finite width. According to figure 4.25 an RF-dressed trap with $\omega_{RF} = 1\text{MHz}$, trap gradient of $\frac{\partial B_{DC}}{\partial r} = 300\text{G/cm}$ and effective Rabi frequency $\Omega_{RF,Rabi} = 2\pi \times 300\text{kHz}$ will lead to $\approx 2\text{kHz}$ linewidth given that atoms are displaced by $50\mu\text{m}$.

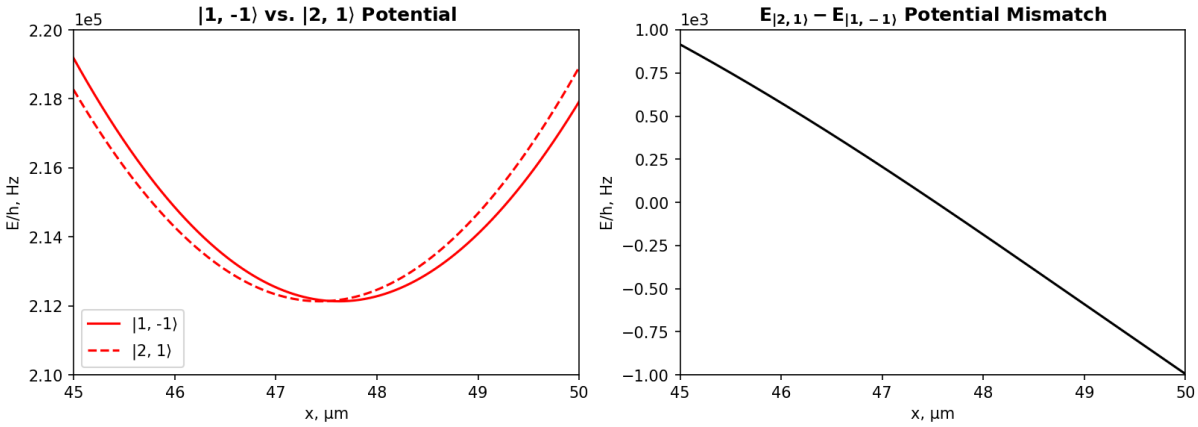

Figure 4.25: The RF-dressed potentials of the states $|F = 2, \bar{m}_F = 1\rangle$ and $|F = 1, \bar{m}_F = -1\rangle$ (left) do not overlap perfectly. The difference between these energy levels is given on the right.

The measured full width at half maximum of the transition in question is $\approx 2\text{kHz}$ when the atoms are cooled down to $1\mu\text{K}$. In figure 4.26 the transition linewidth has been measured at several probe power settings to ensure that the power broadening effects are avoided. A naive interpretation of this result leads us to believe that the contrast decay time is inversely proportional to the linewidth of the $|F = 2, \bar{m}_F = 1\rangle \leftrightarrow |F = 1, \bar{m}_F = -1\rangle$ transition, as $1/T_2 \approx 1/0.5\text{ms} = 2\text{kHz}$. Cooling the atoms to even lower temperatures can mitigate this effect, however, transferring atoms between mismatched potentials with MW pulses will lead to parametric heating.

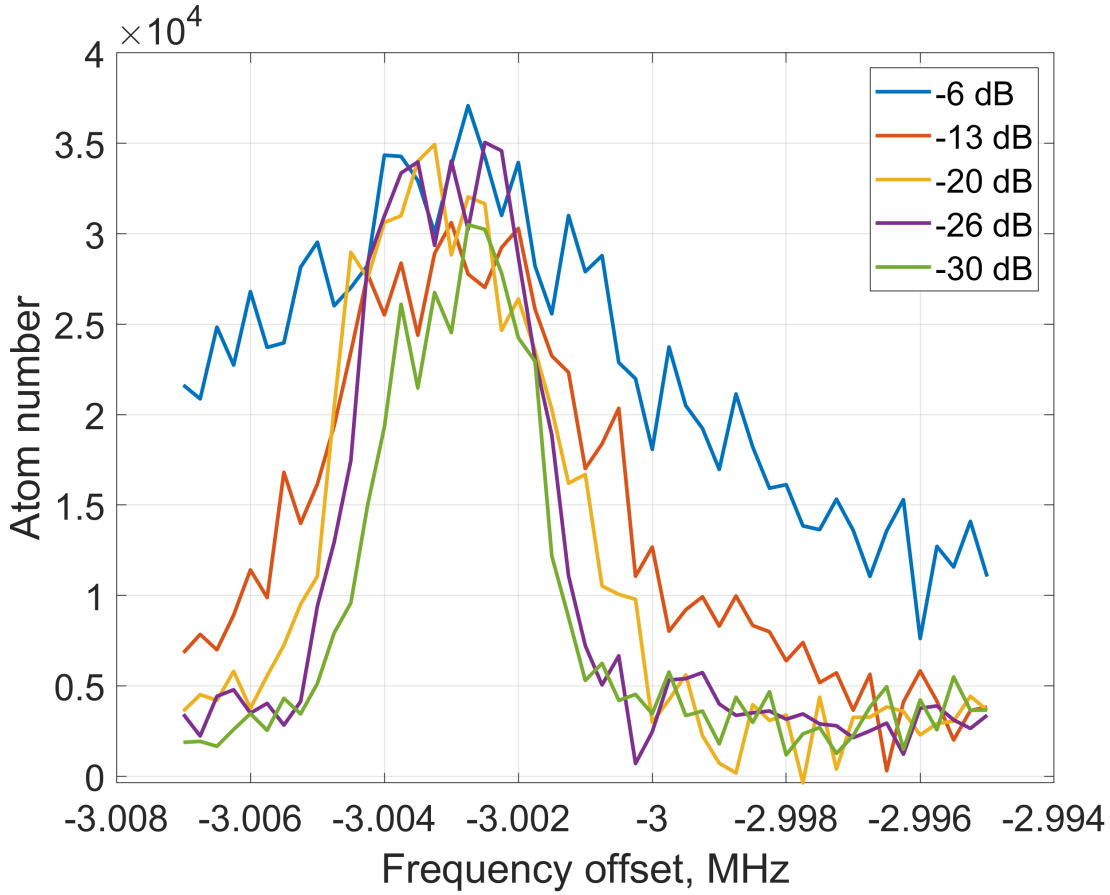

Figure 4.26: $|F = 2, \bar{m}_F = 1\rangle \leftrightarrow |F = 1, \bar{m}_F = -1\rangle$ linewidth measurement with different MW probe power strengths in group -3. Y-axis represents the atom number in the $|F = 2, \bar{m}_F = 1\rangle$ state. $\Delta f_{\mathrm{MW}} = 0$ occurs at $f_{\mathrm{MW}} = 6.834...$ GHz.

4.10 The RF Phase-Dependent Position Control

Atoms loaded into an IP trap with a sufficiently lifted trap bottom can be adiabatically transferred into an RF-dressed trap. A strong RF driving field produced by either RF chip coils or the C4 coil from the PCB interacts with atoms even when not on resonance. The applied dressing field magnitude of each source can be estimated through RF spectroscopy. According to [81], the atoms are resonant with the probing field at angular frequencies equivalent to $\Omega_{RF,Rabi}$, $\omega_{RF} - \Omega_{RF,Rabi}$, and $\omega_{RF} + \Omega_{RF,Rabi}$. We can prove this by looking at the applied RF probe field with some arbitrary polarisation and frequency ω_{probe}. The probing field in the lab frame of reference can be written as

$$\boldsymbol{B}_{lab} = \left(b_+\hat{\boldsymbol{e}}_+ + b_-\hat{\boldsymbol{e}}_- + b_0\hat{\boldsymbol{e}}_0\right) e^{i\omega_{probe}t} \tag{4.41}$$

In the reference co-rotation framework with the dressing field, the probe field can be defined by $\boldsymbol{B}_{rot}$

$$\boldsymbol{B}_{rot} = \left(b_+\hat{\boldsymbol{e}}_+ e^{-i\omega_{dress}t} + b_-\hat{\boldsymbol{e}}_- e^{i\omega_{dress}t} + b_0\hat{\boldsymbol{e}}_0\right) e^{i\omega_{probe}t}. \tag{4.42}$$

The effective magnetic field rotates from $\boldsymbol{e_0}$ by an angle $\alpha = \tan^{-1}\frac{\Omega_{RF,Rabi}}{\Delta}$, with $\Delta = \omega_{dress} - \omega_{Larmor}$. We then find an expression for an effective σ_+ component by rotating it around the y-axis by an angle α in the frame of reference co-rotating with the dressing field. The rotation is represented by a unitary matrix M.

$$\hat{\boldsymbol{e}}_{+,eff} = M\hat{\boldsymbol{e}}_+ e^{-i\sqrt{\Omega^2+\Delta^2}t}, \tag{4.43}$$

with M represented as

$$M(\alpha) = \begin{bmatrix} \cos\alpha & 0 & \sin\alpha \\ 0 & 1 & 0 \\ -\sin\alpha & 0 & \cos\alpha \end{bmatrix}. \tag{4.44}$$

We can now find the coupling coefficient between each of the probe field polarisation components and the atoms. We do this for each polarisation component and we name

the coupling coefficients A_+, A_-, and A_0.

$$|A_+| = b_+ \hat{\boldsymbol{e}}_+ \cdot \hat{\boldsymbol{e}}_{+,eff} e^{it\left(\omega_{probe} - \omega_{dress} - \sqrt{\Omega^2+\Delta^2}\right)} \tag{4.45a}$$

$$|A_-| = b_- \hat{\boldsymbol{e}}_- \cdot \hat{\boldsymbol{e}}_{+,eff} e^{it\left(\omega_{probe} + \omega_{dress} - \sqrt{\Omega^2+\Delta^2}\right)} \tag{4.45b}$$

$$|A_0| = b_0 \hat{\boldsymbol{e}}_0 \cdot \hat{\boldsymbol{e}}_{+,eff} e^{it\left(\omega_{probe} - \sqrt{\Omega^2+\Delta^2}\right)} \tag{4.45c}$$

From the equations above, it can be seen that the coefficient $|A_+|$ becomes time independent when $\omega_{probe} = \omega_{dress} + \sqrt{\Omega^2 + \Delta^2}$, $|A_-|$ resonates at $\omega_{probe} = \omega_{dress} - \sqrt{\Omega^2 + \Delta^2}$, and the exponential for $|A_0|$ becomes constant at $\omega_{probe} = \sqrt{\Omega^2 + \Delta^2}$.

In figure 4.27 one can see that for a fixed detuning, the coupling strength for different polarisations will vary depending on the magnitude of the applied RF dressing field. Within a static magnetic field, where the RF field is polarised precisely along $\boldsymbol{e}_\pm$ or $\boldsymbol{e}_\mathbf{0}$, only one of the peaks would be observed. We can observe all three peaks due to thermal motion of atoms within the trap.

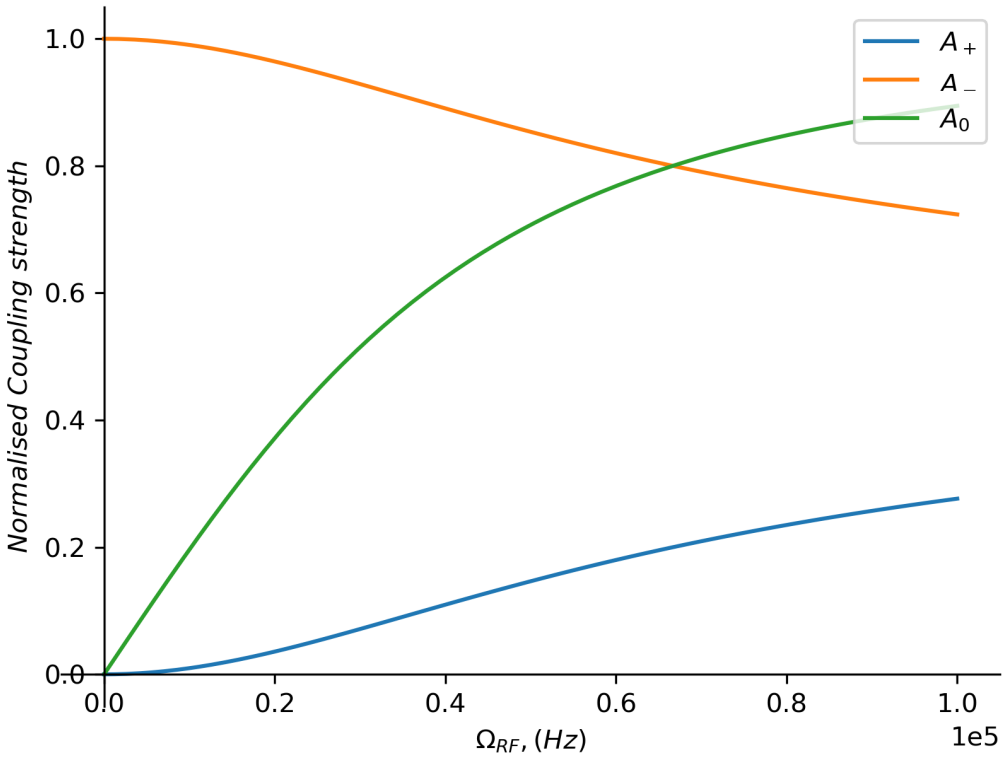

Figure 4.27: RF coupling strengths of different polarisation components. Here, $\Delta = 2\pi \times 50$kHz.

We have measured the RF coupling strengths of individual RF sources and found that the RF chip drives the atoms with an effective Rabi frequency of 240 kHz and the C4 field achieves 300 KHz. There are only two prominent peaks visible in figure 4.28; however, the peak corresponding to $\omega_{RF} - \Omega_{RF,Rabi}$ can also be seen with higher power or different RF polarisations.

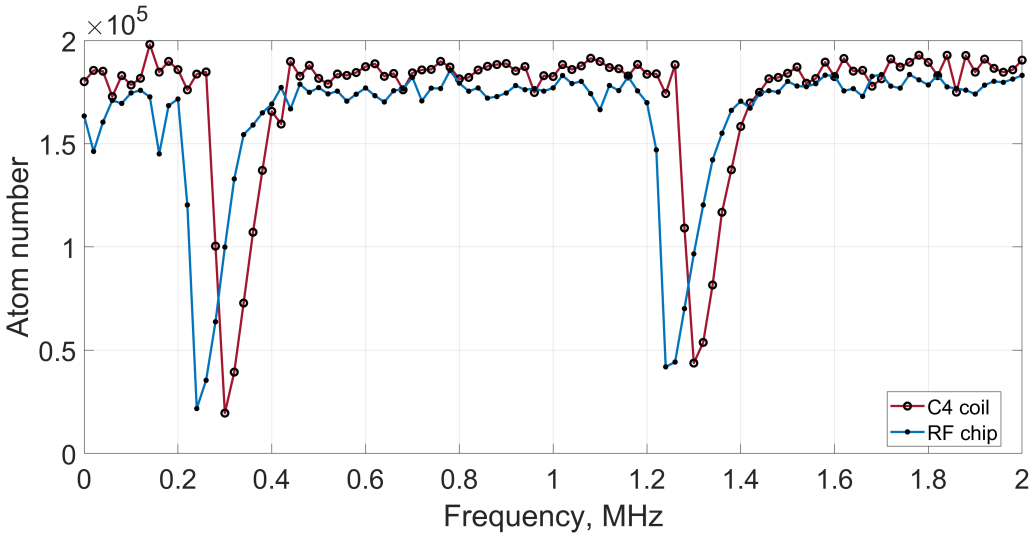

Figure 4.28: RF field strength measurement of RF chip and C4 coil fields.

The choice of the relative RF phase is made by looking at the Rabi frequency when both RF sources are switched on at the same time. The RF chip field is chosen to be the reference, and the C4 field is delayed by different amounts to achieve the desired phase offset. The measured Rabi frequency with one of the ground states only describes the magnitude of one circular polarisation. To get a full polarisation description, we need to observe the Rabi frequency in both F-manifolds at the same time. From results in figure 4.29 is it possible to determine that the angle RF chip and C4 coil field is $\approx 17°$. In the end, a phase of 118.8° has been chosen to produce an upright elliptical RF polarisation.

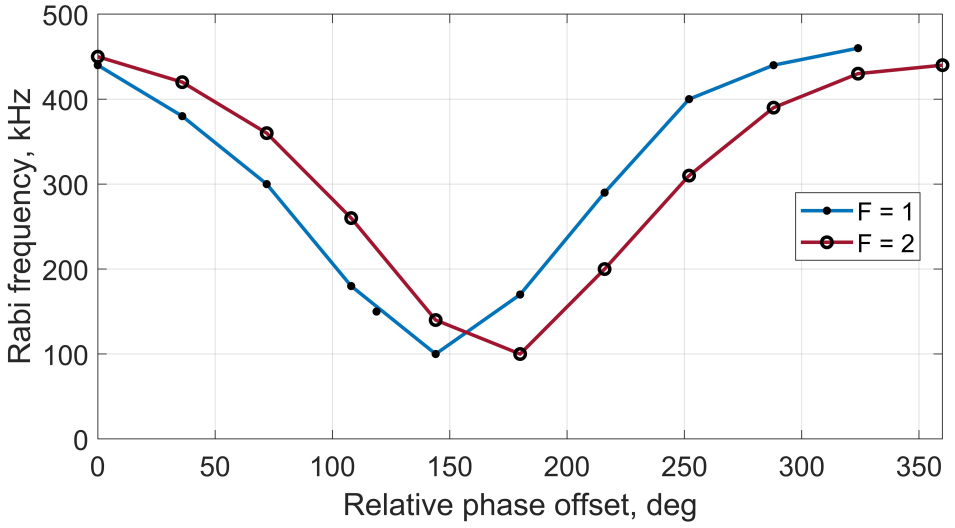

Figure 4.29: RF coupling strength changes with RF polarisation.

With fixed relative phase between the RF chip and C4 coils, the DC bias field produced by the compensation coils is lowered and the quadrupole trap is handed over to the top loop of the EM chip. This sequence transfers atoms from an RF-dressed IP trap into an RF-dressed quadrupole ring trap in an adiabatic manner. We observe the changes in the trapping potential during the DC field ramp by looking at the RF spectra of the atomic ensemble shown in figure 4.30. Without the dressing field, the potential minimum is lowered towards zero, whereas with the RF dressing field switched on, the atoms remain confined to the resonant surface, allowing us to observe typical spectroscopic features around a dressing frequency of 1 MHz. The effective Rabi frequency is lowered in the RF-dressed quadrupole trap as a result of a change in the direction of the static magnetic field with respect to the RF field.

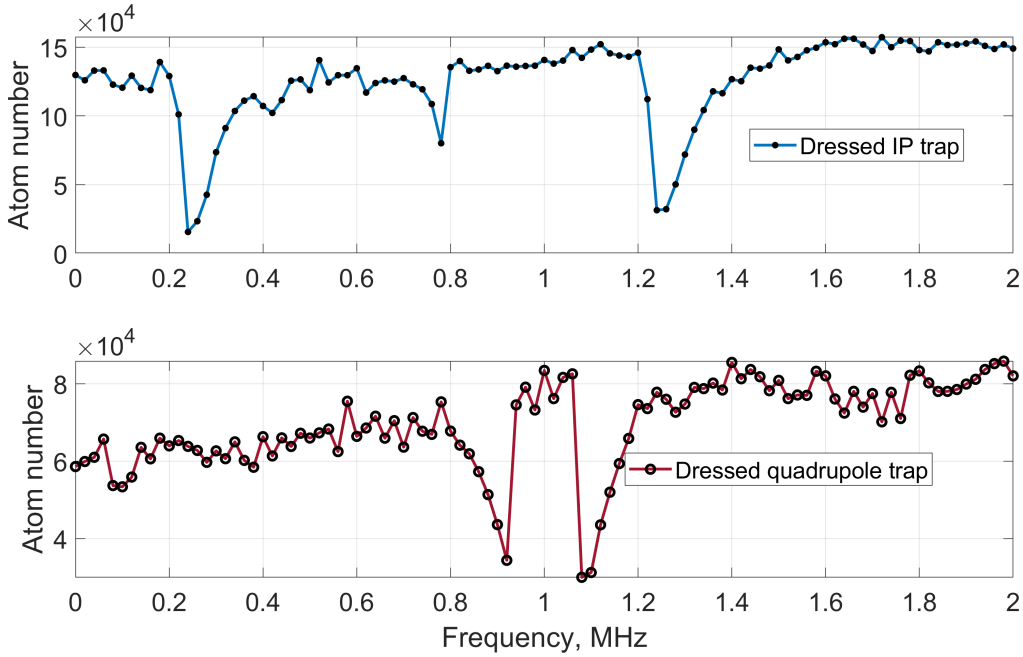

Figure 4.30: RF-dressed atom cloud spectrum in IP trap (top) vs. quadrupole ring trap (bottom).

Another key observation made to verify that the atoms were loaded into the RF-dressed potential comes from lifetime measurement presented in figure 4.31. Atoms confined to the resonant surface do not cross the DC zero-field region and therefore they do not undergo Majorana spin flips, keeping the atom lifetime much longer.

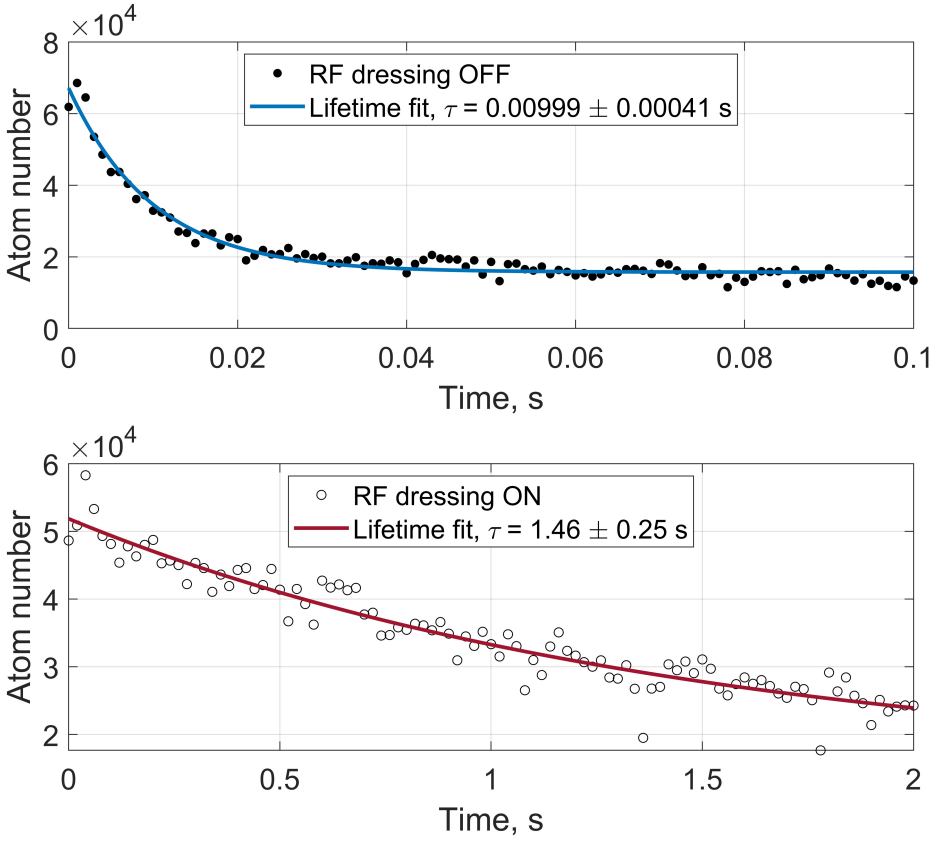

Figure 4.31: Lifetime of atoms in bare ring quadrupole (top) vs. lifetime in RF-dressed ring quadrupole trap (bottom).

After the successful ramp into the RF-dressed quadrupole ring trap, we can introduce the linearly polarised RFx field, which interferes with the radial component of the elliptically polarised RF field, produced by the RF chip and C4 coils. The magnitude of the RFx field was measured by keeping the atoms confined by the DC potentials while varying the relative phase of the RFx field and estimating the resulting Rabi frequency through RF spectroscopy. With the current setup it is possible to modulate the effective Rabi frequency by $\pm 2\pi \times 25$kHz. These measurements predict the formation of an RF-dressed potential with traps slightly tilted with respect to the z-axis as seen in figure 4.32.

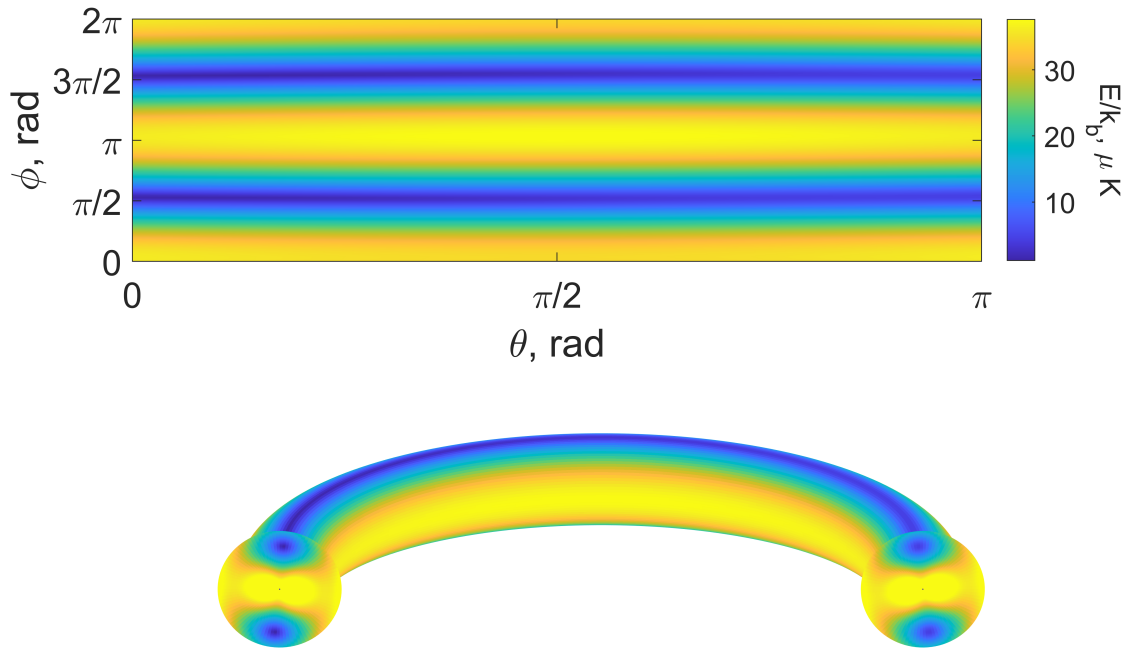

Figure 4.32: Theoretical prediction of the RF-dressed trapping potential based on experimental measurements.

To change the phase of the RFx field, we introduce a small frequency shift to the RFx field with respect to the elliptical dressing field and wait for a fixed amount of time. In this part of the experiment, the atoms remain in the $|F = 2, \bar{m}_F = 2\rangle$ state to maintain a higher potential gradient and keep the number of atoms as high as possible. We always wait for 100 ms to give the atoms enough time to settle down and change the frequency offset by $\pm$5Hz. Depending on the frequency shift, the relative phase of the RFx field varies and, therefore, we locate atoms in different positions around the ring. We should be able to observe two clouds trapped in potentials at the top and bottom of the torus moving in counter-propagating directions due to inverted static magnetic field direction in each trap. In this case, however, only one of the two ring traps is loaded. This happens due to gravity pulling the atoms out of the weaker trap formed further away from the chip surface.

Having verified the working principle of our control scheme, we can attempt to transport the atoms in the $|F = 2, \bar{m}_F = 2\rangle$ state around the entire loop. The RFx field frequency

is ramped up by 5 Hz, and, due to the resulting phase shift of the in-plane RF field, we observe atoms travelling counterclockwise. The atoms are transferred from top EM chip loop trap to the trap generated by the bottom layer structure to avoid guiding the atoms over the lead wires. Unfortunately, because the longitudinal trapping potential is quite shallow, the atomic ensemble spreads a bit too wide, and the edge of the cloud still interacts with the lead wire discontinuity at 150 ms. The results of these experiments are presented in figure 4.33.

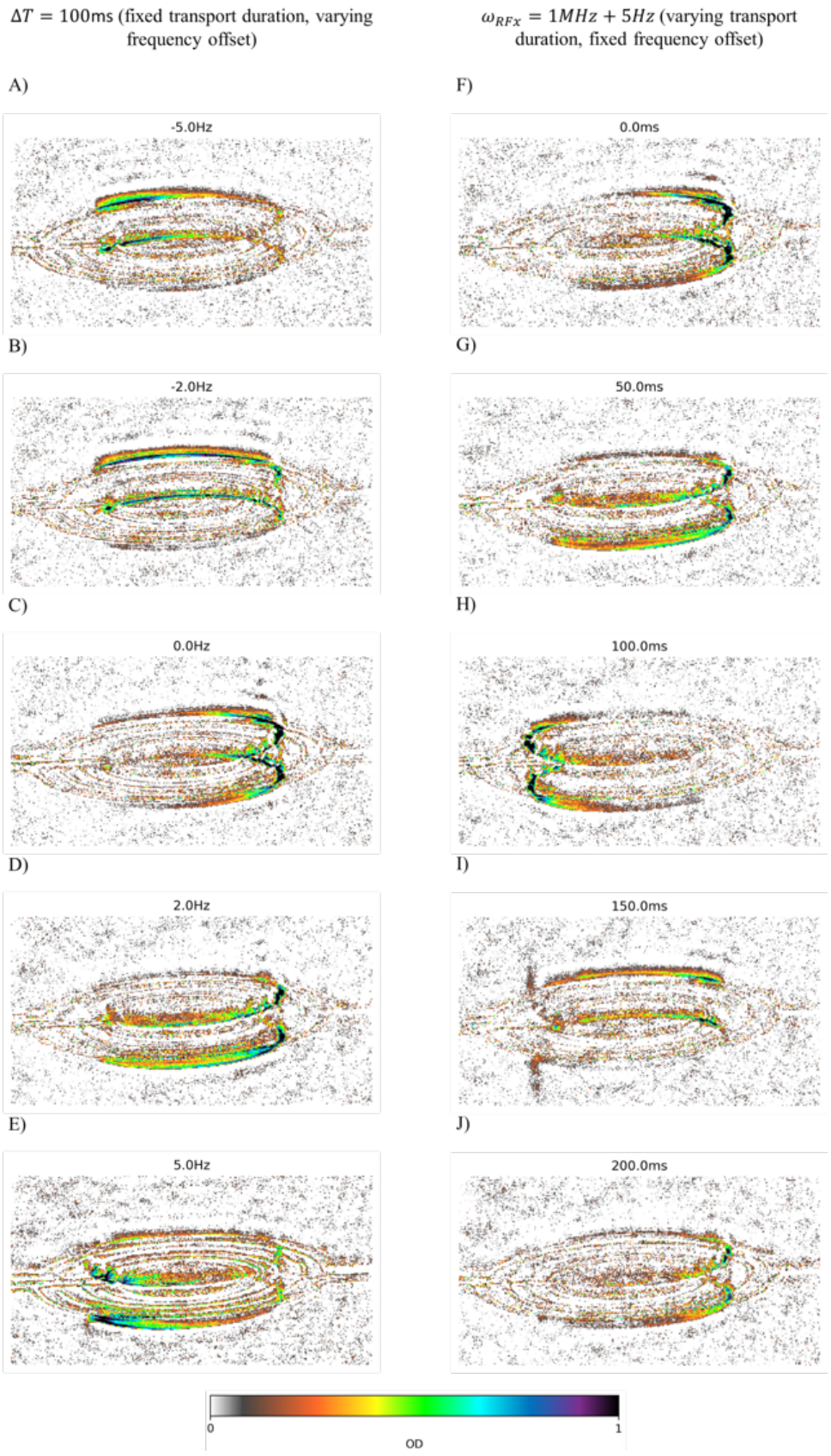

Figure 4.33: False colour absorption images of RF-dressed trap evolution with fixed transport duration on the left column (A – E) and fixed RFx frequency offset on the right (F – J). Here we observe atoms in $|F = 2, \bar{m}_F = 2\rangle$ state.

The total duration of the round trip is 200 ms, as seen in figure 4.34. The angular position of the atom cloud was extracted by determining the center of mass position within each frame of the experimental sequence. Linear fit of the graph confirms that the atoms are being guided around the ring at a fixed rate rather than being accelerated.

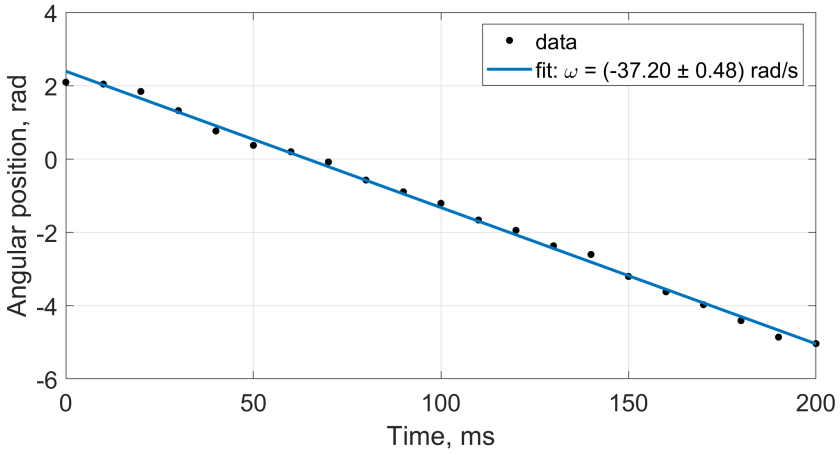

Figure 4.34: Plot of atom cloud angular position during the transport stage where the RFx coil frequency offset is +5Hz. The rotation rate of the atom cloud is estimated to be $37.20 \pm 0.48\,\mathrm{rad/s}$.

With this transport scheme it is possible to complete 9 full loops, since the lifetime of atoms in the stationary trap has been measured to be 1.8 seconds, as shown in figure 4.35. The RFx coil deepens the trapping potential and the lifetime measurement is different from the data presented in Figure 4.31. Notably, no decrease in the lifetime of atoms in the trap has been observed as a result of the addition of an RFx field.

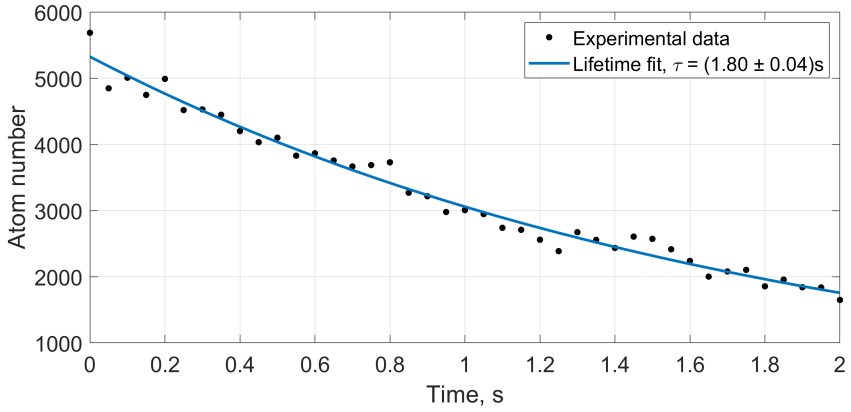

Figure 4.35: Lifetime measurement data of stationary atoms in an RF-dressed ring quadrupole trap.

The temperature of the dressed ring quadrupole trap was measured before and after the transport sequence. The atomic ensemble has heated from $3.48 \pm 1.65\mu$K to $5.20 \pm 2.51\mu$K, which corresponds to a heating rate of 8.6μK/s. The heating rate puts a limit on how many loops we can achieve, however, the heating rate can be significantly reduced by employing optimal control techniques to accelerate atoms smoothly [82].

We then prepared atoms in a superposition of two states, $|F = 1, \bar{m}_F = -1\rangle$ and $|F = 2, \bar{m}_F = 2\rangle$, and repeated the guiding procedure with the RFx field frequency offset set to $\pm$2Hz. The atoms always began in the same position, determined by the IP trap, and ended up in different places depending on the RFx field frequency offset and the atomic state. When the RFx field was changed by +2Hz, the atoms in the $F = 2$ state were guided clockwise and the atoms in the $F = 1$ state moved counterclockwise around the ring trap. The positions of atoms in different ground states after 100ms transport stage are displayed in figure 4.36. When the frequency shift of the RFx field was set to -2Hz, the atoms started to move in opposite directions: atoms in the $F = 2$ manifold were guided counterclockwise and atoms in the $F = 1$ state were moved clockwise.

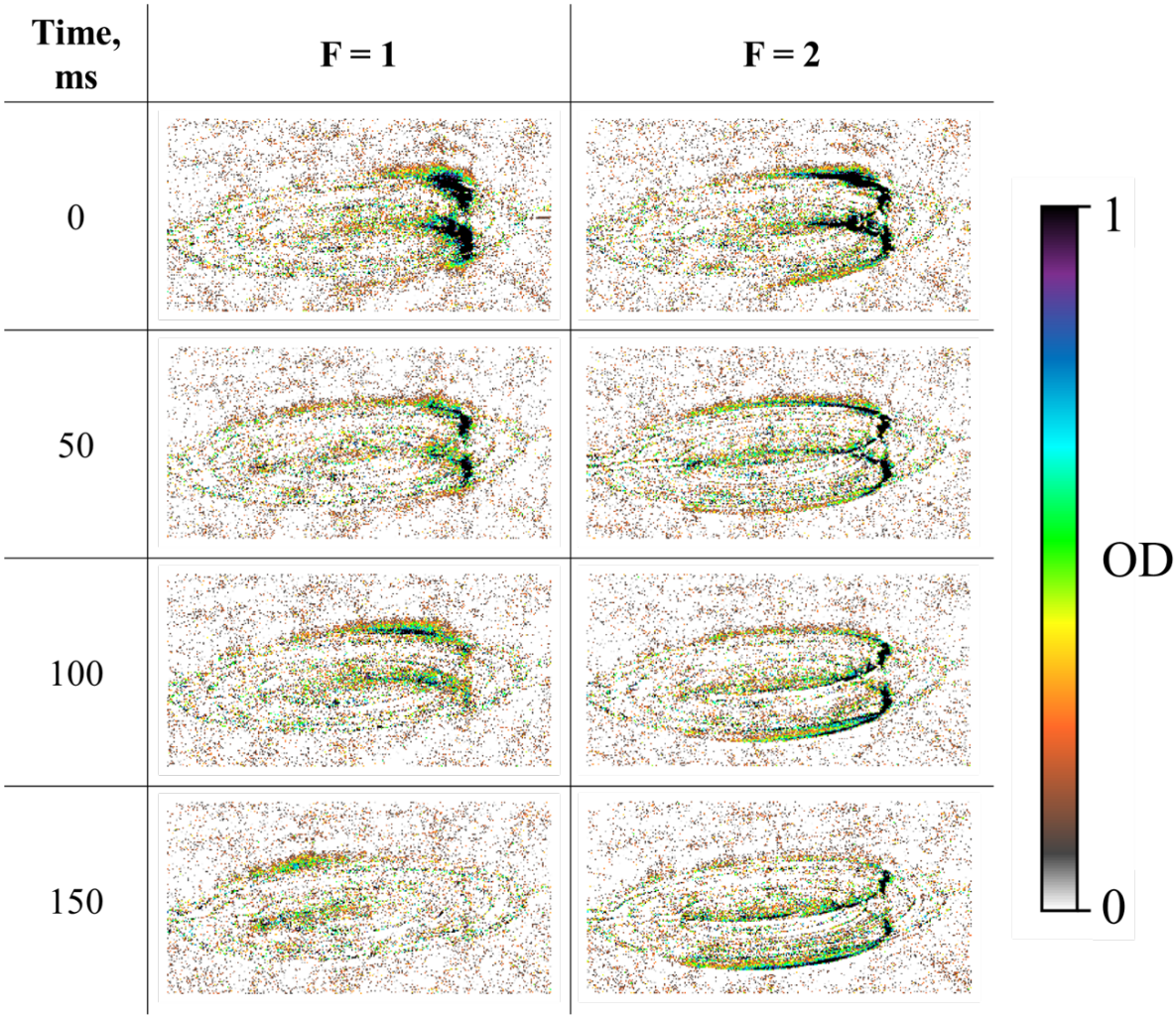

Figure 4.36: Absorption imaging figures of atoms in a state-dependent RF-dressed trap during transport via potential modulation. The left column shows atoms in $|F = 1, \bar{m}_F = -1\rangle$ and the right column displays atoms in $|F = 2, \bar{m}_F = 2\rangle$ state. Modulation field produced by RFx coil has a +2Hz frequency offset with respect to the smoke ring dressing field, the trap radius is 0.5 mm.

There are two RFx field phase values where the trap positions in states $F = 1$ and $F = 2$ overlap. This defines two possible locations where MW π-pulses can be applied. The trap overlap location can be controlled arbitrarily by introducing an RFy field to control the polarisation of the linearly polarised RF field in the x-y plane.

Chapter 5

Summary and Reflections

In conclusion, the experiments have shown that the atom chip is capable of producing DC trapping fields that provide enough potential for trapping, and the RF-dressed transport scheme is able to move the atoms around the ring-shaped guide. Additionally, the MW setup has been constructed and its operation has been confirmed through interferometric and spectroscopic measurements. This has enabled the observation of Rabi cycles and other important spectroscopic features in the MW range, thus demonstrating the ability to create quantum superpositions of atoms in a materwave Sagnac interferometer.

5.1 MW Dressing

The discrepancy between the Ramsey-Borde interferometer coherence time ($T_2 \approx$ 0.5ms) and the time it takes for ^{87}Rb atoms to complete a full loop around the atom chip guide ($T_{guide} \approx$ 200ms) is a major issue. To address this, two approaches can be taken: creating tighter traps to accelerate the atoms faster and using MW dressing fields to enhance the $|F = 2, \bar{m}_F = 1\rangle \leftrightarrow |F = 1, \bar{m}_F = -1\rangle$ transition linewidth, as described in B. Foxon's thesis [1]. The latter technique involves the application of off-resonant MW fields that couple atomic states, resulting in energy shifts δE that increase the spatial potential overlap between the $|F = 2, \bar{m}_F = 1\rangle$ and $|F = 1, \bar{m}_F = -1\rangle$ states. The energy states of ^{87}Rb can be shifted by applying a detuned MW field, with the shift dependent on the MW field power, coupling strength, and detuning.

$$\delta E = \frac{h}{2}\left(-\Delta + sign\left(\Delta\right)\sqrt{\Omega^2 + \Delta^2}\right) \approx h\frac{\Omega^2}{\Delta} \tag{5.1}$$

The Δ term is symmetrical on either side of the transition, but the coupling strength term, Ω, can be either positive or negative depending on the transition and frequency. Dr. Foxon's PhD thesis [1] provides an in-depth analysis of the coupling strength for different polarisation components and transitions. Her experiments showed that the MW dressing scheme can remove the magnetic field dependence on the transition frequency to the first order when in free-fall. Additionally, using multiple MW frequencies at once can reduce the transition linewidth to approximately 100 Hz. To estimate the value of Ω for a transition $|F, m\rangle \rightarrow |F', m'\rangle$ with a specified polarisation, the values from the tables in [1] can be used, where θ_F is defined as the angle of the effective MW field. As an example, the coupling strengths for different transitions and σ^--polarised MW field have been presented in table 5.1.

$$\theta_F = \frac{\pi}{2} - \tan^{-1}\left(\frac{B_{DC} - B_{res,F}}{\sqrt{2}B^{\pm}_{RF}}\right) \tag{5.2}$$

We select a frequency that interacts strongly with only one of the two states of interest that can be trapped. Depending on the amplitude and polarisation of the microwave

transition	$\hat{H}_{MW}^{-,n=-3}/\Omega_{norm}^{-}$	$\hat{H}_{MW}^{-,n=-1}/\Omega_{norm}^{-}$	$\hat{H}_{MW}^{-,n=1}/\Omega_{norm}^{-}$
$\|1,-1\rangle \leftrightarrow \|2,-2\rangle$	$\frac{1}{\sqrt{2}}(1+\cos\theta_1)(1+\cos\theta_2)^2$	$-\sqrt{2}\sin\theta_1(1+\cos\theta_2)\sin\theta_2$	$\frac{1}{\sqrt{2}}(1-\cos\theta_1)\sin^2\theta_2$
$\|1,-1\rangle \leftrightarrow \|2,-1\rangle$	$\frac{1}{\sqrt{2}}(1+\cos\theta_1)(1+\cos\theta_2)\sin\theta_2$	$-\sqrt{2}\sin\theta_1\left(1-\cos\theta_2-2\cos^2\theta_2\right)$	$-\frac{1}{\sqrt{2}}(1-\cos\theta_1)\sin(2\theta_2)$
$\|1,-1\rangle \leftrightarrow \|2,0\rangle$	$\sqrt{3}(1+\cos\theta_1)\sin^2\theta_2$	$\sqrt{3}\sin\theta_1\sin(2\theta_2)$	$-\frac{1}{\sqrt{3}}(1-\cos\theta_1)\left(1-3\cos^2\theta_2\right)$
$\|1,-1\rangle \leftrightarrow \|2,1\rangle$	$\sqrt{2}(1+\cos\theta_1)(1-\cos\theta_2)\sin\theta_2$	$\sqrt{2}\sin\theta_1\left(1+\cos\theta_2-2\cos^2\theta_2\right)$	$\frac{1}{\sqrt{2}}(1-\cos\theta_1)\sin(2\theta_2)$
$\|1,-1\rangle \leftrightarrow \|2,2\rangle$	$\frac{1}{\sqrt{2}}(1+\cos\theta_1)(1-\cos\theta_2)^2$	$\sqrt{2}\sin\theta_1(1-\cos\theta_2)\sin\theta_2$	$\frac{1}{\sqrt{2}}(1-\cos\theta_1)\sin^2\theta_2$
$\|1,0\rangle \leftrightarrow \|2,-2\rangle$	$-\sin\theta_1(1+\cos\theta_2)^2$	$-2\cos\theta_1(1+\cos\theta_2)\sin\theta_2$	$\sin\theta_1\sin^2\theta_2$
$\|1,0\rangle \leftrightarrow \|2,-1\rangle$	$-2\sin\theta_1(1+\cos\theta_2)\sin\theta_2$	$-2\cos\theta_1\left(1-\cos\theta_2-2\cos^2\theta_2\right)$	$-\sin\theta_1\sin(2\theta_2)$
$\|1,0\rangle \leftrightarrow \|2,0\rangle$	$-\sqrt{6}\sin\theta_1\sin^2\theta_2$	$\sqrt{6}\cos\theta_1\sin 2\theta_2$	$-\sqrt{\frac{2}{3}}\sin\theta_1\left(1-3\cos^2\theta_2\right)$
$\|1,0\rangle \leftrightarrow \|2,1\rangle$	$-2\sin\theta_1(1-\cos\theta_2)\sin\theta_2$	$2\cos\theta_1\left(1+\cos\theta_2-2\cos^2\theta_2\right)$	$\sin\theta_1\sin(2\theta_2)$
$\|1,0\rangle \leftrightarrow \|2,2\rangle$	$-\sin\theta_1(1-\cos\theta_2)^2$	$2\cos\theta_1(1-\cos\theta_2)\sin\theta_2$	$\sin\theta_1\sin^2\theta_2$
$\|1,1\rangle \leftrightarrow \|2,-2\rangle$	$\frac{1}{\sqrt{2}}(1-\cos\theta_1)(1+\cos\theta_2)^2$	$\sqrt{2}\sin\theta_1(1+\cos\theta_2)\sin\theta_2$	$\frac{1}{\sqrt{2}}(1+\cos\theta_1)\sin^2\theta_2$
$\|1,1\rangle \leftrightarrow \|2,-1\rangle$	$\sqrt{2}(1-\cos\theta_1)(1+\cos\theta_2)\sin\theta_2$	$\sqrt{2}\sin\theta_1\left(1-\cos\theta_2-2\cos^2\theta_2\right)$	$-\frac{1}{\sqrt{2}}(1+\cos\theta_1)\sin(2\theta_2)$
$\|1,1\rangle \leftrightarrow \|2,0\rangle$	$\sqrt{3}(1-\cos\theta_1)\sin^2\theta_2$	$-\sqrt{3}\sin\theta_1\sin(2\theta_2)$	$-\frac{1}{\sqrt{3}}(1+\cos\theta_1)\left(1-3\cos^2\theta_2\right)$
$\|1,1\rangle \leftrightarrow \|2,1\rangle$	$\sqrt{2}(1-\cos\theta_1)(1-\cos\theta_2)\sin\theta_2$	$-\sqrt{2}\sin\theta_1\left(1+\cos\theta_2-2\cos^2\theta_2\right)$	$\frac{1}{\sqrt{2}}(1+\cos\theta_1)\sin(2\theta_2)$
$\|1,1\rangle \leftrightarrow \|2,2\rangle$	$\frac{1}{\sqrt{2}}(1-\cos\theta_1)(1-\cos\theta_2)^2$	$-\sqrt{2}\sin\theta_1(1-\cos\theta_2)\sin\theta_2$	$\frac{1}{\sqrt{2}}(1+\cos\theta_1)\sin^2\theta_2$

Table 5.1: Normalised coupling coefficients for all possible transitions with σ^- polarised field present. Values were taken from B. Foxon's thesis [1].

field, we can observe the potential landscape of a particular state shift and tilt seen in figure 5.1 to better align with the curvature of the other potential. To achieve this, the δE contribution to the total Hamiltonian must have the opposite curvature compared to what is shown in Figure 4.25. A $|F=1, m_F=-1\rangle \leftrightarrow |F=2, m_F=-2\rangle$ transition is a suitable choice due to its curvature when coupled with σ^- polarisation; however, the MW frequency and amplitude must be carefully chosen for the best results.

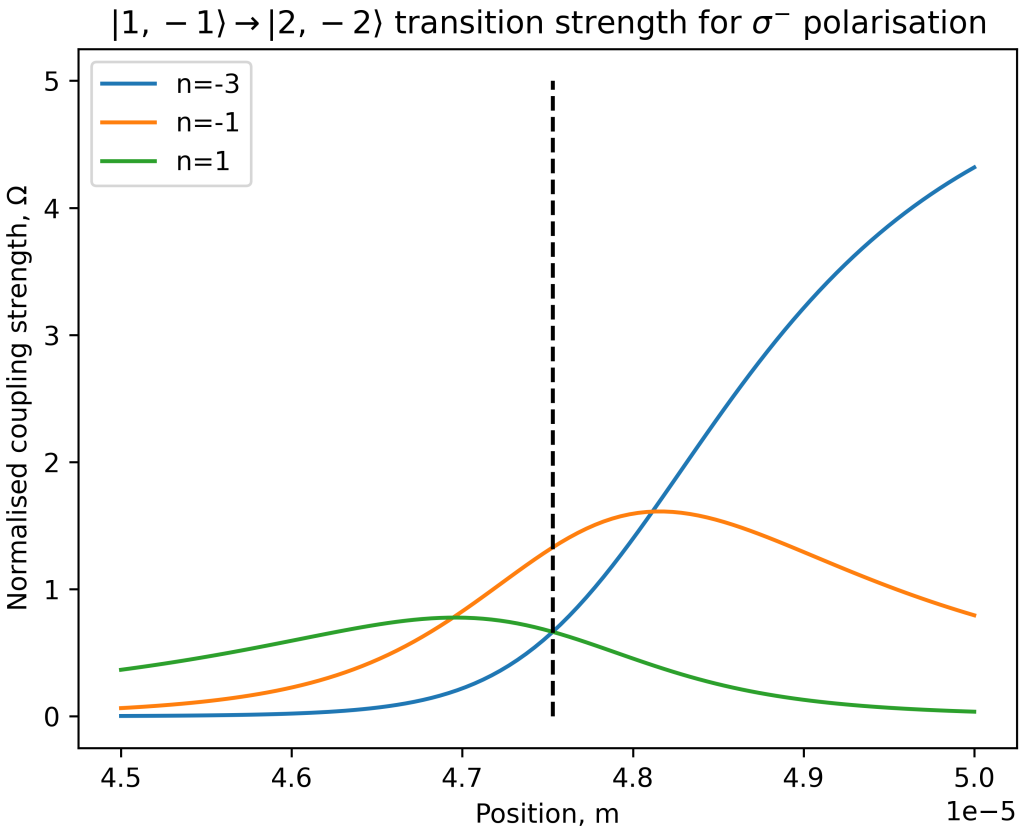

Figure 5.1: Coupling strength Ω vs. position for atoms dressed with 1 MHz dressing field and $\frac{\partial B}{\partial x}$ = 300G/cm matching parameters from figure 4.25. Groups -3, -1, and 1 have non-vanishing coupling coefficients for σ^- polarisation. A 35µG MW field amplitude is assumed and the dashed vertical line provides a visual reference for the resonant field taken as the average between values for F=1 and F=2 manifolds.

First signs of successful MW dressing have been observed by looking at the atoms in an RF-dressed IP trap. We have used the monopole MW antenna inside the vacuum chamber to dress and probe the atoms. The dressing frequency was set to be 3.085MHz above the hyperfine splitting frequency and $\Omega_{RF,Rabi} \approx$ 200kHz, which corresponds to a blue-detuned MW dressing from the transition $|F=1, m_F=-1\rangle \leftrightarrow |F=2, m_F=-1\rangle$ in group $n=3$. We observe a small shift in the transition frequency as well as improvement in linewidth. More power and multiple dressing frequencies must be introduced to achieve a desired linewidth of several Hz.

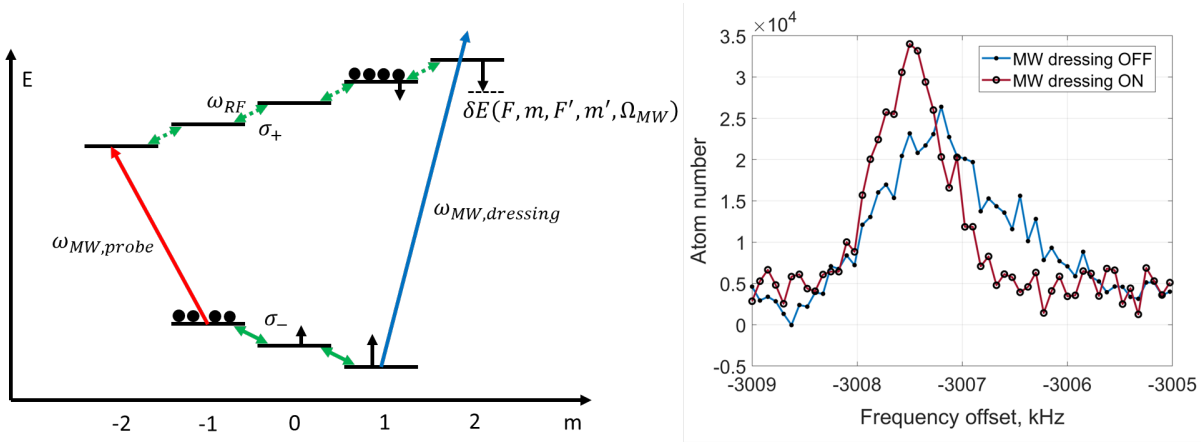

Figure 5.2: MW transition linewidth improves with MW dressing enabled.

5.2 Operation Under Tilt

The state-dependent RF-dressed adiabatic potential implementation can be expanded to have higher order multipole traps providing tighter confinement of atoms in the radial direction. Currently, the modulation of effective Rabi frequency by ±25MHz only allows setup operation under a small tilt. The largest potential gradient in the longitudinal direction of the trap is given by

$$\frac{\partial E_{RFtrap}}{\partial \theta} = 2\pi \times 25kHz \frac{\partial \sin\theta}{\partial \theta}\hbar. \tag{5.3}$$

The maximum gravitational potential gradient around the ring tilted at an angle α_{tilt} is given as

$$\frac{\partial E_{grav}}{\partial \theta} = mgr \sin\alpha_{tilt}. \tag{5.4}$$

Combining equations 5.3 and 5.4 provides a way to calculate the maximum possible tilt without losing the atoms due to gravity forces.

$$\sin\alpha_{tilt} = \frac{2\pi\hbar \times 25kHz\hbar}{mgr} \tag{5.5}$$

The theoretical maximum tilt achievable currently is only 0.67° and the minimum required Rabi frequency modulation frequency needed to tilt the setup by 90 degrees is on the order of 2.1MHz. Having more lattice sites will ensure tighter confinement along the track which will also help to overlap the two thermal clouds at the end of the interferometer sequence with higher precision. The result above puts a lower bound on ω_{RF}, since it is required that $\Omega_{RF,Rabi} < \omega_{RF}$ to remain in the adiabatic regime.

5.3 Setup Redesign

Considering arguments laid out in section 5.2, it has been found that an Ioffe-Pritchard type trap can address a lot of issues and requirements presented by the experiment. A lifted trap bottom enables adiabatic transfer into RF-dressed potentials while avoiding interaction with higher RF harmonics and prevents Majorana losses during the cooling stages. The changes in setup geometry are reflected in the designs of the vacuum compatible PCB as well as the RF and the EM chips. Additional changes are also covered in the following sections. Unfortunately, due to delays in supply chain and experimental setbacks, we were unable to test this new setup and quantify the impact of the improvements.

5.3.1 The PCB

The PCB has been redesigned to include straight wire segments forming a H-trap as. The PCB shown in figure 5.3 will be able to form IP type traps with an applied external magnetic field. The lifted trap bottom and a larger trap volume will prevent Majorana losses during the early evaporative cooling stages, removing the need for optically plugged quadrupole trap setup. It will also facilitate easier transfer of atoms into RF-dressed ring quadrupole trap which will improve the signal to noise ration of our measurements. The new design, shown in the figure below, features 14 conductive layers, with the PCB coils containing up to 10 turns and the straight wires placed in the two layers just under the surface of the PCB. The board still has the same number of concentric wire windings (C1-C7), however, the coils are now rectangular. The shape of the PCB coils was changed to work better with the bar wires forming the H-trap.

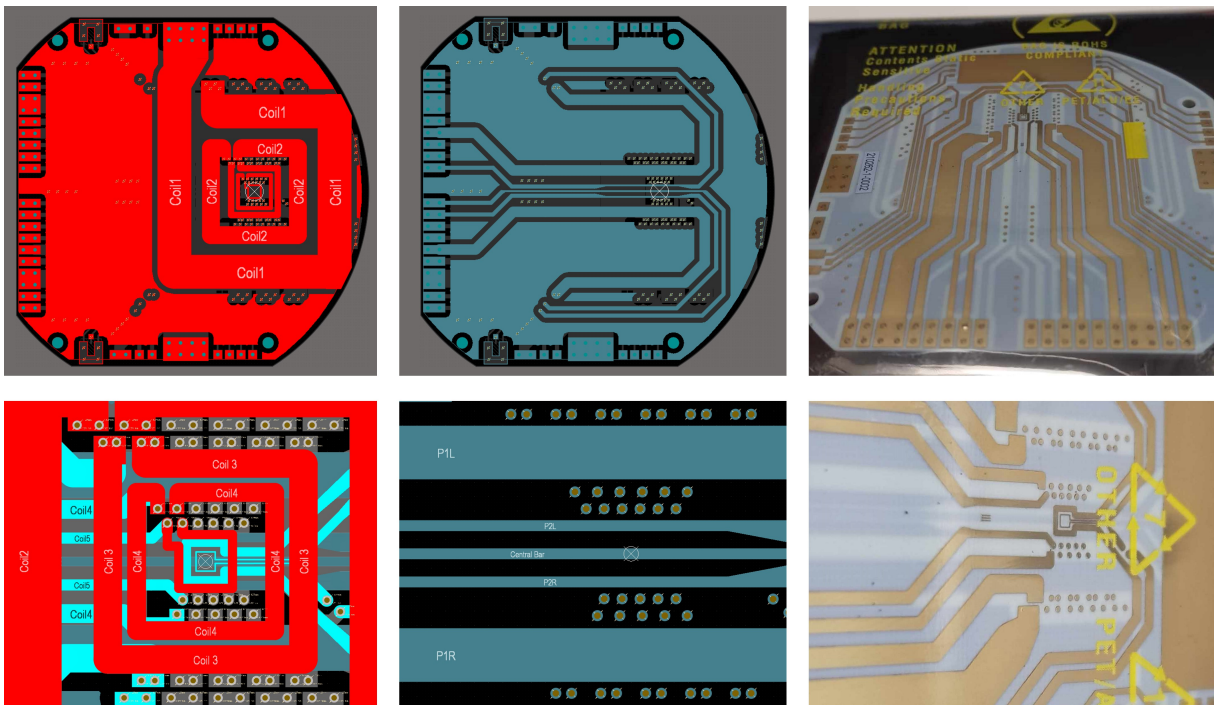

Figure 5.3: The redesigned PCB.

The simulation of the transport stage in figure 5.4 shows an IP trap forming above the PCB surface with the bias fields applied. The isosurfaces indicate where the total magnetic field magnitude remains the same and show that the trap bottom is lifted above zero by at least 0.3 G at all times.

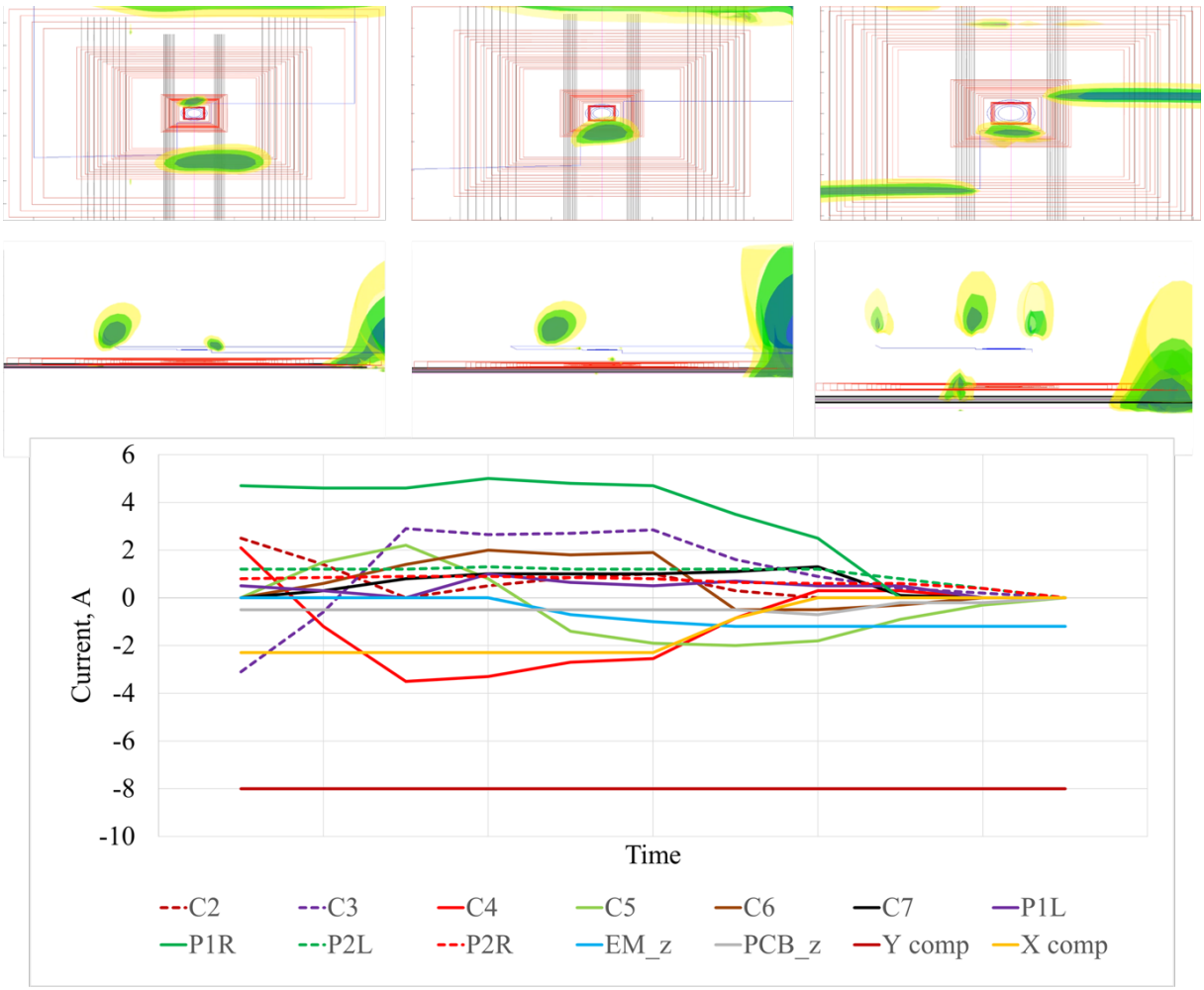

Figure 5.4: PCB transport sequence. The top row of images show the isopotential surfaces of the trap traversing the extent of the PCB. The bottom graph shows the currents required to complete the transport sequence. Here, C1-C7 are concentric square coils that follow the same convention as the current PCB, P1L & P1R are the large parallel bars, P2L & P2R are smaller parallel bars, PCB_z is the central wire, EM_z is the EM chip z-wire, and X comp/Y comp are the external bias coils.

5.3.2 The RF Chip

The RF chip currently produces a radially symmetric field that is tilted from the vertical axis by only $\approx 17°$ at the location of the atom trap, meaning that a large fraction of the RF power is being wasted. The design of the RF chip can be improved by reducing the inner radius of the spiral. DC field simulations of the setup presented in figure 5.5 have shown that at the location of the ring quadrupole trap the RF field is pointing at 17.96° which agrees with the Rabi frequency measurements described in section 4.10. The new design should have have a smaller spiral which produces a field rotated by 40.29° from the vertical axis. While the smaller loop creates a smaller overall field, the radial component increases in magnitude and the unwanted vertical field component becomes smaller.

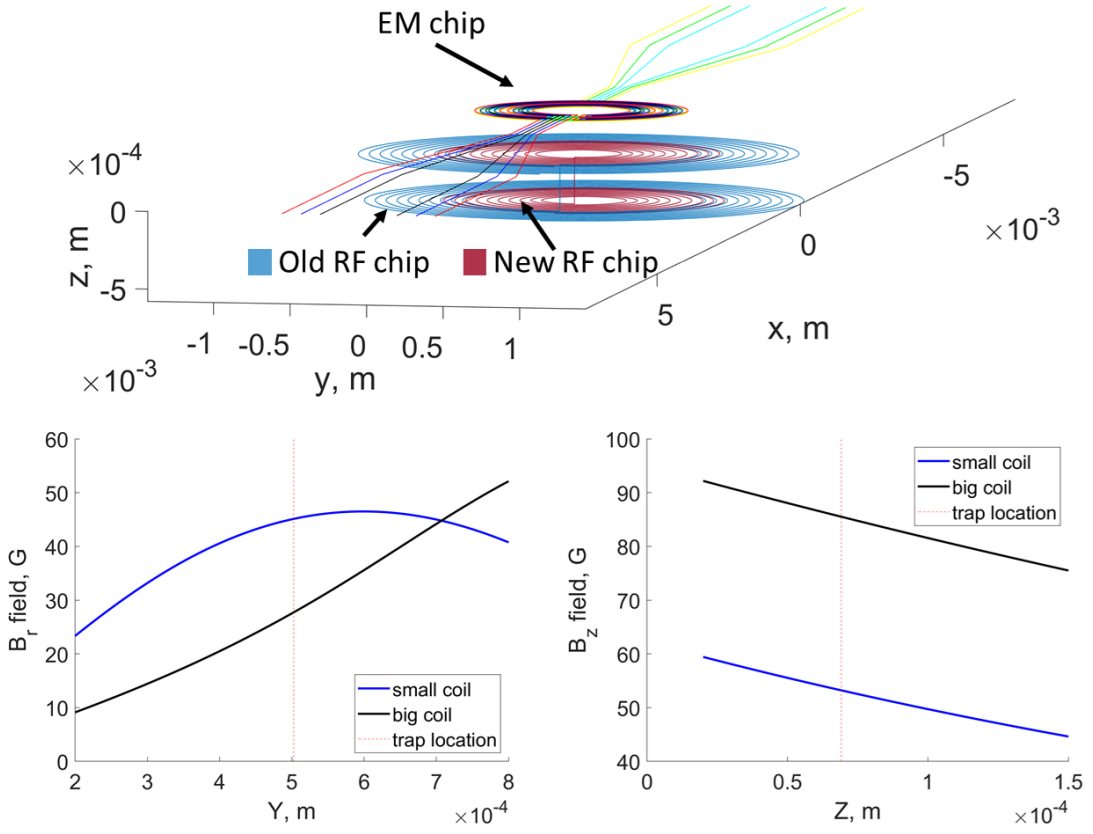

Figure 5.5: Numerical simulation of field produced by the RF chip.

In addition to the adjusted spiral geometry a z-trap structure can be added by taking advantage of previously unused gold pads. The z-wire near the atom chip might prove to be useful when trying to compress the atoms during the evaporative cooling ramp. Currently, however, a possibility to evaporate a z-wire structure onto one of previously

unused RF chips is being explored. Figure 5.6 shows a 1 mm wide gold conductor with 2μm thickness that has been deposited to reduce the manufacturing time and costs. The rectangular gold patches have also been included to serve as levelling spacers that will keep the EM chip from tilting during the bonding process.

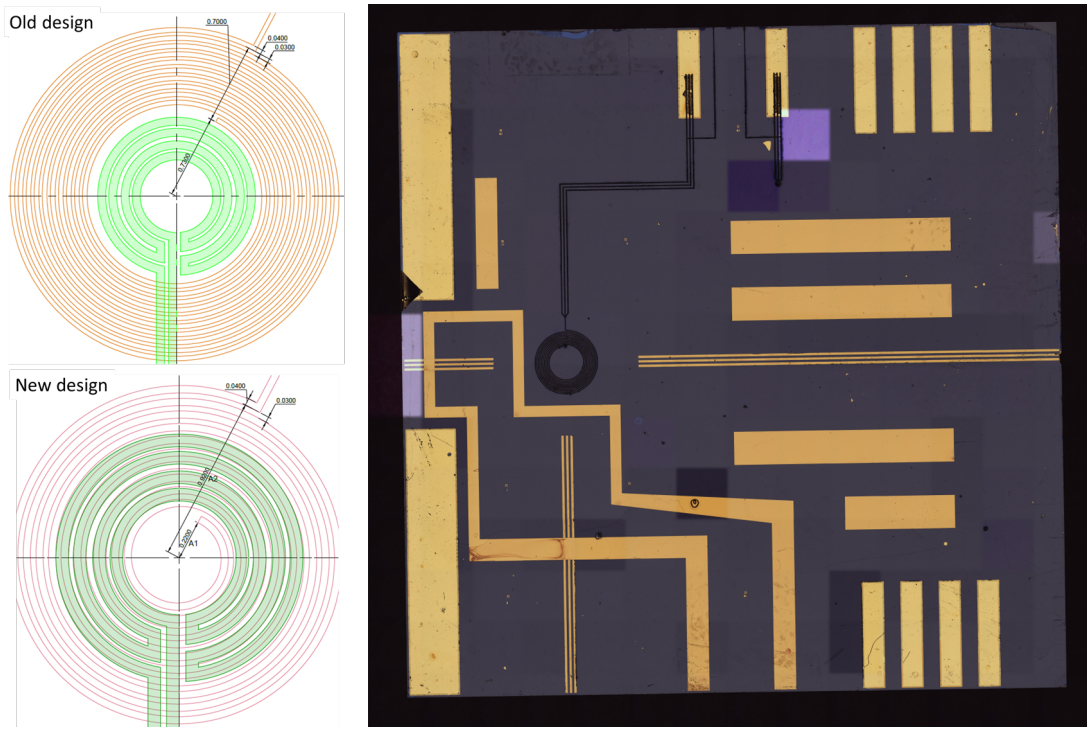

Figure 5.6: The redesigned RF chip.

5.3.3 The EM chip

The EM chip remains largely unchanged, however, the substrate thickness can be reduced from 280μm to 200μm, getting the atoms even closer to the PCB coils. Just like the case of the RF chip, a z-wire structure seen in figure 5.7 has been added to the lower conductor layer to allow the formation of tightly confined IP traps.

The main setback is a small mistake made during the bonding process which misaligned the EM chip with respect to the RF chip. The alignment marks are 100μm wide and separated by 100μm gaps. Skipping one of these alignment marks resulted in chip misalignment of $\approx$ 200μm which, unfortunately, made the PCB-chip stack unusable.

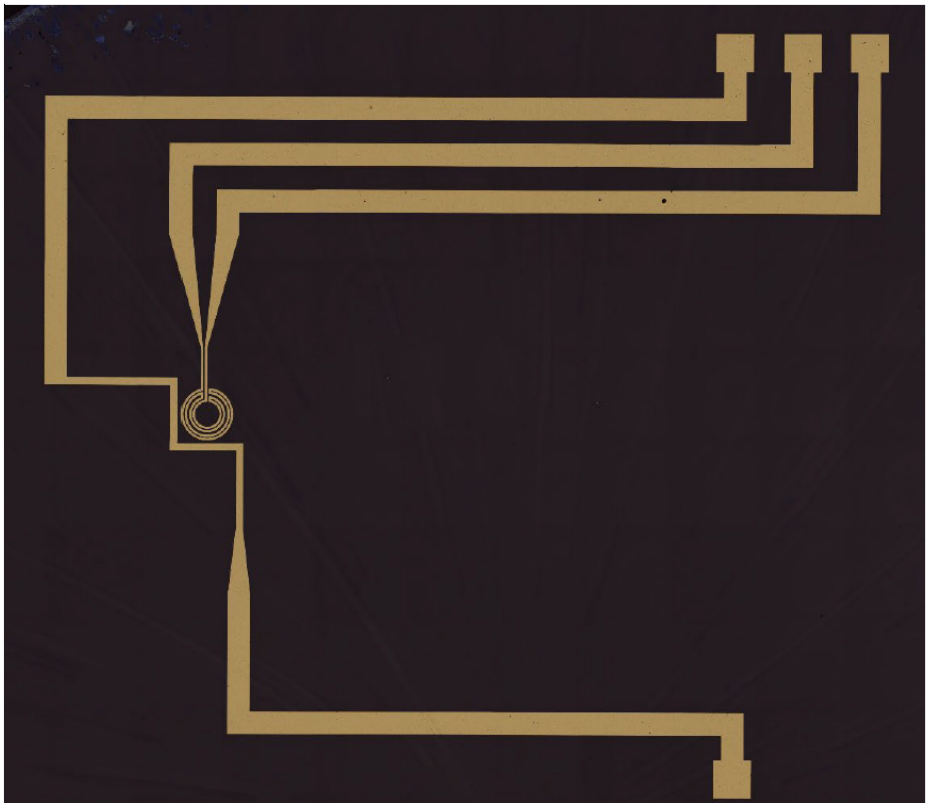

Figure 5.7: The redesigned atom chip bottom layer.

5.4 Time-Averaged Adiabatic Potentials

One of the remaining challenges preventing us from completing an interferometric measurement is the spatial mismatch between positions of atoms in the $F = 1$ and $F = 2$ ground states. The trapping potentials defined by the σ_+-polarised field will have their principal axes tilted with respect to traps defined by the σ_--polarised field. Figure 5.8 shows a simulation where a multipole trap of 2nd order is used as an example. This tilt between the trapping potentials will cause the loss of contrast when the atoms interact with the MW field during the read-out stage of the experiment. Performance of the interferometer can be affected by increased temperature of the atom cloud or larger RF field produced by the RFx coil. The spatial overlap becomes even worse under tilt due to the gravity pulling the atoms towards the edges of the elliptical traps. Reducing the temperature means that less atoms remain in the trap, and the reduced RFx field lowers the trap depth. Both of these outcomes are undesirable and, thus, Time-averaged adiabatic potentials (TAAPs) have to be employed [83, 84, 85].

The time-averaged potentials, as outlined in J. Johnson's thesis [18], require modulation the z-component of the RF dressing field at the right frequency, leading to time-averaged potentials defined as

$$V_{average} = \frac{1}{T}\int_0^T V(t)dt. \tag{5.6}$$

The frequency at which the RF field magnitude needs to be modulated needs to be higher than the mechanical motion frequency of the atom within the trap but below the dressing frequency ω_{RF}. If the modulation frequency is too low, the atoms will always follow the moving potential minimum and not experience any averaging effects. If the field is modulated too fast, the modulation frequency becomes comparable to ω_{RF}, so the condition for allowed RF field modulation frequency ω_m is given by $\omega_{trap} << \omega_m << \omega_{RF}$. The RF field magnitude in the z-direction can be represented by Equation 5.7;

$$B_{RF,z}(t) = B_{RF,z}\sin\omega_m t. \tag{5.7}$$

Experimentally, this would require an RF source with a facility for I/Q modulation. By modulating the RF field magnitude at angular frequency $\omega_m \approx 2\pi \times 10\text{kHz}$ we can obtain the average potential for both atomic states. We can see in figure 5.8 that the traps in this case overlap completely, however, the trap depth is reduced.

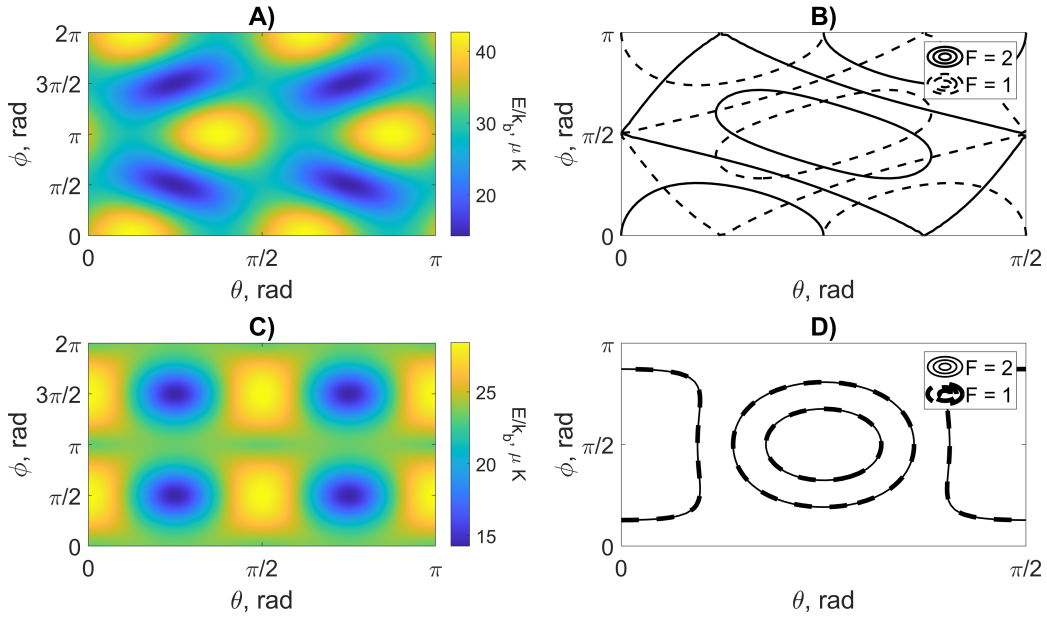

Figure 5.8: TAAP influence on the trapping potential shape. Figures A) and B) show traps with no time-averaging, C) and D) display the trap potentials overlap when the DC magnetic field is modulated. Figures A) and B) show potentials for $|F = 2, \bar{m}_F = 1\rangle$ state with RF field strengths of 1.5 G in the z-direction, 0.9 G in the radial direction, and 0.3 G in the x-direction. The isopotential contour plots on the right indicate the tilt of the traps keeping atoms in the states $F = 1$ (dashed lines) and $F = 2$ (solid lines).

5.5 Conclusion

The scheme presented in this thesis has many potential advantages in sensing applications and the experimental observations described here have increased the confidence in feasibility of this scheme. The completed work also sets a solid foundation for making a new generation of atom chips for Sagnac interferometry. While the measurement is possible and the path to proceed is clear, this endeavour remains extremely difficult. The experiment can be improved by altering the existing designs and implementing additional techniques that will mitigate the main challenges that are preventing us from progressing forward in the short-term. Once the device is operational, there will be a set of new problems to explore, mainly integration of the cold atom setup into a hybrid system that benefits from high measurement bandwidth of traditional rotation sensors and long-term stability of matterwave interferometers.

Bibliography

[1] Bethany Foxon. *Quantum coherence control for radio-frequency dressed cold atom systems*. Phd thesis, University of Nottingham, July 2021.

[2] Daniel A Steck. Rubidium 87 d line data. 2001.

[3] Georges Sagnac. L'éther lumineux démontré par l'effet du vent relatif d'éther dans un interféromètre en rotation uniforme. *CR Acad. Sci.*, 157:708–710, 1913.

[4] Yongxiang Lu, Chuijun Qian, and Hui He. *A history of Chinese science and technology*, volume 1. Springer, 2015.

[5] The Editors of Encyclopaedia. "Foucault pendulum". Encyclopedia Britannica. `https://www.britannica.com/science/Foucault-pendulum`. Accessed 15 June 2023.

[6] Guo Zhanshe, Cheng Fucheng, Li Boyu, Cao Le, Lu Chao, and Song Ke. Research development of silicon mems gyroscopes: A review. *Microsystem Technologies*, 21:2053–2066, 2015.

[7] Sten F. Odenwald and Cait M. Bailey. Gravimetric detection of earth's rotation using crowdsourced smartphone observations. *IEEE Access*, 7:148131–148141, 2019.

[8] W. M. Macek and Jr. Davis, D. T. M. Rotation rate sensing with travelling-wave ring lasers. *Applied Physics Letters*, 2(3):67–68, 11 2004.

[9] Brynle Barrett, Rémy Geiger, Indranil Dutta, Matthieu Meunier, Benjamin Canuel, Alexandre Gauguet, Philippe Bouyer, and Arnaud Landragin. The sagnac effect:

20 years of development in matter-wave interferometry. *Comptes Rendus Physique*, 15(10):875–883, 2014.

[10] John F. Clauser. Ultra-high sensitivity accelerometers and gyroscopes using neutral atom matter-wave interferometry. *Physica B+C*, 151(1):262–272, 1988.

[11] M. v. Laue. Zum versuch von f. harreß. *Annalen der Physik*, 367(13):448–463, 1920.

[12] Paul Langevin. Sur la théorie de relativité et l'expérience de m. sagnac. *CR Acad. Sci*, 173:831–834, 1921.

[13] Paul Langevin. Sur l'expérience de sagnac. *Compt. Rend*, 205(5):304–306, 1937.

[14] J. C. Hafele and Richard E. Keating. Around-the-world atomic clocks: Observed relativistic time gains. *Science*, 177(4044):168–170, 1972.

[15] T. Fernholz, R. Gerritsma, P. Krüger, and R. J. C. Spreeuw. Dynamically controlled toroidal and ring-shaped magnetic traps. *Phys. Rev. A*, 75:063406, Jun 2007.

[16] Thomas Bishop. *A guided matter-wave Sagnac interferometer*. Phd thesis, University of Nottingham, April 2019.

[17] Fabio Gentile. *Towards an atomic Sagnac interferometer with full dynamical control of atoms in ring waveguides*. Phd thesis, University of Nottingham, December 2019.

[18] Jamie Johnson. *Atom-Chip Designs for a Trapped and Guided Matterwave Sagnac Interferometer*. Phd thesis, University of Nottingham, July 2021.

[19] J. Blake, P. Tantaswadi, and R.T. de Carvalho. In-line sagnac interferometer current sensor. *IEEE Transactions on Power Delivery*, 11(1):116–121, 1996.

[20] A. N. Starodumov, L. A. Zenteno, D. Monzon, and E. De La Rosa. Fiber Sagnac interferometer temperature sensor. *Applied Physics Letters*, 70(1):19–21, 01 1997.

[21] Ke-Xun Sun, M. M. Fejer, Eric Gustafson, and Robert L. Byer. Sagnac interferometer for gravitational-wave detection. *Phys. Rev. Lett.*, 76:3053–3056, Apr 1996.

[22] Tobias Eberle, Sebastian Steinlechner, Jöran Bauchrowitz, Vitus Händchen, Henning Vahlbruch, Moritz Mehmet, Helge Müller-Ebhardt, and Roman Schnabel. Quantum enhancement of the zero-area sagnac interferometer topology for gravitational wave detection. *Phys. Rev. Lett.*, 104:251102, Jun 2010.

[23] E. R. Moan, R. A. Horne, T. Arpornthip, Z. Luo, A. J. Fallon, S. J. Berl, and C. A. Sackett. Quantum rotation sensing with dual sagnac interferometers in an atom-optical waveguide. *Phys. Rev. Lett.*, 124:120403, Mar 2020.

[24] Romain Gautier, Mohamed Guessoum, Leonid A. Sidorenkov, Quentin Bouton, Arnaud Landragin, and Remi Geiger. Accurate measurement of the sagnac effect for matter waves. *Science Advances*, 8(23):eabn8009, 2022.

[25] AD King. Inertial navigation-forty years of evolution. *GEC review*, 13(3):140–149, 1998.

[26] Yu. N. Korkishko, V. A. Fedorov, V. E. Prilutskiy, V. G. Ponomarev, I. V. Fedorov, S. M. Kostritskii, I. V. Morev, D. V. Obuhovich, S. V. Prilutskiy, A. I. Zuev, and V. K. Varnakov. Highest bias stability fiber-optic gyroscope srs-5000. In *2017 DGON Inertial Sensors and Systems (ISS)*, pages 1–23, 2017.

[27] D. Savoie, M. Altorio, B. Fang, L. A. Sidorenkov, R. Geiger, and A. Landragin. Interleaved atom interferometry for high-sensitivity inertial measurements. *Science Advances*, 4(12):eaau7948, 2018.

[28] J. Lautier, L. Volodimer, T. Hardin, S. Merlet, M. Lours, F. Pereira Dos Santos, and A. Landragin. Hybridizing matter-wave and classical accelerometers. *Applied Physics Letters*, 105(14):144102, 10 2014.

[29] F Riehle, T Kisters, A Witte, J Helmcke, and C J Borde. Optical ramsey spectroscopy in a rotating frame: Sagnac effect in a matter-wave interferometer. *Physical Review Letters; (USA)*, 67:2, 7 1991.

[30] Alan Lenef, Troy D. Hammond, Edward T. Smith, Michael S. Chapman, Richard A.

Rubenstein, and David E. Pritchard. Rotation sensing with an atom interferometer. *Phys. Rev. Lett.*, 78:760–763, Feb 1997.

[31] Markus K. Oberthaler, Stefan Bernet, Ernst M. Rasel, Jörg Schmiedmayer, and Anton Zeilinger. Inertial sensing with classical atomic beams. *Phys. Rev. A*, 54:3165–3176, Oct 1996.

[32] Christian Schubert, Sven Abend, Matthias Gersemann, Martina Gebbe, Dennis Schlippert, Peter Berg, and Ernst M. Rasel. Multi-loop atomic sagnac interferometry. *Scientific reports*, 11(1):16121–16121, 2021.

[33] Christian Schubert, Sven Abend, Matthias Gersemann, Martina Gebbe, Dennis Schlippert, Peter Berg, and Ernst M Rasel. Multi-loop atomic sagnac interferometry. *Scientific Reports*, 11(1):1–9, 2021.

[34] Hyosub Kim, Katarzyna Krzyzanowska, KC Henderson, Changhyun Ryu, Eddy Timmermans, and Malcolm Boshier. One second interrogation time in a 200 round-trip waveguide atom interferometer. *arXiv preprint arXiv:2201.11888*, 2022.

[35] Hélène Perrin and Barry M. Garraway. Trapping atoms with radio frequency adiabatic potentials. In *Advances In Atomic, Molecular, and Optical Physics*, pages 181–262. Elsevier, 2017.

[36] Jamie Johnson, Bethany Foxon, Vilius Atkocius, Fabio Gentile, Sindhu Jammi, Konstantinos Poulios, and Thomas Fernholz. Hafele and keating on a chip: Sagnac interferometry with a single clock. In *Optical, Opto-Atomic, and Entanglement-Enhanced Precision Metrology II*, volume 11296, pages 224–237. SPIE, 2020.

[37] L. et. al. Amico. Roadmap on Atomtronics: State of the art and perspective. *AVS Quantum Science*, 3(3), 08 2021. 039201.

[38] Arthur H. Compton. A quantum theory of the scattering of x-rays by light elements. *Phys. Rev.*, 21:483–502, May 1923.

[39] C.J. Foot. *Atomic Physics*. Oxford Master Series in Physics. OUP Oxford, 2004.

[40] N. Bohr Dr. phil. I. on the constitution of atoms and molecules. *The London, Edinburgh, and Dublin Philosophical Magazine and Journal of Science*, 26(151):1–25, 1913.

[41] Bergmann Ludwig, Schaefer Clemens, Raith Wilhelm, and Ludwig Bergmann. *Constituents of matter : atoms, molecules, nuclei and particles*. Walter de Gruyter, Berlin New York, 1997.

[42] A. Corney. *Atomic and Laser Spectroscopy*. Oxford science publications. Clarendon Press, 1977.

[43] S Tolansky. Negative nuclear spins and a proposed negative proton. *Nature*, 134(3375):26–26, 1934.

[44] William H. Wing. On neutral particle trapping in quasistatic electromagnetic fields. *Progress in Quantum Electronics*, 8(3):181–199, 1984.

[45] Norman F. Ramsey. A molecular beam resonance method with separated oscillating fields. *Phys. Rev.*, 78:695–699, Jun 1950.

[46] Ch. J. Bordé, Ch. Salomon, S. Avrillier, A. van Lerberghe, Ch. Bréant, D. Bassi, and G. Scoles. Optical ramsey fringes with traveling waves. *Phys. Rev. A*, 30:1836–1848, Oct 1984.

[47] Albert Messiah. *Quantum mechanics*. Courier Corporation, 2014.

[48] H. F. Baker. On the exponential theorem for a simply transitive continuous group, and the calculation of the finite equations from the constants of structure. *Proceedings of the London Mathematical Society*, s1-34(1):91–129, 1901.

[49] Clarence Zener and Ralph Howard Fowler. Non-adiabatic crossing of energy levels. *Proceedings of the Royal Society of London. Series A, Containing Papers of a Mathematical and Physical Character*, 137(833):696–702, 1932.

[50] L. Landau. Zur theorie der energieubertragung. ii, 1932.

[51] Fabio Gentile, Jamie Johnson, Konstantinos Poulios, and Thomas Fernholz. Ring-shaped atom-trap lattices using multipole dressing fields. *arXiv preprint arXiv:1909.01186*, 2019.

[52] John Miles (KE5FX). Automated phase-noise measurement utility for spectrum analyzers. `http://www.ke5fx.com/gpib/readme.htm`. Accessed June 2023.

[53] Ward Harriman (AE6TY). Open-source electronic component simulation software. `http://www.ae6ty.com/smith_charts.html`. Accessed June 2023.

[54] George G Harman. *Wire bonding in microelectronics / George Harman.* McGraw-Hill, New York, 3rd ed. edition, 2010.

[55] Daryl W Preston. Doppler-free saturated absorption: Laser spectroscopy. *American Journal of Physics*, 64(11):1432–1436, 1996.

[56] Jürgen Appel, Andrew MacRae, and A I Lvovsky. A versatile digital ghz phase lock for external cavity diode lasers. *Measurement Science and Technology*, 20(5):055302, apr 2009.

[57] Gary C Bjorklund, MD Levenson, W Lenth, and C Ortiz. Frequency modulation (fm) spectroscopy: theory of lineshapes and signal-to-noise analysis. *Applied Physics B*, 32:145–152, 1983.

[58] G. Reinaudi, T. Lahaye, Z. Wang, and D. Guéry-Odelin. Strong saturation absorption imaging of dense clouds of ultracold atoms. *Opt. Lett.*, 32(21):3143–3145, Nov 2007.

[59] E. L. Raab, M. Prentiss, Alex Cable, Steven Chu, and D. E. Pritchard. Trapping of neutral sodium atoms with radiation pressure. *Phys. Rev. Lett.*, 59:2631–2634, Dec 1987.

[60] Press release article on the Nobel prize in physics 1997, Oct 1997. `https://www.nobelprize.org/prizes/physics/1997/press-release/`, Accessed July 2023.

[61] Paul D. Lett, Richard N. Watts, Christoph I. Westbrook, William D. Phillips, Phillip L. Gould, and Harold J. Metcalf. Observation of atoms laser cooled below the doppler limit. *Phys. Rev. Lett.*, 61:169–172, Jul 1988.

[62] C. Monroe, W. Swann, H. Robinson, and C. Wieman. Very cold trapped atoms in a vapor cell. *Phys. Rev. Lett.*, 65:1571–1574, Sep 1990.

[63] Magnus Haw, Nathan Evetts, Will Gunton, Janelle Van Dongen, James L. Booth, and Kirk W. Madison. Magneto-optical trap loading rate dependence on trap depth and vapor density. *J. Opt. Soc. Am. B*, 29(3):475–483, Mar 2012.

[64] D. Guéry-Odelin, J. Söding, P. Desbiolles, and J. Dalibard. Strong evaporative cooling of a trapped cesium gas. *Opt. Express*, 2(8):323–329, Apr 1998.

[65] VI Balykin, VS Letokhov, and VI Mishin. Cooling of sodium atoms by resonant laser emission. *Zh. Eksp. Teor. Fiz*, 78:1376–1385, 1980.

[66] J. Dalibard and C. Cohen-Tannoudji. Laser cooling below the doppler limit by polarization gradients: simple theoretical models. *J. Opt. Soc. Am. B*, 6(11):2023–2045, Nov 1989.

[67] T. Fernholz, R. Gerritsma, S. Whitlock, I. Barb, and R. J. C. Spreeuw. Fully permanent magnet atom chip for bose-einstein condensation. *Phys. Rev. A*, 77:033409, Mar 2008.

[68] Willian C. Stwalley and L. H. Nosanow. Possible "new" quantum systems. *Phys. Rev. Lett.*, 36:910–913, Apr 1976.

[69] Pieter Valkering. Optimization of evaporative cooling of rubidium atoms in a magnetic trap. M. Sc. thesis, University of Utrecht, 1999.

[70] C. R. Monroe, E. A. Cornell, C. A. Sackett, C. J. Myatt, and C. E. Wieman. Measurement of cs-cs elastic scattering at t=30 μk. *Phys. Rev. Lett.*, 70:414–417, Jan 1993.

[71] H. M. J. M. Boesten, C. C. Tsai, J. R. Gardner, D. J. Heinzen, and B. J. Verhaar. Observation of a shape resonance in the collision of two cold ^{87}Rb atoms. *Phys. Rev. A*, 55:636–640, Jan 1997.

[72] D. S. Naik and C. Raman. Optically plugged quadrupole trap for bose-einstein condensates. *Phys. Rev. A*, 71:033617, Mar 2005.

[73] K. B. Davis, M. O. Mewes, M. R. Andrews, N. J. van Druten, D. S. Durfee, D. M. Kurn, and W. Ketterle. Bose-einstein condensation in a gas of sodium atoms. *Phys. Rev. Lett.*, 75:3969–3973, Nov 1995.

[74] Dong-Fang Zhang, Tian-You Gao, Ling-Ran Kong, Kai Li, and Kai-Jun Jiang. Production of rubidium bose—einstein condensate in an optically plugged magnetic quadrupole trap. *Chinese Physics Letters*, 33(7):076701, jul 2016.

[75] R. Dubessy, K. Merloti, L. Longchambon, P.-E. Pottie, T. Liennard, A. Perrin, V. Lorent, and H. Perrin. Rubidium-87 bose-einstein condensate in an optically plugged quadrupole trap. *Phys. Rev. A*, 85:013643, Jan 2012.

[76] Rudolf Grimm, Matthias Weidemüller, and Yurii B. Ovchinnikov. Optical dipole traps for neutral atoms. volume 42 of *Advances In Atomic, Molecular, and Optical Physics*, pages 95–170. Academic Press, 2000.

[77] Tobias Schmidutz, Igor Gotlibovych, Stuart Moulder, Robert Campbell, Naaman Tammuz, Richard Fletcher, Alexander Gaunt, Scott Beattie, Robert Smith, and Zoran Hadzibabic. A compact single-chamber apparatus for bose-einstein condensation of 87 rb. In *APS Division of Atomic, Molecular and Optical Physics Meeting Abstracts*, volume 2013, pages Q1–047, 2013.

[78] G. A. Sinuco-Leon, B. M. Garraway, H. Mas, S. Pandey, G. Vasilakis, V. Bolpasi, W. von Klitzing, B. Foxon, S. Jammi, K. Poulios, and T. Fernholz. Microwave spectroscopy of radio-frequency-dressed ^{87}Rb. *Phys. Rev. A*, 100:053416, Nov 2019.

[79] Rogerio de Sousa. *Electron Spin as a Spectrometer of Nuclear-Spin Noise and Other Fluctuations*, pages 183–220. Springer Berlin Heidelberg, Berlin, Heidelberg, 2009.

[80] Hector Mas, Saurabh Pandey, Georgios Vasilakis, and Wolf Von Klitzing. Bichromatic adiabatic shells for atom interferometry. *New Journal of Physics*, 21(12):123039, 2019.

[81] S. Hofferberth, B. Fischer, T. Schumm, J. Schmiedmayer, and I. Lesanovsky. Ultracold atoms in radio-frequency dressed potentials beyond the rotating-wave approximation. *Phys. Rev. A*, 76:013401, Jul 2007.

[82] Yongcheng Ding, Tang-You Huang, Koushik Paul, Minjia Hao, and Xi Chen. Smooth bang-bang shortcuts to adiabaticity for atomic transport in a moving harmonic trap. *Phys. Rev. A*, 101:063410, Jun 2020.

[83] B. E. Sherlock, M. Gildemeister, E. Owen, E. Nugent, and C. J. Foot. Time-averaged adiabatic ring potential for ultracold atoms. *Phys. Rev. A*, 83:043408, Apr 2011.

[84] Sourabh Sarkar, S. P. Ram, V. B. Tiwari, and S. R. Mishra. Different atom trapping geometries with time averaged adiabatic potentials. *The European physical journal. D, Atomic, molecular, and optical physics*, 75(11), 2021.

[85] Hélène Perrin and Barry M. Garraway. Chapter four - trapping atoms with radio frequency adiabatic potentials. volume 66 of *Advances In Atomic, Molecular, and Optical Physics*, pages 181–262. Academic Press, 2017.

[86] Ian T Jolliffe. *Principal component analysis*. Springer, 2002.

[87] C. F. Ockeloen, A. F. Tauschinsky, R. J. C. Spreeuw, and S. Whitlock. Detection of small atom numbers through image processing. *Phys. Rev. A*, 82:061606, Dec 2010.

[88] F. Pedregosa, G. Varoquaux, A. Gramfort, V. Michel, B. Thirion, O. Grisel, M. Blondel, P. Prettenhofer, R. Weiss, V. Dubourg, J. Vanderplas, A. Passos, D. Cournapeau, M. Brucher, M. Perrot, and E. Duchesnay. Scikit-learn: Machine learning in Python. *Journal of Machine Learning Research*, 12:2825–2830, 2011.

[89] Gal Ness, Anastasiya Vainbaum, Constantine Shkedrov, Yanay Florshaim, and Yoav

Sagi. Single-exposure absorption imaging of ultracold atoms using deep learning. *Physical Review Applied*, 14(1), Jul 2020.

[90] Christian Ledig, Lucas Theis, Ferenc Huszár, Jose Caballero, Andrew Cunningham, Alejandro Acosta, Andrew Aitken, Alykhan Tejani, Johannes Totz, Zehan Wang, et al. Photo-realistic single image super-resolution using a generative adversarial network. In *Proceedings of the IEEE conference on computer vision and pattern recognition*, pages 4681–4690, 2017.

[91] Kaiming He, Xiangyu Zhang, Shaoqing Ren, and Jian Sun. Deep residual learning for image recognition. In *Proceedings of the IEEE conference on computer vision and pattern recognition*, pages 770–778, 2016.

Appendix A

Imaging Denoising Techniques

A.0.1 PCA Analysis

Principal component analysis [86] can be used to reduce the noise in the imaging data [87]. It relies on reducing the dimensionality of a complex system by picking out principal axes along which most of the variation within the system happens. We describe a matrix Rij to perform image decomposition using PCA. Here i is the image index and j corresponds to pixels within the image. First, the mean value of each pixel, M_i in the set of N reference images is found.

$$M_i = \frac{1}{N} \sum_{j=1}^{N} R_{ij} \tag{A.1}$$

We can then rewrite samples R as a zero mean value matrix, B. Matrix B only contains information about the individual pixel intensity variation with zero mean value.

$$B = R_{ij} - M_i \tag{A.2}$$

The next step in the process is to calculate a cross-correlation matrix, S, which describes the correlation between any two pixels within the reference images. An image with completely uncorrelated noise in the entire image would only have non-zero terms on the diagonal. On the other hand, correlated pixels, such as in case of interference fringes spanning a wide region of the image, some off-diagonal terms become significant.

$$S = \frac{1}{p-1} BB^T \tag{A.3}$$

The normalised and reshaped eigenvectors of S describe the principal components of all the reference images R, and the corresponding eigenvalues tell us the scaling factor. The eigenvalues are normalised such that the total sum adds to 1. The eigenvectors with the largest eigenvalues tell us along which principal axis the image A is most likely to vary. It is usually sufficient to take only a few largest eigenvectors and disregard the rest. The 'perfect' background image is found by calculating the overlap between image A and each of the most significant principal components. Finally, the eigenvectors, scaled accordingly by taking into account the numerical overlap integral and eigenvalues, are superimposed onto a single picture.

Even with a relatively low resolution image estimating S quickly becomes computationally intensive and demands a lot of memory. For Example, a 640×480 image requires us to define a matrix with over 94×10^9 entries. Thankfully, the deep learning community has developed tools that are specifically meant to deal with this problem. A Python module 'Scikit learn' [88] performs the calculation within minutes without exceeding the memory limit. Some improvement can be seen in the overall background image as well as the regions around the atom chip rings analysed in figure A.1. Processing images only takes a short while, however, this method has its limitations. The random noise withing the atom chip track structure simply cannot be predicted which causes unreliable performance in the vicinity of the atom chip. Indeed, from the figure below we can see that the difference between non-processed and de-noised images contains mostly noise coming from the atom chip tracks.

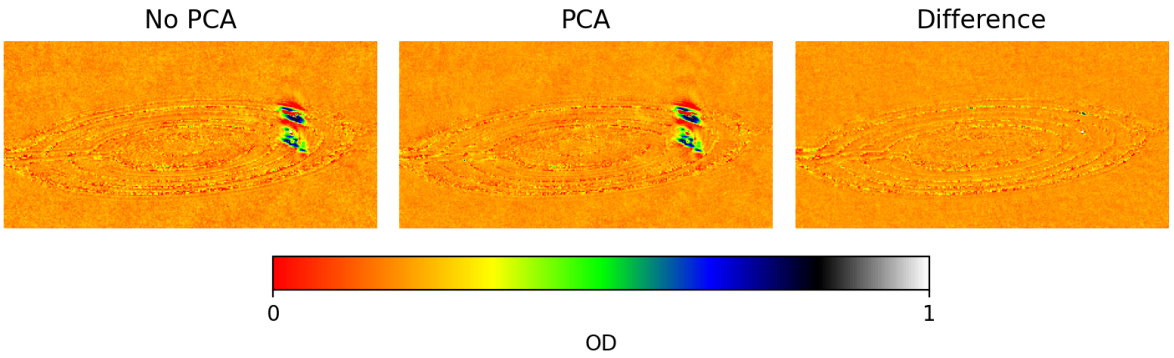

Figure A.1: Optical density image without post-processing vs. PCA de-noising technique. The difference between the two results is shown on the right.

A.0.2 Machine Learning Approach

The fringes and noise in the absorption images comes mostly from the fact that there are multiple pictures taken at different times. Because of that, small displacements of the camera with respect to the setup become apparent. The goal here is to eliminate the need for multiple images entirely as described in [89], by using deep learning techniques.

Although the method itself is complicated, the idea is simple: cut out a 'hole' from the original absorption image with atoms where the cloud is supposed to be, and teach an algorithm to fill in the gaps to produce a background image as shown in figure A.2. The algorithm is learning to fill a hole with reference images which contain no atoms and therefore only produces artificial background light images.

The image generator is written in Python by adapting the code from 'Super resolution generative adversarial network' [90], which has already been successful at recovering small details within complex images. Superres GAN has two main components: a generator and a discriminator. The generator is given poor quality inputs and learns how to produce upscaled images which are then evaluated by the discriminator. The discriminator tries to tell apart the reference images from the ones that were ruined on purpose and then upscaled by the generator. These two networks would usually compete until the quality of the generator and discriminator does not improve anymore. The generator uses a 'Resnet34' [91] network known for working well with image processing applications, and produces some promising results. It manages to fill in the hole with 0.0264% validation

loss. To produce these results, 3300 images have been used, however, these images can be taken a lot faster compared to the experimental sequence. Another advantage would be the computational efficiency. The network only needs to be trained once, the rest of the image processing relies on simple matrix operations which are easily scalable in parallel computing implementations.

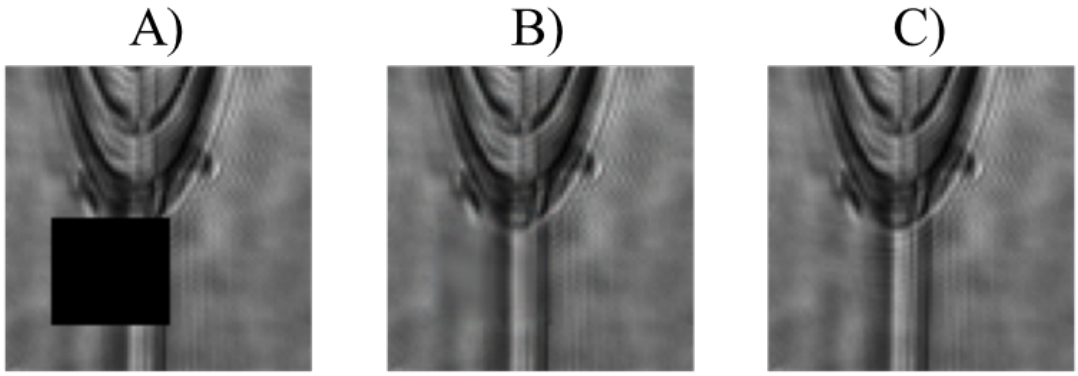

Figure A.2: The generator manages to fill the hole with lots of detail with an input that has some information missing completely. Figure A is the input with region of interest cropped out, B is the reconstructed result, and C is target reference image.

Unfortunately, with the deep learning approach we run into similar issues as with the PCA method. Some of the noise within the images simply cannot be predicted due to its chaotic nature and we end up with unreliable results seen in figure A.3. This method could be revisited in the future, as the discriminator part is still missing in this implementation. It was also pointed out later on that the mean background image was not subtracted from the reference image set before passing the data to train the model. Subtracting the mean image should be the first thing to do in the following iterations of this method.

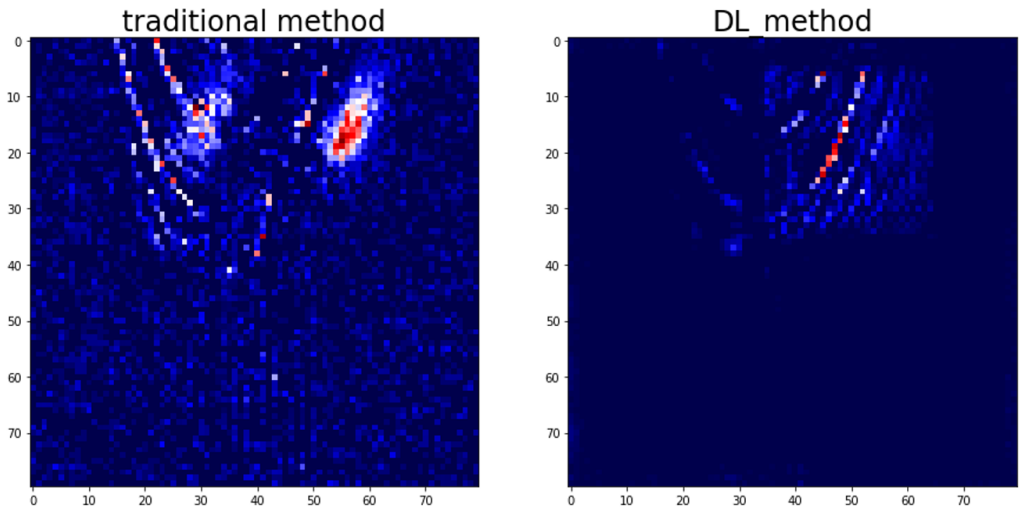

Figure A.3: Image with the 3 image processing and no defringing methods applied (left) vs. deep learning approach (right). Although a lot of background noise is removed with the DL method, the atomic signal also becomes comparable to background noise levels.